Optimal Material Selection for Transducers

by

Gregory Seviora

A thesis
presented to the University of Waterloo
in fulfillment of the
thesis requirement for the degree of
Master of Applied Science
in
Mechanical and Mechatronics Engineering

Waterloo, Ontario, Canada, 2018

Author's Declaration

I hereby declare that I am the sole author of this thesis. This is a true copy of the thesis, including any required final revisions, as accepted by my examiners.

I understand that my thesis may be made electronically available to the public.

Abstract

When selecting an active material for an application, it is tempting to rely upon prior knowledge or commercial products that fit the design criteria. While this method is time effective, it does not provide an optimal selection. The optimal material selection requires an understanding of the limitations of the active material, understanding of the function, constraints and objectives of the device, and rigorous decision making method to ensure rational and clear material selection can be performed.

Therefore, this work looks into the three most researched active materials (piezoelectrics, magnetostrictives and shape memory alloys) and looks at how they work and their difficulties. The field of piezoelectrics is vast and contains ceramics, plastics and cellular structures that couple the mechanical and electrical domain. The difficulty with piezoelectric ceramics is their small strains and the dependence of their coefficients on the ferroelectric domains. Giant magnetostrictives materials couple the mechanical and magnetic domains. They are generally better suited for low-frequency operations since they properties deteriorate rapidly with heat. Shape memory alloys are materials that couple thermal and mechanical domains. They have large strain but are limited in their force output, fatigue life and cycle frequency.

Optimal material selection requires a formalized material selection method. In mechanical material selection, the formal material selection method uses function, constraints and objectives of the designer to limit the parameter space and allow better decisions. Unfortunately, active materials figures of merit are domain dependent and therefore the mechanical material selection method needs to be adapted. A review of device selection of actuators, sensors and energy harvesters indicates a list of functions, constrains and objectives that the designer can use. Through the analysis of these devices figures of merit, it is realized that the issue is that the simplification that the figures of merit perform does not assist in decision making process. It is better to use decision making methods that have been developed in the field of operational research which assists complex comparative decision making.

Finally, the decision making methods are applied to two applications: a resonant cantilever energy harvester and an ultrasound transducer. In both these cases, a review of selection methods of other designers provides guidance of important figures of merit. With these selection methods in consideration, figures of merit are selected and used to find the optimal material based upon the designer preference.

Acknowledgements

I would like to thank all those people that helped me through my work.

Most notably Prof. Mustafa Yavuz and Prof. Eihab Abdel-Rahman for guiding me and giving me the freedom to grow. Others have also helped develop the academic that I am now, such as Sutang Park, Boyd Panton, Andrew Micheal, and so forth. Each of these people that have helped me were formative in my development of how I researched and each one has left a notable trace upon how I looked at this problem.

Table of Contents

List of Tables ix

List of Figures xi

1 Introduction 1

1.1 Motivation . . . 1
1.2 Aim and Objectives . . . 2
1.3 Smart Material Overview . . . 2
1.4 Thesis Organization . . . 5

2 Piezoelectrics 6

2.1 Piezo-, Pyro- and Ferro-electricity . . . 7
2.2 Physical Properties of Piezoelectric Materials . . . 8
2.2.1 Barium Titanate-Type Ferroelectrics . . . 8
2.2.2 Direct and Converse Piezoelectric Effect . . . 10
2.2.3 Ferroelectric and Ferroelastic Switching . . . 11
2.2.4 PZT-type Ferroelectrics and the MPB Concept . . . 11
2.2.4.1 Soft and Hard PZT . . . 12
2.2.5 Poled Polycrystalline Materials . . . 15
2.2.6 Hysteresis and Constitutive Nonlinearities . . . 15
2.2.7 Relaxor Ferroelectrics . . . 17
2.2.8 Piezoelectric Polymers . . . 21
2.2.8.1 Bulk Piezopolymers . . . 22
2.2.8.2 Piezoelectric Polymer Composites . . . 25
2.2.8.3 Piezo-, Pyro- and Ferro-electrets . . . 27
2.3 Application Considerations . . . 28

2.3.1 Stacking . . . 29
2.3.2 Preload . . . 29
2.3.3 Creep and Aging . . . 30
2.3.4 Dielectric Loss Coefficient and Mechanical Quality Factor . . . 32
2.3.5 Small- and Large-Signal Piezoelectric Coupling Coefficient . . . 32
2.3.6 Temperature-Dependent Behavior . . . 33
2.4 Summary and Comments . . . 34

3 Giant Magnetostrictive Materials 36
3.1 Physical Properties of Magnetostrictive Materials . . . 37
3.1.1 Magnetic Dipole Moment Orientation . . . 37
3.1.2 Ferromagnetic Domains . . . 38
3.1.3 Initial Magnetization Processes and Hysteresis . . . 40
3.1.4 Anhysteretic Magnetization and the Magnetomechanical Effect . . . 41
3.1.4.1 Tendency towards anhysteretic magnetization . . . 42
3.1.4.2 Stress dependence of anhysteretic magnetization . . . 42
3.1.5 Other Magnetostrictive Effects . . . 44
3.1.6 Magnetic Material Coefficients . . . 44
3.2 Application Considerations . . . 44
3.2.1 Material Selection . . . 45
3.2.2 Magnetomechanical properties . . . 46
3.2.2.1 Young's Modulus . . . 46
3.2.2.2 Magnetostrictive Coupling and Magnetostrictive Coefficients 47
3.2.2.3 Quality Factor . . . 48
3.2.2.4 Permeability . . . 48
3.2.3 Actuation Optimizations . . . 49
3.2.3.1 Mechanical Prestress . . . 49
3.2.3.2 Magnetic Biasing . . . 50
3.2.4 Temperature-Dependent Behavior . . . 50
3.2.5 Eddy Current Effects . . . 53
3.3 Summary and Comments . . . 53

4 Shape Memory Alloys **54**

4.1 Physical Properties of Shape Memory Alloys . . . 55

4.1.1 Phase Transformation Phenomena . . . 55

4.1.2 Shape Memory Effect . . . 58

4.1.3 Transformation Temperatures . . . 60

4.1.4 Cyclic Behavior . . . 61

4.1.5 R-Phase Transformation . . . 62

4.2 Application Considerations . . . 63

4.2.1 Material Selection . . . 63

4.2.2 Actuator Configuration . . . 65

4.2.2.1 Single-Direction Actuators . . . 65

4.2.2.2 Bias-Force and Antagonistic Actuators . . . 65

4.2.3 Energy Efficiency . . . 66

4.2.4 SMA Position Control . . . 68

4.2.5 Power Output Limitations . . . 69

4.2.5.1 Parallel Designs . . . 70

4.2.5.2 Cooling Time Reduction . . . 70

4.2.6 Factors affecting Fatigue Life . . . 71

4.2.6.1 Alloy Composition . . . 71

4.2.6.2 Stress-Strain-Temperature Regime . . . 72

4.3 Summary and Comments . . . 73

5 Selection Methods and Performance Criteria **75**

5.1 Selection of Materials . . . 76

5.1.1 Active Material Performance Criteria . . . 77

5.2 Selection of Devices . . . 79

5.2.1 Actuators . . . 80

5.2.1.1 Figures of Merit . . . 81

5.2.2 Sensors . . . 86

5.2.2.1 Figures of Merit . . . 87

5.2.3 Energy Harvesters . . . 88

5.2.3.1 Figures of Merit . . . 88

5.3 Alternative Selection Methods . . . 90

5.3.1 Analytic Hierarchy Process . . . 91
5.3.2 Order Preference By Similarity to Ideal Solution . . . 91
5.3.3 Multi-criteria Optimization and Compromise Solution . . . 93
5.3.3.1 AHP+MCDM Method . . . 95
5.4 Summary and Comments . . . 95

6 Implementation of Selection Method 96
6.1 Mechanical Energy Harvesters . . . 97
6.1.1 Resonant Energy Harvester Figures of Merit . . . 98
6.1.1.1 Energy Output . . . 98
6.1.1.2 Design Complexity . . . 99
6.1.2 Generation of Weights . . . 100
6.1.3 MCDM Material Selection for Energy Harvesters . . . 102
6.2 Ultrasound Imaging Transducers . . . 104
6.2.1 Basic Piezoelectric Transducer Design . . . 105
6.2.2 Review of Piezoelectric Ultrasound Figures of Merit . . . 108
6.2.2.1 Transmission Performance . . . 109
6.2.2.2 Receiver Performance . . . 110
6.2.2.3 Design Complexity . . . 111
6.2.3 AHP+MCDM Piezoelectric Ultrasound Material Selection . . . 111
6.2.3.1 Generation of Weights . . . 111
6.2.3.2 TOPSIS and VIKOR Ranking . . . 111
6.3 Selection Criteria Issues . . . 115
6.4 Summary and Comments . . . 116

7 Conclusions and Future Work 117

References 119

APPENDICES 139

A Piezoelectric Derivations 140

B Material Properties 143
B.1 Magnetostrictives . . . 145

List of Tables

1.1 Total number of publications and patents of active materials* 4

2.1 Brief overview of conventional piezoelectrics and piezoelectric ceramics properties 14
2.2 Properties of various generations of relaxor-PT single crystals [22]. 21
2.3 Material property overview of PVDF and PVDF copolymers 25
2.4 An overview of piezo- and ferro-electret films 28

3.1 Summary of magnetostrictive effects [104]. 44
3.2 Magnetostrictive materials properties at room temperature except where indicated [18]. 45
3.3 Comparison of Terfenol and Galfenol Properties [104]. 45

4.1 Major SMAs systems and their advantages [151]. 64
4.2 Thermal and Mechanical Properties for NiTi 65
4.3 Comparison of Loading Configuration of SMA Actuators [160]. 67
4.4 Relative Effects of SMA Cooling Methods [132]. 71

5.1 Functions, Objectives and Constraints [179]. 76
5.2 Overview of Actuator Function, Constraints and Objectives 81
5.3 Illustration of the loss of information from using power density (inspiration from [191] and data from [185]). 84
5.4 Overview of Sensor Function, Constraints and Objectives 87
5.5 Sensor Characteristics [196]. 87
5.6 Overview of Energy Harvester Function, Constraints and Objectives 89
5.7 The fundamental scale of absolute numbers [202]. 91

6.1 Physical Characteristics of power conversion devices and calculated efficiency [223]. 99

6.2 Difference between k^2Q_m and η . . . 100
6.3 Pairwise comparison matrix of energy harvester criteria . . . 101
6.4 Eigenvector weights generated from the pairwise comparison matrix of criteria 102
6.5 Pairwise comparison matrix of energy output sub-criteria . . . 102
6.6 Pairwise comparison matrix of design complexity sub-criteria . . . 102
6.7 Eigenvector weights from the pairwise comparison of sub criteria . . . 103
6.8 Weights for selection criteria . . . 103
6.9 Criteria Values for different alternatives. **Bold = estimated through piezoelectric equations**. . . . 103
6.10 Energy Harvester MCDM ranking results for TOPSIS and VIKOR(v=0.5). **Bold = ranking partially based upon estimated values**. . . . 104
6.11 Pairwise comparison matrices of ultrasound criteria and sub-criteria. . . . 112
6.12 AHP generated weights for ultrasound material selection . . . 113
6.13 Alternative material values and criteria. **Bold = estimated through piezoelectric equations**. . . . 114
6.14 Ultrasound MCDM ranking results for TOPSIS and VIKOR(v=0.5). **Bold = ranking partially based upon estimated values**. . . . 115

B.1 Piezoelectric Properties . . . 143
B.2 Piezoelectric Properties References . . . 144
B.3 Commercial Magnetostrictive Properties . . . 145
B.4 Material-Based Figures of Merit . . . 146
B.5 References for Material-Based Figures of Merit . . . 147

List of Figures

1.1 Number of publications by smart material subject 4

2.1 Classes of functional dielectrics [11]. 7

2.2 $BaTiO_3$ perovskite structure (a) above and (b) below curie temperature T_c. Internal energy as a function of Ti position along the x_3 axis in the (c) paraelectric $T > T_c$ and (d) ferroelectric $T < T_c$ phases [18]. 9

2.3 (a) Surface charge due to a spontaneous polarization and (b) Twinned 180° domains formed to minimize electrostatic energy [18]. 9

2.4 Twinned 90° and 180° present in $BaTiO_3$ [18]. 10

2.5 (a) Tetragonal form of $PbTiO_3$ and the spontaneous polarization P_0, (b) converse piezoelectric effect $S = d_{33}E$, (c) direct piezoelectric effect $\Delta d = d_{33}\sigma$ and (d) $\Delta D = d_{31}T$ for $\sigma < \sigma_c$ where σ_c indicates the critical stress [18]. 10

2.6 (a) Spontaneous polarization, or electric displacement, D_0 for $PbTiO_3$, (b) ferroelectric 180° polarization switching due applied field higher than coercive field ($E > E_c$), (c) ferroelastic 90° switching due to compressive stress higher than coercive stress $\sigma > \sigma_c$ and (d) Six pinning sites for the Ti^{4+} ion in the tetragonal structure [23, 18]. 12

2.7 (a) $Pb(Zr, Ti)O_3$ phase diagram showing dependence of curie temperature T_c on the molar fraction x of Zr and morphotropic boundary and (b) coupling coefficient and piezoelectric strain coefficient for $Pb(Zr, Ti)O_3$ showing high values near MPB. (Reprinted from [12], with permission from Elsevier.) . . 12

2.8 Polarization hysteresis for hard (a) and soft (b) PZT (Reprinted by permission from Springer Customer Service Centre GmbH: [27]). 13

2.9 Comparison of spontaneous polarization of (a) single crystal and (b) polycrystalline after poling $BaTiO_3$ [18]. 15

2.10 (a) Unpoled polycrystalline ferroelectric materials, (b) changes in 180° domains, (c) in 90 ° domains as a result of poling and (d) ferroelastic switching due to applied stress greater than coercive stress [18, 37]. 16

2.11 (a) Hysteresis field-polarization relation and the linear approximation at point B, where there is remanent polarization and (b) hysteresis field-strain relation and linear approximation at point B and F, where there is remanent strain [18, 12]. 16

2.12 Hysteresis shown in (a) stress-strain relation and (b) stress-polarization relation due to 90° switching caused by compressive stress [18]. 17

2.13 Characteristic features of PMN. (a) Dielectric dispersion as a function of temperature and frequency, (b) hysteresis as a function of temperature and (c) Optical and x-ray evidence of absence of macroscopic phase change around the dielectric maximum temperature (Reprinted by permission from Springer Customer Service Center GmbH: [40]). 19

2.14 Absence of aging in 0.9 PMN:0.1 PT over a range of temperatures and at different frequencies after 1,000 h of aging at 20°C (Reprinted by permission from Springer Customer Service Center GmbH: [40]). 20

2.15 (a) Electrostrictive strain as a function of applied electric field in 0.9 PMN:0.1 PT, where the solid line represents the d_{33} slope and the dotted line shows the d_{33} slope for a PZT , (b) illustration of the relaxor polar nano region ((a) Reprinted from [43] with permission from SAGE and (b) adapted from [37], with permission from Elsevier). 20

2.16 Schematic of different piezoelectric polymer categories: bulk piezopolymers, piezoelectric polymer composites and piezo-, pyro- and ferro-electrets (images from [44], and adapted from [45] ©2005 IEEE). 22

2.17 Illustration of different chain conformations where T means trans and G means gauche torsional arrangements with substituents taking 180° and ±60° to each other respectively (Reprinted from [50] with permission from John Wiley and Sons). 23

2.18 (a) Polarization hysteresis loops of P(VDF-TrFE) 50/50 copolymer at room temperature (left) before and (right) after irradiation, (b) Polarization hysteresis loops measured at two temperature showing the increased remanent polarization and hysteresis at low temperatures and (c) (top) Strain-field dependence of irradiated P(VDF-TrFE) 50/50 copolymer and (bottom) electrostrictive relation between strain and polarization, where P≥0 strains overlap P≤0 strains (From [54]. Reprinted with permission from AAAS). . . . 24

2.19 Overview of piezocomposite connectivities ([45] ©2005 IEEE). 26

2.20 Comparison of figure of merit ($d_h g_h$) of various piezoelectric composites ([45] ©2005 IEEE). 26

2.21 Manufacturing process for voided polymers by (top) stretching or (bottom) direct film foaming (Reprinted from [80] with John Wiley and Sons). . . . 28

2.22 (a) Effect of longitudinal expansion on volume of actuator and (b) electrode configuration of longitudinal piezoelectric stack [84]. 29

2.23 Stroke-force relation of a preloaded piezoelectric actuator (Reprinted from [85], with the permission of AIP Publishing.). 30

2.24 Polarization-Field P(E) and Strain-Field S(E) at room-temperature under different electric field amplitudes 1 kV mm⁻1, 2 kV mm⁻1 and 3 kV mm⁻1 (Reprinted from [87], with permission from Elsevier). 31

2.25 Output displacement creep with an applied step input (Reprinted by permission from Springer Customer Service Center GmbH: [88]). 31

2.26 Polarization reversal/reorientation model for explaining dielectric, mechanical and piezoelectric losses (Reprinted by permission from Springer Customer Service Center GmbH: [91]). 32

2.27 Strain-field relation for soft and hard PZT showing large-signal hysteresis (Reprinted by permission from Springer Customer Service Centre GmbH: [27]). 33

2.28 A vertical (a) and curved (b) morphotropic phase boundary (Reprinted from [93] with permission from John Wiley and Sons). 34

3.1 An illustration of the Joule effect, where T_c is curie temperature (Reprinted from [107], with permission from Elsevier). 38

3.2 An illustration of the Villari effect, where T_c is curie temperature and S is stress (Reprinted from [107], with permission from Elsevier). 38

3.3 (a) Single domain and flux lines, (b) formation of 180° domains to reduce magnetostatic energy and (c) formation of 90° closure domains resulting in zero magnetostatic energy [106]. 39

3.4 Domain structure of a magnetostrictive material (Reprinted from [107], with permission from Elsevier). 39

3.5 Orientation of Terfenol-D crystals ([109] ©1990 IEEE). 40

3.6 Initial magnetization process and dominant mechanism in the $(1\bar{1}0)$ plane of single crystal Terfenol-D due to applied field H in $[11\bar{2}]$ direction (left) and the magnetization flux-field relation(right) at (a) demagnetized state, (b) domain growth from domain wall motion, (c) rotation of moments to easy axis $[11\bar{1}]$, (d) saturation rotation of moments to align with applied field (left [18] and right [106]). 41

3.7 A comparison of ferromagnetic magnetic flux B and strain S response to magnetic field (Reprinted from [107], with permission from Elsevier). . . . 42

3.8 Schematic of ferromagnetic material flux density and applied field magnetic history to an applied stress ([110] ©1990). 43

3.9 Hysteretic and anhysteretic magnetic flux density and applied field relation dependence upon applied stress from 100 MPa to -400 MPa ([110] ©1990). 43

3.10 Stress-strain response of Terfenol-D and Galfenol at constant magnetic field ([115] ©2007 IEEE). 46

3.11 An illustration of the magnetomechanical coupling coefficient [97]. 47

3.12 Terfenol-D k_{33} and d_{33} coefficients dependence on applied stress (Reprinted from [97], with permission from Elsevier). 48

3.13 Cross section of a typical GMM actuator (Reprinted from [99], with permission from Elsevier). 49
3.14 (a) Magnetostriction and (b) magnetic Field against applied field at various stresses. ISU transducer, 12.7 mm diameter solid material, near-DC frequency of operation [124]. 50
3.15 Magnetostriction (a) without and (b) with magnetic biasing [99]. 51
3.16 Strain-applied field minor loops. Bias Condition (left to right): 5.2 MPa, 24 kA/m (0.75 ksi, 300 Oe); 6.9 MPa, 33.2 kA/m (1.0 ksi 415 Oe); 8.6 MPa 38.4 kA/m (1.25 ksi, 480 Oe). AC Drive Fields (top to bottom): 4, 8, 16 kA/m (50, 100, 200 Oe). ISU 12.7 mm diameter rod transducer, 0.75 Hz excitation [125]. 51
3.17 Quasi-static temperature effects of Terfenol-D at 13.3 MPa Compressive Stress (Reprinted from [126] with permission from SAGE). 52
3.18 Steady-state position of PZT and Galfenol without temperature control (Reprinted from [128] with permission from SPIE). 52

4.1 (a) Forward transformation of austenite to twinned martensite from cooling and (b) reverse transformation from twinned martensite to austenite from heating, where T is temperature [2]. 56
4.2 (a) Detwinning process and (b) shape memory effect from unloading of detwinned martensite and heating to austenite after load removal [2]. 56
4.3 Thermally induced phase transformation at a stress above detwinning finish stress σ_f^{cr} from austenite to detwinned martensite [2]. 57
4.4 (a) Mechanically-induced forward and reverse transformation above A_f and (b) representation of stress-strain behavior of the superelastic effect [2]. . . 57
4.5 Stress-temperature behavior of a SMA showing SME and SE (or transformation pseudoelasticity) (Reprinted from [136], with permission from Elsevier). 58
4.6 The effect of temperature on the stress-strain relationship of a Ti-49.8Ni alloy annealed at 673 K after 1 hr of cold work (Reprinted from [136], with permission from Elsevier). 59
4.7 Stress-strain-temperature behavior of a NiTi SMA (Reprinted from Springer Customer Service Centre GmbH: [2]). 60
4.8 (a) Differential scanning calorimetry output and (b) constant-load strain-temperature relationship with the transformation temperatures determined through tangent method [138]. 61
4.9 An example of the residual strain evolution of a thermally cycled $Ti_{50.1}Ni_{49.9}$ SMA at 150 MPa (Adapted from [143], with permission from Elsevier). . . 62
4.10 Illustration of (a) the effect of annealing time on R-phase presence, (b) stress-strain relationship and (c) resistance-temperature relationship (Reprinted by permission from Springer Customer Service Center GmbH: [146] and reprinted from [145] with permission from SAGE). 63

4.11 Temperature range of different SMA compositions. Automotive preferred temperature range denoted (Reprinted from [149] with permission from SAGE). 64
4.12 Stress-strain relationship of the single-direction actuator design with (a) free recovery and (b) constrained recovery (Reprinted from [149] with permission from SAGE). 66
4.13 Stress-strain relationship of the bias-force actuator design with (a) bias spring and (b) deadweight (Reprinted from [149] with permission from SAGE). 67
4.14 Antagonistic designs for (a) linear and (b) rotary motion (Reprinted from [149] with permission from SAGE). 67
4.15 Major hysteresis loop behavior of heating and cooling resistance-displacement curve. The inset represents an approximation of the wire temperature over time (Reprinted from [161] with permission from SAGE). 68
4.16 Arrangement of SMA wires on end plate (Reprinted from [149] with permission from SAGE). 70
4.17 Strain and number of cycle relationship for thermomechanical cycles of NiTi SMA wire at 200 and 300 MPa and annealed at 450°C for 15 min. RD indicates residual plastic deformation and RS indicates recovery strain (Reprinted by permission from Springer Customer Service Centre GmbH: [177]). 72
4.18 Strain and number of cycles relations for thermomechanical cycles of NiTi SMA wire at 200 MPa with 2 and 4 % recovered strain. The wire was annealed at 450° C for 15 min (Reprinted by permission from Springer Customer Service Centre GmbH: [177]). 73
4.19 Strain and number of cycles showing fatigue life as a function of maximum temperature of the wire which is at stress of 200 MPa (Reprinted by permission from Springer Customer Service Centre GmbH: [177]). 74

5.1 A panel of length ℓ, width b, and thickness t, loaded in bending by a force F per unit width (Reprinted from [179], with permission from Elsevier). . . 77
5.2 A generalized model of a transducer with A_1 and T_1 are the input across and through variables, and A_2 and T_2 are the output across and through variables 78
5.3 Anatomy of an actuator system with a dashed box indicating focus. Based on [183]. 80
5.4 Actuation Stress versus actuation strain of various actuator technologies. Heavy lines indicate upper limit of performance. Low-strain piezoelectrics are Quartz (SiO_2), Lithium Niobate ($LiNbO_3$), Lithium Tantalate ($LiTiO_3$) (Reprinted from [185] by permission of the Royal Society). 83
5.5 Comparison of output energy density per unit volume of 6 induced-strain actuators with casing and prestress mechanism [188]. 83

5.6 Volumetric power versus frequency of various actuator technologies. Lines of slope +1 indicate equal volumetric work output per cycle (Reprinted from [185] by permission of the Royal Society). 85

5.7 Anatomy of a Sensor System. Dashed box indicates scope of work (Adapted with permission from [196]). 86

5.8 Anatomy of Energy Harvesting System. Dashed box indicates scope of work. 88

5.9 A typical power consumption of a sensor node. Due to consumption not matching harvester output, an energy buffer and power management is needed (Reprinted from [198], with permission from Elsevier). 89

6.1 An illustration of cantilever piezoelectric energy harvester (Reprinted from [221], with permission from Elsevier). 97

6.2 Decision hierarchy for energy harvester selection. The top is the goal. Second row is the criteria, where EO is energy output, ρ is density, DC is design complexity. Third row is the sub-criteria, where k^2Q_m is the maximum power, η is efficiency, Z_e is the boolean value for impedance matching, and BPP is the boolean value for requiring bias field, prestress mechanism and a pickup coil. 100

6.3 Schematic of a piezoelectric ultrasound transducer (Adapated from [45] ©2005 IEEE). 106

6.4 Impulse response of a lightly backed (Z = 4 Rayl) piezoelectric ultrasound transducer without and with matching layer ([45] ©2005 IEEE). 107

6.5 Impulse response of a light backed (Z = 4 MRayl) and heavy backed (Z = 10 MRayl) piezoelectric ultrasound transducer ([45] ©2005 IEEE). 108

6.6 Decision hierarchy of the ultrasound material selection, where TP is transmitter performance, RP is receiver performance, DC is decision complexity, TC_{max} is the maximum transmission coefficient, T_c is the curie temperature, R_{VS} is the receiver voltage sensitivity, R_{SNR} is the receiver signal-to-noise ratio, k_t is the transducer thickness coupling, Z_a is the number of matching layers and Z_e is electronic matching. 112

Chapter 1

Introduction

Active material transducers are materials that convert energy between the electrical and mechanical domains. Some of these transducers take advantage of heat generation from the electro-caloric effect to cause displacement through phase transformations while others are materials that have an unintuitive response to a physical input. Through this link, these transducers can function as multiple different engineering devices: such as an actuator with an electrical input, or a sensor and an energy harvester with a mechanical input.

These active materials provide new functionality in engineering and industrial applications. Due to their transduction mechanism, self-sensing actuator systems are feasible, which reduces the cost and component complexity of actuation systems. Embedding these transducers in structures allows for structural health monitoring and self-healing properties. As well, their ability to convert ambient energy into electrical energy allows for long-lasting self-powered wireless networks to be achievable. These transducers and devices have garnered interest from academic, industrial and commercial communities resulting in large number of papers, patents, and applications.

The transducers coupling of two domains provides advantages and disadvantages to conventional transducers. These materials require simple assemblies, weigh less and can operate in nanoscopic scale. On the other hand, the phenomenon causes complex nonlinearities, fatigue mechanisms and temperature-dependent properties. The successful implementation of active material transducers requires knowledgeable understanding of these limitations alongside skilled selection of materials. Due to this knowledge gap and inefficient material selection methods, some of these materials struggle to find a path to implementation.

1.1 Motivation

When considering whether to use conventional or active material transducers, the designer needs to compare an array of transducers which do not share similar properties. The designer who has a set of device requirements (force, stroke, frequency) is likely to either use experience, a few metrics, or rely upon commercial products that are heavily marketed.

While this approach is time effective, the selection is not chosen on the basis of device efficiency or effectiveness.

In the consideration of different designs and devices, designers lack proper tools to make an effective decision. Some academics have developed a material selection software, called the Cambridge Engineering Selector, that optimizes material properties based on designer-specified performance metrics and applied it to electromechanical transducers [1]. Although the database is useful, this program is expensive and the designer still needs to select the optimal material. Other researchers used a theoretical standpoint to create metrics based off of the material or model properties. Yet, these metrics offer a solution to a simplistic problem where there are no competing objectives that require a compromise between imperfect solutions. Therefore, it would be beneficial if there was a solution to selection of transducers that would achieve both issues: it does not require proprietary software and could make selection from a set of candidates that requires a complex decisions.

1.2 Aim and Objectives

The aim of this thesis is to assist designers in the selection of active materials for certain devices (actuators, sensors, and energy harvesters). In an effort to do this, the three most researched active materials will reviewed and their practical considerations will be highlighted. As generalized coefficients to compare across different domains are not plentiful, it will be necessary to do a review of how designers use these generalized figures of merit, whether they are useful and how to clearly select material based upon a designer set goals. Therefore, thee objective of the thesis is to do a review of transducer technology, applications and selection methods and to apply the information gathered to a couple cases to highlight the effectiveness of the solution. The specific objectives are outlined below:

1. Go through a phenomenological review of the three most researched active materials,
2. Review application selection criteria and decision making methods,
3. Through the use of a decision making algorithm, perform analysis on optimal active materials selection for an energy harvester and ultrasound transducer.

1.3 Smart Material Overview

Materials have traditionally played a structural role in engineering design. They were selected based on some favorable property that existed in the material. At first, these favorable properties were related to mechanical domain, such as mechanical strength, ductility, workability, and toughness. With improvements in material understanding and technology, material scientists could understand how to adjust the microstructure of materials to create better properties, and there was an increased demand for different domain material

properties. With the material science knowledge it became possible to tailor the material to have certain properties in different domains (mechanical, thermal, and electrical) and new materials were developed depending on the requirements at the time. Due to the drive for stronger, lighter material with specific properties, materials were developed that could achieve the structural requirements and provide other engineering functionality (electromechanical shielding or sensing). These materials are called *functional materials*. A subset of the functional materials, called *active materials*, could act as both a sensor and actuator and garnered increased interest.

Active material can operate as sensors, actuators, active dampers and energy harvesters. Due to their electrical domain response from a mechanical input they can act as sensors. Actuators are the reciprocal; they convert a non-mechanical input into a mechanical output. Active dampers are materials that adjust damping rate and stiffness through a command signal, and are quite similar to actuators. Energy harvesters are used similar to sensor but the focus is on extracting the most electrical power out of a mechanical input. Active materials mostly are materials that respond mechanically to some non-mechanical input. The benefit of these materials is there response is normally orders of magnitude higher than the response due to thermal expansion [2]. Active materials can also be divided by whether there response is reciprocal, or if the domains have direct coupling. Piezoelectric and electrostrictive (materials that couple mechanical and electrical domain), magnetostrictive (materials that couple the mechanical and magnetic domains), and shape memory alloys (materials that couple mechanical and thermal domain) are examples of directly coupled materials. This means that either domain could act as an input or output.

Active materials that are directly coupled can be also called solid-state transducers, smart materials, and so on. The advantage of a active material transducers is there is little assembly and no moving parts. It can be miniaturized and can be used in micro-electromechanical systems. They do have distinct disadvantages that are phenomenon dependent, and it is possible that some of the material implementation difficulty is based upon their effectiveness.

A BCC Research financial analysis shows that the interest in active materials is only going to grow in the coming years. The global market share totals $26.0 billion in 2014, and is projected to grow to $42.2 billion in 2019 [3]. The breakdown of the global market share of smart materials showed that the majority is related to motors and actuators (≈70%) [3]. This amount was $18.4 billion in 2014 and is projected to grow to $30.2 billion. Transducers, the second largest segment, was $4.1 billion in 2014 and will be $6.0 billion in 2019 [3].

A literature analysis of the number of publications and patents of the main smart materials (piezoelectric, magnetostrictives, shape memory alloys, and electrostrictives) indicates that piezoelectric is the most published and patented, see Table 1.1 and Figure 1.1. Even though giant magnetostrictives materials were discovered in the same decade as shape memory alloys it has less academic and commercial interest from the 1990s and onwards. It is possible that this difference in interest is that magnetostrictive materials do not have a clear implementation path, but it could be also be caused by the effectiveness of the material as an transducer.

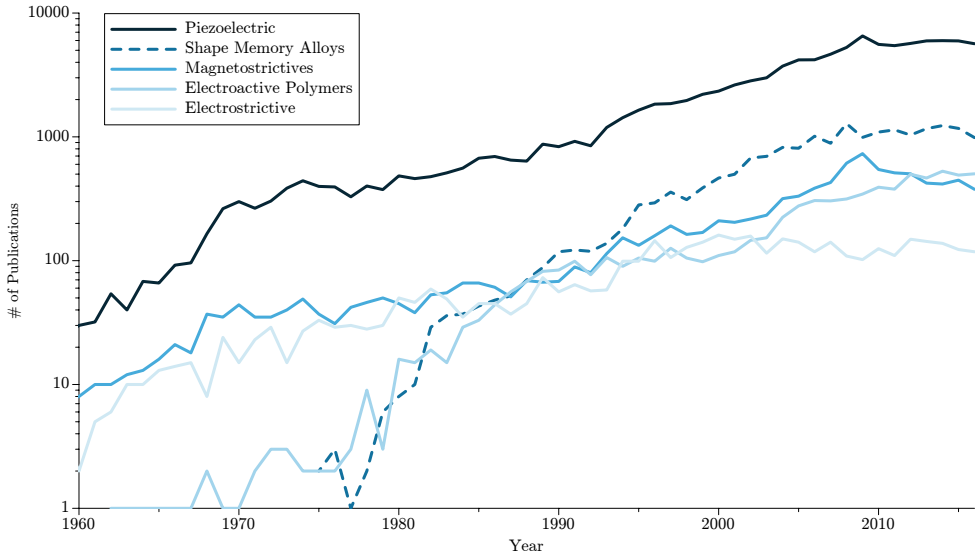

Figure 1.1: Number of publications by smart material subject

Table 1.1: Total number of publications and patents of active materials*

Material Title	Total Publications	Total Patents	Year Discovered
Electroactive Polymers	6953	22239	1990** [4]
Electrostrictive	2188	23496	1979*** [5]
Magnetostrictive	9480	37595	1971† [6]
Piezoelectric	105180	601713	1880 [7]
Shape Memory Alloy	18701	68613	1963‡ [2]

* A literature analysis carried out with Scopus using material title as search query and acronyms

** Based on the discovery of new electroactive polymers

*** Based on publications of new electrostrictive materials

† Based on the discovery of giant magnetostrictive materials

‡ Based on the discovery of Nitinol

Therefore, it is imperative to fully comprehend the phenomenon and limitations of these materials. In this work, the focus will be on the three most researched active materials: piezoelectric, magnetostrictive, and shape memory alloys.

1.4 Thesis Organization

This thesis studies the optimal selection of different technology (piezoelectric, magnetostrictive and shape memory alloy) in different roles (actuation, sensing and energy harvesting). In Chapter 2, different piezoelectric materials are introduced through the timeline of phenomenological understanding before an overview of important design features, application considerations and limitations of piezoelectric operation. Chapter 3 describes the magnetostrictive phenomenon prior to an overview of the application considerations and limitations of giant magnetostrictive material operation. In Chapter 4, an overview of the phenomenon of shape memory alloys is discussed and is followed by discussion of design consideration, application considerations and limitations of shape memory alloys. Following the material overview chapters, in Chapter 5 the discussion of how optimal materials are selected and critiques current intrinsic figures of merit. The application of the material selection method and the material covered in Chapter 2–4 are covered in Chapter 6. Chapter 7 concludes the thesis and indicates the future work.

Chapter 2

Piezoelectrics

Piezoelectric ceramics are the most prevalent and well-known active material. The piezoelectric phenomenon was first discovered in 1880 by the Curie brothers in their study of single crystal quartz [7]. The first large-scale use of piezoelectrics was in World War II where the demand quickly outpaced the supply of natural quartz [8]. Due to the high demand and low stock, there was interest in manufacturing synthetic piezoelectrics. This interest fueled the synthesis of new piezoelectric ceramics, such as lead zirconate titanate (PZT), and discovery new piezoelectric phenomena. These discoveries allowed for new applications and developments in piezoelectricity. Piezoelectrics can be found everywhere from our watches, printers, and cellphones to our cars, aircrafts, and space crafts.

In general transduction terms, piezoelectric ceramics are known to have high natural frequency, good linearity, nano-scale resolution, high power output and low power consumption. Its disadvantages are its low maximum strain, low frequency limitations and high electrical impedance. Piezoelectrics are micro devices as their maximum strain is roughly 0.10%–0.15% [9]. Therefore, the actuator applications are limited by the minuscule displacement that piezoelectrics can achieve. Efforts have been made to improve the linear transduction range using mechanical stroke amplification methods, stick-slip linear actuators and traveling-wave rotational actuators [10].

Piezoelectric actuators are commonly found in precision instrumentation, speakers and ultrasonic cleaning. Piezoelectric sensors are widely used, where the most common usages are in accelerometers, gyroscopes, pressure sensors, dynamic force sensors, strain gauges and timers. Common piezoelectric energy harvesters are gas lighters and electric switches.

Although the field of piezoelectrics has been known for a while, new piezoelectric materials are continuously being introduced with different structures which hinders proper piezoelectric selection. To understand how to properly implement piezoelectrics, it is useful to understand the phenomenon, the different physical properties of the most common piezoelectric phenomenon and the application considerations. With this knowledge, those designers would be more capable of selecting the proper criteria which will assist in the optimal piezoelectric selection.

2.1 Piezo-, Pyro- and Ferro-electricity

Three phenomena explain the development of electric fields within dielectric materials. Piezoelectricity which is the polarization of a dielectric due to mechanical energy [10]. A subset of piezoelectric materials exhibit spontaneous polarization by *uniform* heating, which is called pyroelectricity. Ferroelectrics are a subset of pyroelectrics that exhibit a domain structure below its curie temperature and spontaneous polarization that can be reoriented by applied fields. These three phenomenon and their relation to each other are described in Figure 2.1.

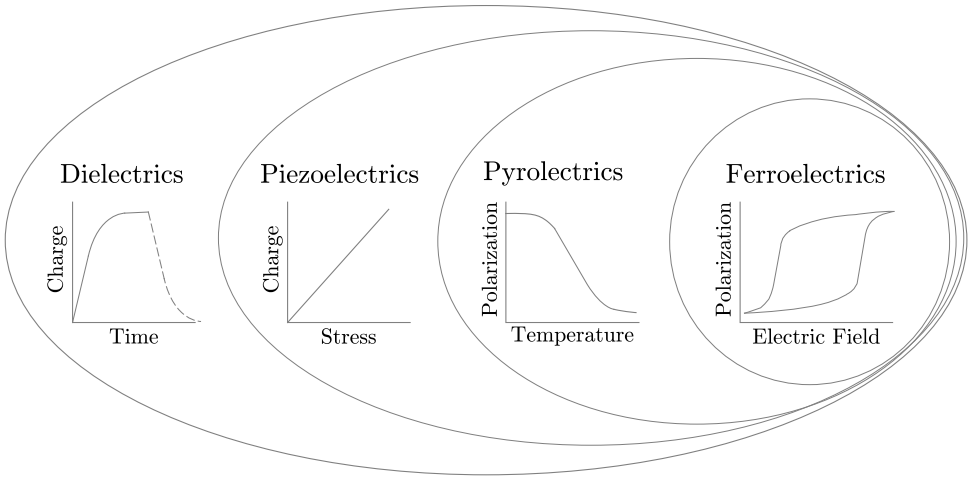

Figure 2.1: Classes of functional dielectrics [11].

Piezoelectricity in crystalline material relies on the a lack of symmetry in the unit cell. On the basis of orientation symmetry, there are total of 32 crystal symmetry point groups, where a point grouping is based on orientation only. Of these groups, there are 11 centrosymmetric classes and 21 noncentrosymmetric classes, a crystal class which has no center of symmetry. Twenty of the noncentrosymmetric classes exhibit piezoelectricity while the last one does not exhibit it because of has other symmetry elements. Ten of the 20 noncentrosymmetric piezoelectric classes exhibit heat-generated spontaneous polarization, where spontaneous indicates there is permanent polarization in a unit cell, and describes pyroelectric effect [12]. A subgroup of those 10 noncentrosymmetric classes also exhibit reversible polarization, which occurs at certain applied electric fields and indicates the ferroelectric effect. Piezoelectricity, pyroelectricity, and ferroelectricity are normally found in ceramics, but can be found in polymers and voided polymers.

Materials that exhibit solely the piezoelectric phenomenon are used for sensors due to their decreased temperature sensitivity. Ferroelectrics are the most commonly used piezoelectric in other applications, particularly PZT types. Ferroelectrics ceramics are designed to have favorable piezoelectric properties but as a result of being polycrystalline have increased nonlinearity and hysteresis.

2.2 Physical Properties of Piezoelectric Materials

The history of piezoelectrics can be described with the discovery of ferroelectric materials and theories. The most important discoveries where the discovery of barium titante ($BaTiO_3$) and lead zirconate ($Pb(Zr, Ti)O_3$), the discovery of the morphotropic phase boundary concept that later fueled the discovery of relaxor ferroelectrics and the invention of ferroelectric polymers [13]. Each of these discoveries created a significant increase in the research effort and all have found large scale commercial usage.

Barium titanate is a simple ferroelectric material that was discovered in the late 1940s. Its simple structure allows for the discussion of the atomic- and nano-scale ferroelectric phenomena. As the bulk temperature goes below the curie temperature, the bulk material exhibits a phase change from paraelectric cubic to ferroelectric tetragonal that allows for spontaneous polarization. This is exhibited by two phenomena at the atomic scale and the nanoscopic scale. At the atomic scale and with small inputs, induced lattice strain displaces ions and creates a stronger electric dipole polarization, which describes the direct piezoelectric phenomenon. At higher inputs, the induced lattice strain can cause ferroelectric switching and the higher energy ferroelastic switching. The discovery of PZT-type ferroelectrics in 1950s was an important turning point. It introduced the widely used PZTs which have excellent properties and a high curie temperature but suffer hysteresis predominantly from domain reorientation. Through the modification of the composition and addition of donors or cations, hard and soft PZTs were created and the morphotropic phase boundary concept was discovered. It provided for fruitful discovery of relaxor ferroelectrics in 1990s by Park and Shrout that exceed the PZT properties [14]. Separately, the discovery of piezoelectric polymers in 1969 greatly expanded the range and possibilities of piezoelectrics [15].

The term ferroelectricity was coined due to the similarity of ferroelectrics response to electric field to ferromagnetics response to magnetic field [12] . Yet, the term is somewhat misleading. Ferromagnetism occurs as a result of magnetic dipoles in each atom, whereas ferroelectricity dipoles are present in the unit structure of the crystal [16]. Therefore, the term ferro- is not used to indicate relation to iron, as ferromagnetics do, but to indicate a similar characteristics to ferromagnetics [17]. Structural similarity is due to the ferroelectrics exhibiting a polar structure like ferromagnetics [17]. Property similarity is due to ferroelectric exhibiting broad hysteresis curves caused by large spontaneous polarization [17].

2.2.1 Barium Titanate-Type Ferroelectrics

Barium titanate ($BaTiO_3$) was the first major ferroelectric breakthrough. It belongs to the family of ABO_3 perovskite mineral $CaTiO_3$ structure, where A and B are metals [13]. For ferroelectric materials, electric polarization occurs spontaneously, without an applied electric field, as a result of a phase change below the curie temperature T_c. The phase change results in a separation of the centroid of the positive and negative charges and thus a polar structure [12]. For example, $BaTiO_3$ exhibits a cubic structure above curie tem-

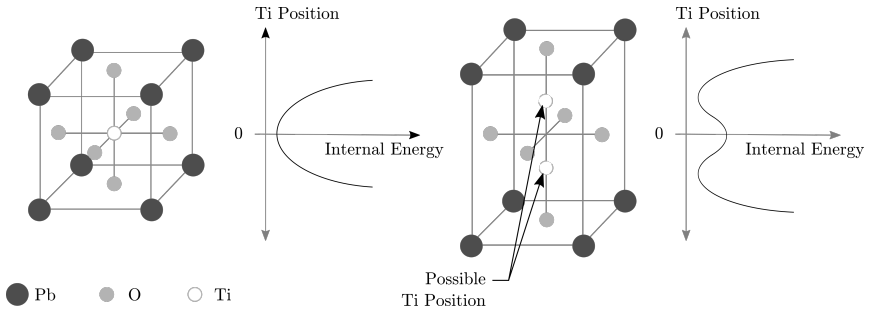

Figure 2.2: $BaTiO_3$ perovskite structure (a) above and (b) below curie temperature T_c. Internal energy as a function of Ti position along the x_3 axis in the (c) paraelectric $T > T_c$ and (d) ferroelectric $T < T_c$ phases [18].

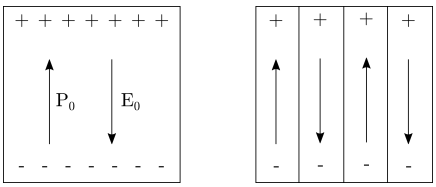

Figure 2.3: (a) Surface charge due to a spontaneous polarization and (b) Twinned 180° domains formed to minimize electrostatic energy [18].

perature, Figure 2.2(a). In this cubic centrosymmetric structure, $BaTiO_3$ is a paraelectric, it exhibits polarization only if an electric field is applied. Below the curie temperature, the structure changes to noncentrosymmetric (e.g. $BaTiO_3$ changes to tetragonal, orthorhombic, rhombohedral), Figure 2.2(b). Due to the relative change in the position of Ti^{4+} and O^{2-} ions, the unit cell has spontaneous polarization.

As shown in Figure 2.2 (c) and (d), the internal energy pinning center of the paraelectric and ferroelectric unit cells are different. Above the curie temperature, there is one pinning center. In the noncentrosymmetric unit cell, there are two pinning centers that results in two distinct positions for the Ti^{4+} ions. With enough electric energy or mechanical energy, the ion can shift between the pinning centers and result in dipole switching, in this case of Figure 2.2 it is called 180° switching. The dipole switching results in a region called the burst region where polarization changes signs and magnitude rapidly over a small input electric field.

Due to this spontaneous polarization, the material forms surface charges P_0 and a depolarizing field E_0, see Figure 2.3. As a result of the minimization of electrostatic energy, the dipoles align in 180° twinned domain structure — domains are regions in which there is uniform polarization [18].

As the material cools down from paraelectric to ferroelectric phases, a second mechanism is present due to the thermal stresses. Thermal stresses will not impact the 180° twinned domains structure but will form 90° domains to minimize ferroelastic energy [18]. This forms another twinned structure as shown in Figure 2.4.

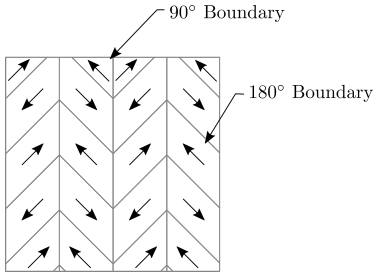

Figure 2.4: Twinned 90° and 180° present in $BaTiO_3$ [18].

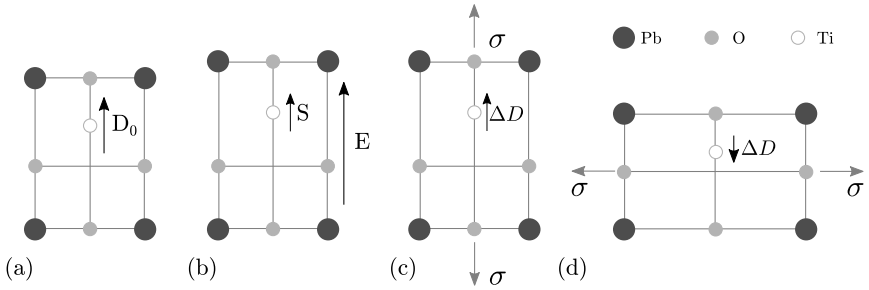

Figure 2.5: (a) Tetragonal form of $PbTiO_3$ and the spontaneous polarization P_0, (b) converse piezoelectric effect $S = d_{33}E$, (c) direct piezoelectric effect $\Delta d = d_{33}\sigma$ and (d) $\Delta D = d_{31}T$ for $\sigma < \sigma_c$ where σ_c indicates the critical stress [18].

2.2.2 Direct and Converse Piezoelectric Effect

The direct piezoelectric effect is the phenomenon where the material exhibits a linear and reversible dielectric polarization caused by an applied stress. The converse piezoelectric effect is a linear and reversible strain generated from an applied electric field. At low input energy, a ferroelectric response is similar to a piezoelectric and therefore is shown in Figure 2.5. As shown in Figure 2.5 (a) and (b), the application of a small electric field results in change of ionic position which causes lattice deformation. The direct piezoelectric effect is the opposite where the application of a low stress produces a change in polarization.

The accepted model to describe piezoelectric ceramic behavior was created in 1966 and revised in 1987 by the IEEE Ultrasonics, Ferroelectrics and Frequency Control Society [19]. This linearized model consisted of two constitutive equations that couple the mechanical and electrical domains and describes the piezoelectric behavior. The quasistatic linear piezoelectric constitutive equations are represented in the following form, where σ is used instead of T to reduce confusion with temperature:

$$\begin{aligned} S_i &= s_{ij}^E \, \sigma_j + d_{mi} \, E_m \\ D_m &= d_{mi} \, \sigma_i + \epsilon_{mk}^T \, E_k \end{aligned} \tag{2.1}$$

where S, σ, E, D represents the strain tensor (m/m), stress tensor (N/m^2), electrical displacement vector (V/m), and energy field vector (C/m^2), and s, d, ε represents the elastic compliance matrix (m^2/N), the matrix of piezoelectric constant $(m/V$ or $C/N)$, and

the permittivity constant (F/m). The superscript E, as in s_{ij}^{E} represents measurements taken when the electrodes are in short circuit, or $E = 0$, [12] and the superscript σ, as in ϵ_{mk}^{σ} represents measurements taken at zero stress and the subscripts $i, j = 1, 2, \ldots, 6$ and $m, k = 1, 2, 3$ represent different vector dimensions of the material coordinate system [20]. Depending on the axis of the applied stress, the degree of polarization changes. The piezoelectric strain coefficient d_{mi} indicates the conversion between mechanical and electrical domains, where m indicates the direction of polarization and i indicates the direction of applied stress. The two main stress and polarization configuration are called the piezoelectric 33-mode and 31-mode modes. The 33-mode is used in actuators, and 31-mode is normally used in bending actuators and energy harvesters.

The linear direct and converse piezoelectric effects occurs in materials that only exhibit piezoelectric effect. Even though ferroelectrics exhibit much different phenomenon, these equations act as a simplification and are used extensively. Therefore, when a designer uses the constitutive equations and quasistatic coefficients for ferroelectric ceramics it assumes just atomic scale phenomenon (lattice strain). In reality, most ferroelectrics respond by a mixture of atomic scale (lattice strain), nano-scale (reversible and irreversible domain wall motion) and micro-scale (intergranular coupling) phenomena [21].

2.2.3 Ferroelectric and Ferroelastic Switching

Ferroelectric switching occurs when an applied field is large enough to exceed coercive field E_c. The coercive field is the electric field needed to reduce polarization to zero. When the applied field is larger than the coercive field, the Ti^{4+} ion has enough energy to switch to the other pinning centers aligned with the field, which produces 180° ferroelectric polarization switching as shown in Figure 2.6 (a) to (b). Ferroelectric 180° domain switching, which does not involve elastic deformation, is energetically easier than ferroelastic switching, which consists of significant elastic deformation [22].

Ferroelastic switching occurs when the stress exceeds the coercive stress σ_c and causes reorientation of the Ti^{4+} in the pinning site closest to the applied stress, which produces 90° ferroelastic polarization switching as shown in Figure 2.6 (a) and (c). In total there are six possible pinning sites, see Figure 2.6(d), in the tetragonal structure that indicate possible ferroelectric and ferroelastic switching mechanisms.

2.2.4 PZT-type Ferroelectrics and the MPB Concept

Lead zirconate $(Pb(Zr, Ti)O_3$ or PZT) is arguably the most popular ferroelectric compound used in active materials. PZT is ferroelectric compound composed of $PbTi_{1-x}O_3$ and $PbZr_xO_3$ where the composition x is chosen for maximum piezoelectric coupling coefficient. The effect of composition is shown in Figure 2.7 (a) where the phase diagram of $PbTiO_3$ and $PbZr_xO_3$ shows the dependence of the curie temperature on the molar fraction of Zr. In Figure 2.7 (b), the larger piezoelectric coupling coefficient and dielectric constants occurs near the morphotropic phase boundary between rhombohedral and tetragonal structures. These higher piezoelectric coefficients, Figure 2.7 (b), indicate why PZT is preferred to

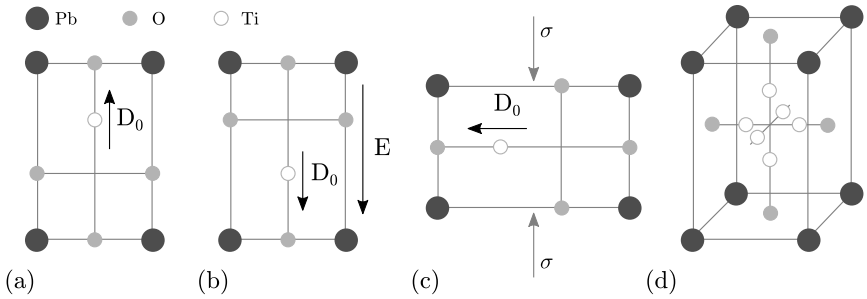

Figure 2.6: (a) Spontaneous polarization, or electric displacement, D_0 for $PbTiO_3$, (b) ferroelectric 180° polarization switching due applied field higher than coercive field ($E > E_c$), (c) ferroelastic 90° switching due to compressive stress higher than coercive stress $\sigma > \sigma_c$ and (d) Six pinning sites for the Ti^{4+} ion in the tetragonal structure [23, 18].

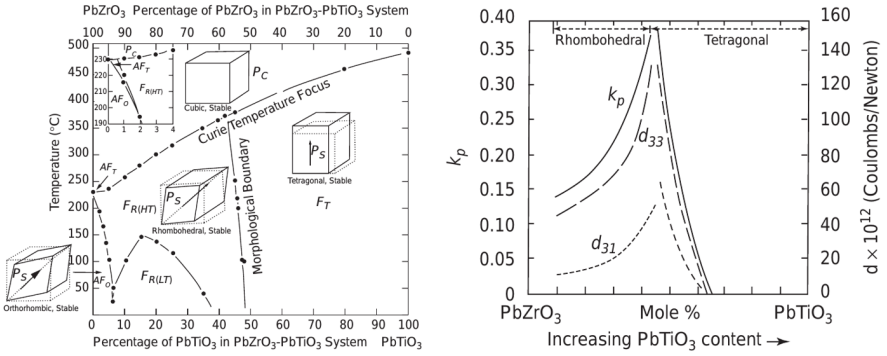

Figure 2.7: (a) $Pb(Zr, Ti)O_3$ phase diagram showing dependence of curie temperature T_c on the molar fraction x of Zr and morphotropic boundary and (b) coupling coefficient and piezoelectric strain coefficient for $Pb(Zr, Ti)O_3$ showing high values near MPB. (Reprinted from [12], with permission from Elsevier.)

$PbTiO_3$ and the higher curie temperature (250°C to 350°C) indicates why PZT is preferred to $BaTiO_3$ (T_c of 123°C) [18, 24].

The concept that explains the peak in piezoelectric properties at a certain composition is called the morphotropic phase boundary (MPB) concept. In PZT, the compositions near the MPB consist of both rhombohedral and tetragonal phases, which gives a total of fourteen possible polarization directions (6 from tetragonal and 8 from rhombohedral). The large number of polarization directions allows for larger domains orientation with the applied field and thus higher piezoelectric properties [25].

2.2.4.1 Soft and Hard PZT

PZT materials have been doped to provide better application-specific properties. The exact properties of PZTs are controlled by specifications. PZT specifications are dictated by the Piezoelectric Ceramic Material and Measurements Guidelines for Sonar Transducers, MIL-STD-1376B, which classifies hard doped PZT as DoD Type I (PZT 4) and Type III (PZT 8), and soft doped PZT as DoD Type II (PZT 5A) and Type VI (PZT 5H) [26].

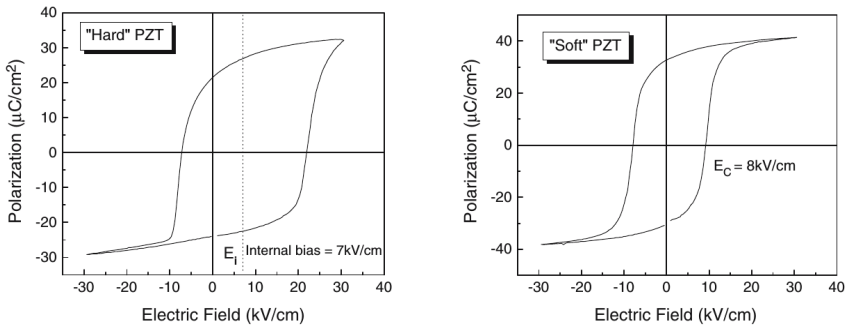

Figure 2.8: Polarization hysteresis for hard (a) and soft (b) PZT (Reprinted by permission from Springer Customer Service Centre GmbH: [27]).

Generally, a small substitution near the MPB of a small amount of cations (1–2 mol%) favorably modifies the dielectric and piezoelectric properties [27]. By doping with lower valance cations, such as replacing Ti^{+4} or Zr^{+4} with Fe^{+3}, or Pb^{+2} with K^{+1}, there is reduced domain wall mobility. This hardening effect results in reduced piezoelectric constant and dielectric constant and loss while causing an increase in the coercive field and the mechanical quality factor (the inverse of mechanical loss). As well, the electric resistivity is reduced. Typically, the 'hard' doped PZTs are used for high power and high voltage applications. As shown in Figure 2.8, the ability to introduce an internal bias is the reason for the increased coercive field [27].

When PZT is doped with donors, the piezoelectric constant, dielectric constant, resistivity and loss increase while the coercive field and mechanical quality factor decrease. The substitution of Pb^{+2} with La^{+3} and Ti^{+4} or Zr^{+4} with Nb^{+5} results in increased domain wall mobility. These materials are electrically and mechanically 'soft' and are typically used in ultrasound transducers, pressure sensors, and actuators due to their high resistivity and coupling coefficient. Soft PZTs are the most common. In 2014, a survey showed that 94.5% of all piezoelectric actuators consisted of bulk soft PZT [28].

An overview of material properties of popular piezoelectric ceramics is shown in Table 2.1. Although these numbers are fixed, manufacturers generally provide large tolerances for different coefficients [29]. For example, Noliac, a piezoelectric ceramic supplier, indicates a fairly conservative tolerance of ±10% for dielectric properties (tan δ and ϵ^T), ±5% for electromechanical properties (k and d coefficients) and ±5% for physical properties (Q_m, T_C, ρ and s coefficients) [30]. From Table 2.1, a list, shown below, from Jaffe and Berlincourt was created that highlights qualitative properties of the coefficients [31]:

1. High piezoelectric coupling: PZT-5H
2. High permittivity: PZT-5H
3. Low permittivity: PZT-7A
4. High mechanical Q: PZT-6B and PZT-8
5. Low dielectric loss at high electric field: PZT-8

Table 2.1: Brief overview of conventional piezoelectrics and piezoelectric ceramics properties

Material	T_C (°C)	k_{33} —	k_{31} —	$\epsilon_{33}^T/\epsilon_0$ —	$\epsilon_{11}^T/\epsilon_0$ —	d_{33} (pC/N)	d_{31} (pC/N)	s_{33}^E ($10^{-12}m^2/N$	s_{11}^E ($10^{-12}m^2/N$	E_C (kV/cm)	Q_m —	tan δ —	Ref.
α Quartz	573	0.11	—	4.6	4.6	—	—	—	—	—	10^4–10^6	—	[32, 33, 34]
AlN	>1000	0.23	—	11.9	10	5	-2	2.824	2.854	—	2490	—	[32, 11, 33]
CdS	—	0.26	—	10.33	9.53	10.3	-5.18	16.97	20.69	—	1000	—	[11, 32]
GaN	—	—	—	10.5	11.2	3.7	-1.9	2.915	3.326	—	2800	—	[11, 35]
ZnO	—	0.48	—	11	8.84	12.4	-5	6.94	7.86	—	1700	—	[11, 33, 32]
$BaTiO_3$	115	0.5	-0.21	1700	1450	190	-78	9.3	9.1	0.4	300	0.01	[31, 27]
$PbTiO_3$	470	0.45	—	190	—	56	—	—	—	—	1300	0.02	[36]
PZT 4 (Type I)	328	0.7	-0.33	1300	1475	289	-123	15.5	12.3	>1	500	0.004	[31]
PZT 5A (Type II)	365	0.705	-0.34	1700	1730	374	-171	18.8	16.4	0.7	75	0.02	[31]
PZT 5H (Type VI)	193	0.75	-0.39	3400	3130	593	-274	20.7	16.5	0.4	65	0.02	[31]
PZT 8 (Type III)	300	0.62	-0.295	1000	—	218	-93	13.9	11.1	1.5	1000	0.004	[31]

2.2.5 Poled Polycrystalline Materials

So far the discussion has centered on lattice strain which describes the atomic phenomenon, but there is also a nanoscopic phenomenon that creates the ferroelectric response. Ferroelectrics are polycrystalline ceramics that have reversible spontaneous polarization. Even though the lattice of a ferroelectric is polar, the unpoled polycrystal bulk is apolar due to the random orientation of grains and domains [12]. Furthermore, the random orientation of domains and the limitation of possible polarization directions results in reduction of the saturation polarization of the bulk poled polycrystalline ferroelectric. This results in approximately half the saturation polarization of polycrystalline $BaTiO_3$ in comparison to single crystals, see Figure 2.9 [18].

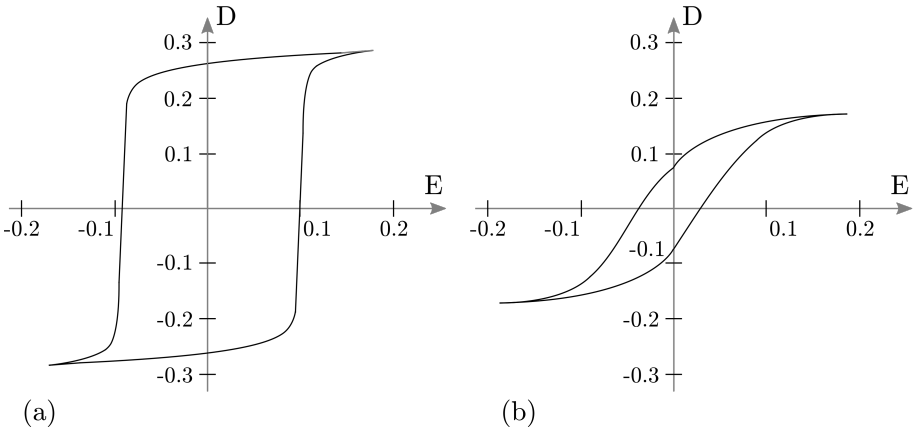

Figure 2.9: Comparison of spontaneous polarization of (a) single crystal and (b) polycrystalline after poling $BaTiO_3$ [18].

In order to fully utilize polycrystalline ferroelectric materials, poling needs to occur near the curie temperature. Poling is a process of applying high DC fields at temperatures near curie temperature that causes dipole reorientation, see Figure 2.10 (a)–(c). Typically, the poling aligns the polar vector with the x_3 axis. In Figure 2.10 (d), the ferroelastic switching that occurs above σ_c is shown.

2.2.6 Hysteresis and Constitutive Nonlinearities

Lattice strain and domain wall displacement represent nearly the complete piezoelectric effect — for a discussion on intergranular coupling read Pramanick et al. [21]. A essential property of ferroelectric materials is the effect domain switching has upon the relation between the input field E and input stress σ and the output polarization P and output strain ε as shown in Figure 2.11 and 2.12. Hysteresis and nonlinearities are present to some degree in all ferroelectric outputs at all input drive levels and is also a function of temperature and pressure [27, 38].

In Figure 2.11, the hysteresis relations for field-polarization and field-strain are shown for a typical soft single crystal ferroelectric compound, lead lanthanum zirconate titanate

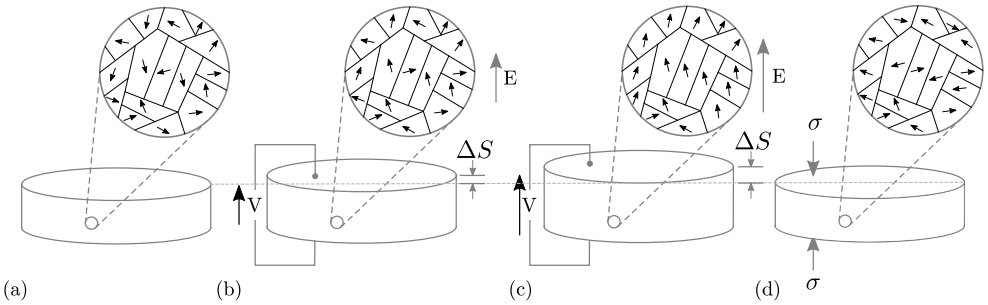

Figure 2.10: (a) Unpoled polycrystalline ferroelectric materials, (b) changes in 180° domains, (c) in 90 ° domains as a result of poling and (d) ferroelastic switching due to applied stress greater than coercive stress [18, 37].

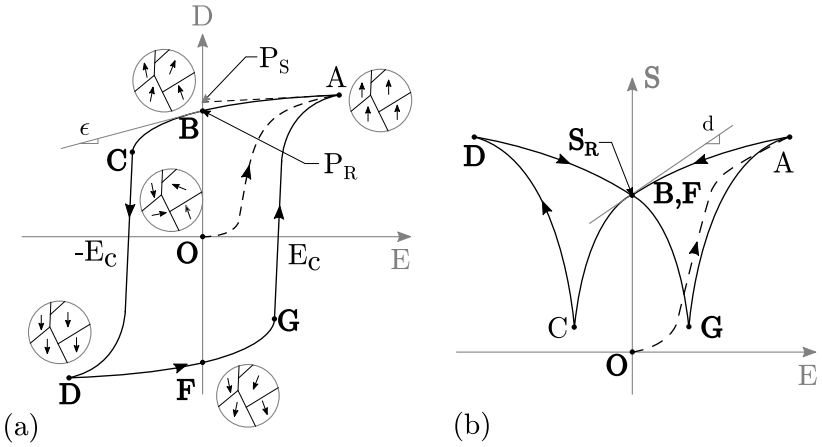

Figure 2.11: (a) Hysteresis field-polarization relation and the linear approximation at point B, where there is remanent polarization and (b) hysteresis field-strain relation and linear approximation at point B and F, where there is remanent strain [18, 12].

(PLZT). Soft ferroelectric compounds have higher domain wall mobility than hard ferroelectric compounds and are referred to as "ferroelectrically soft". The usage of this provides an example of typical soft ferroelectric and ferroelastic properties that are common to soft ferroelectric compounds.

At first, the bulk PLZT is apolar and has random domain alignment, as Shown in Figure 2.11 point O. As the material is subjected to a high electric field, line segment OA, the domains go from random to aligned to the field and the polarization is saturated P_S. If the field is increased further, there is approximately linear increase due to reversible displacement of the ions. From line segment AB, there is a removal of the applied field, which results in positive remanent polarization P_R, remanent strain S_R and the material is now poled. One thing to note is that if the material was purely dielectric it would follow a straight line from A to above B (dashed line) which is not the case. If small fields were applied at point B, it would be possible to approximate the output polarization and strain as reversible and linear, which is what linear constitutive equations estimate. As the negative field is increase from line segment C to D, the negative coercive field $-E_c$ is passed and the polarization begins to switch. In the field-polarization chart, the region is

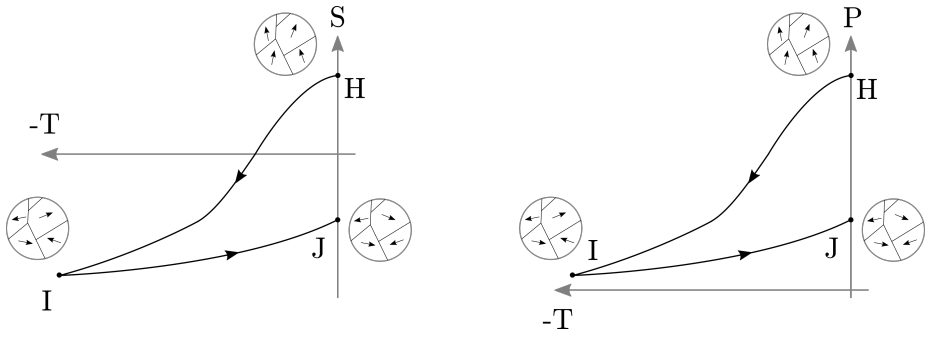

Figure 2.12: Hysteresis shown in (a) stress-strain relation and (b) stress-polarization relation due to 90° switching caused by compressive stress [18].

called the "burst region" which is the result of 180° domain switching. In the field-strain chart, this burst region does not affect strain. At point D, the dipoles have aligned or are in near alignment to the field. The polarization is opposite of point A, but the strain is equal to A as the lattice strain is in the same sense whether the polarization is negative or positive. From segment D to E and G to A, the effect is similar but opposite polarization to line segment A to B and C to D.

Ferroelastic switching caused by compressive stress is shown in Figure 2.12. Point H indicates the positive remanent polarization when no applied field or stress is present. As the compressive stress is increased from point H to I, the increasing compressive stress causes 90° domain switching and results in negative strain and polarization reduces. Once point I is reached, the switching is almost complete and the Young's modulus is linear. As the compressive stress is reduced from point I to J, the polarization and strain are nearly linear as the primary component of strain is elastic strain.

As shown, hysteresis is present in ferroelectric materials due to ferroelectric and ferroelastic switching, which is a function of the available pinning centers that is dependent upon the crystal structures present. As most ferroelectric alloys are near to the morphotropic phase boundary, hysteresis is a complex function of both the tetragonal and rhombohedral minimum energy sites. Furthermore, the "burst region" for polycrystalline is closer to that shown in Figure 2.9 than in Figure 2.11 due to the effect of random orientation of domain and grains and stress present at the grain boundaries. Even single crystals do not have a sharp transition as the domain wall movement is hindered by inclusions and pinning sites in the material.

2.2.7 Relaxor Ferroelectrics

Relaxor ferroelectrics, or relaxors, can be differentiated from ferroelectrics ceramics by a frequency dependence of dielectric permittivity peak, temperature dependent hysteresis, and lack a phase transition to describe those two phenomena. While relaxors are named ferroelectrics, the fundamental phenomenon is different. The following discussion will focus on widely researched relaxor, lead magnesium niobate (PMN) [39].

The dielectric permittivity of conventional ferroelectrics have peaks near structural phase transitions (e.g. from cubic to tetragonal). These peaks are explained by the dynamic instability that exists as the material is shifting between two structures [39]. Yet the cause for relaxors permittivity peak, see Figure 2.13 (a), is not from a structural phase transition. The dielectric permittivity peak is a function of frequency and temperature, which indicates a different mechanism [40].

Secondly, relaxor ferroelectrics exhibit a temperature dependent hysteresis, see Figure 2.13 (b). At low temperatures, relaxor ferroelectrics have a similar ferroelectric hysteresis shape. Yet, as the temperature increases the hysteresis slowly shifts to nonlinearity. Further proof of a different mechanism than phase change can be seen by the slow reduction of the remanent polarization as the temperature increases, which is unlike the polarization loss that occurs in ferroelectrics during phase transition.

Further proof of the lack of a structural change is seen in the lack of optical anisotropy, or x-ray line splitting, as the PMN is cooled and shows these phenomena, see Figure 2.13 (c). The lack of optical anisotropy and x-ray line shifting indicates that this material does not exhibit a phase change while the strain response becomes ferroelectric and permittivity peaks.

The relaxor phenomena was described through the concept of polar nano-regions (PNR) and later experimentally proven through electro-optical methods [40]. The PNR begin to form at 620 K, which is called the Burns temperature [39]. These regions start at 2–3 nm near the Burns Temperature and grow to ≈10nm at 160 K, which roughly constitutes 30% volume fraction at the low temperature [15]. These PNRs are believed to be dynamic and contribute significantly to the polarizability of the system [15]. Therefore, the PNRs dynamics, which is disordered, impact the dielectric permittivity relaxation that occurs at the dielectric maximum temperature and is spread across a range of 200 K [40].

These PNRs are also used to describe the low-temperature ferroelectric hysteresis. These PNR are frozen into spin-glass-like state when the temperature is cooled [41]. Although these polar regions are dominantly polarized in the $\langle 111 \rangle$ orientation, they are randomly arranged and exhibit zero macroscopic anisotropy [15]. When a high electric field is applied, these PNRs can be oriented to form macro-domains and a similar hysteresis shape is exhibited.

A common polycrystalline relaxor is lead magnesium niobate with lead titanate (PMN-PT) that has favorable properties compared to normal ferroelectrics. Due to the lack of macroscopic domains, the material exhibits no aging, see Figure 2.14. Furthermore, the macroscopic electric field response is quadratic and described as electrostrictive, see Figure 2.15 (a). The microscopic electric field response of the PNR can be seen in Figure 2.15 (b). Relaxors are used in high precision activities due to the lack of hysteresis, customizable dielectric peak temperature and absence of aging. For these reasons, PMN-PT has been used in the Hubble telescope and finds applications in deformable mirror and other high precision items [42].

Although PMN-PT properties are excellent, there has been implementation issues. PMN-PT has a low curie temperature T_C and a low rhombohedral-to-tetragonal phase

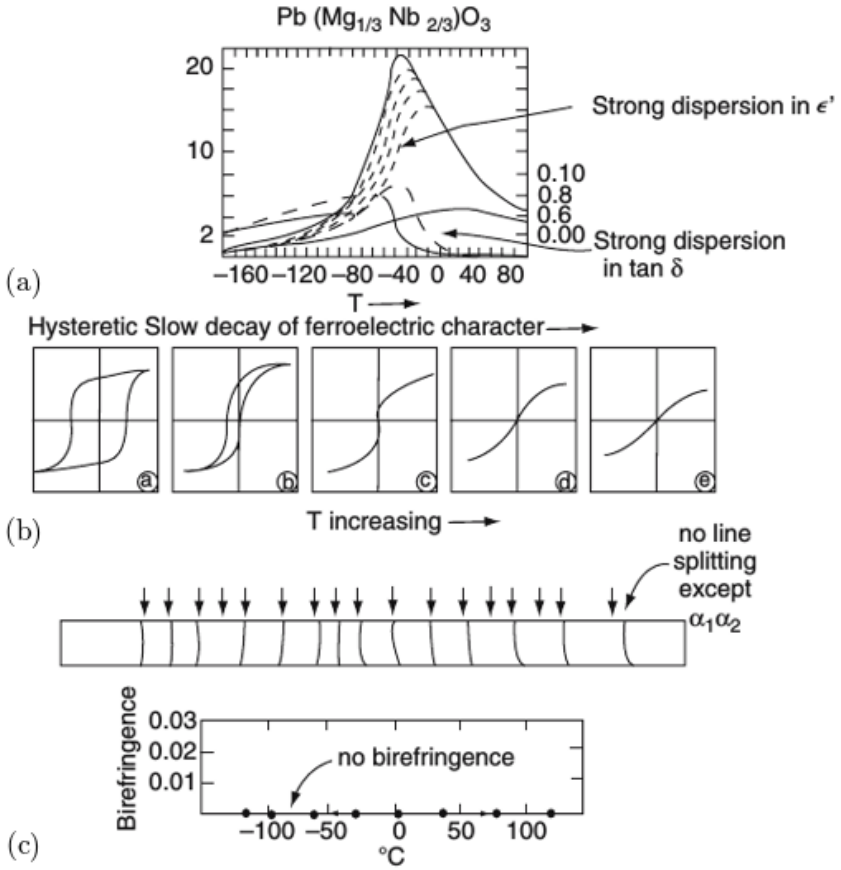

Figure 2.13: Characteristic features of PMN. (a) Dielectric dispersion as a function of temperature and frequency, (b) hysteresis as a function of temperature and (c) Optical and x-ray evidence of absence of macroscopic phase change around the dielectric maximum temperature (Reprinted by permission from Springer Customer Service Center GmbH: [40]).

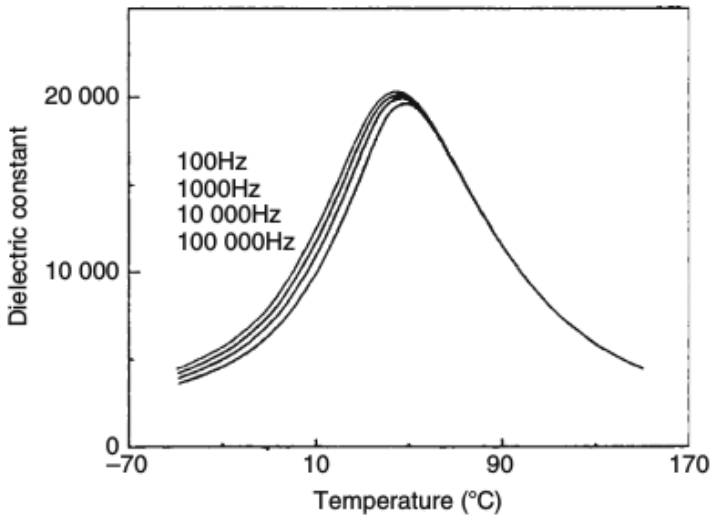

Figure 2.14: Absence of aging in 0.9 PMN:0.1 PT over a range of temperatures and at different frequencies after 1,000 h of aging at 20°C (Reprinted by permission from Springer Customer Service Center GmbH: [40]).

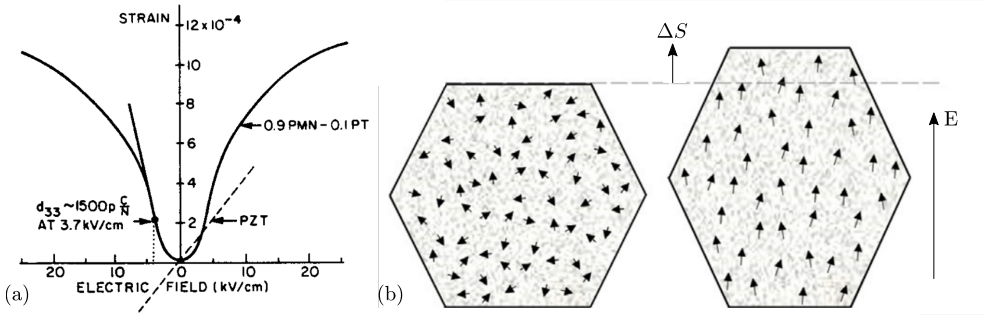

Figure 2.15: (a) Electrostrictive strain as a function of applied electric field in 0.9 PMN:0.1 PT, where the solid line represents the d_{33} slope and the dotted line shows the d_{33} slope for a PZT , (b) illustration of the relaxor polar nano region ((a) Reprinted from [43] with permission from SAGE and (b) adapted from [37], with permission from Elsevier).

Table 2.2: Properties of various generations of relaxor-PT single crystals [22].

Crystal	T_C(°C)	T_{RT}(°C)	E_C(kV/cm)	ϵ_r^*/ϵ_0	d_{33} (pC/N)	k_{33}	Q_m
First generation crystals							
PMN-0.29PT	135	96	2.3	5400	1540	0.91	150
PMN-0.33PT	155	65	2.8	8200	2800	0.95	100
Second generation crystals							
PIN-PMN-PT	191	125	5.0	4400	1510	0.92	180
PIN-PMN-PT (MPB)	197	96	5.5	7240	2740	0.95	120
PMN-PZT	210	113	5.0	5000	1750	0.92	150
PMN-PZT	216	144	4.6	4850	1530	0.93	100
BSPT57	402	349	13.7	3000	1150	0.91	—
PYN-0.45PT	325	160	12.5	2000	2000**	0.90	—
Third generation crystals							
Mn:PIN-PMN-PT	193	199	6.0	3700	1120	0.90	810
Mn:PMN-PZT	203	141	6.3	3410	1140	0.92	1050

* - real dielectric permittivity where $\epsilon_r' = \epsilon_r \cdot \tan\delta$ where ϵ_r' is imaginary permittivity [22]

** - calculated from the slope of S-E loop at 20 kV/cm

transition temperature T_{RT} that limits its temperature range. Alongside the low temperature range, PMN-PT has a low coercive field E_C, which introduces polarization stability issues [22]. To mitigate the polarization stability, a dc bias field needs to be applied but a dc bias reduces sensitivity which increases electronic complexity [22]. Lastly, PMN-PT have low mechanical quality factors (≈100) which limits their resonance applications. Due to these reasons, other relaxor materials have been studied.

The concept of different generations of relaxor crystals introduced by Smith is used to describe the field of relaxor ferroelectrics [22]. The first generation crystals, PMN-PT and PZN-PT, have high electromechanical coupling and piezoelectric coefficients that allow for significant improvements in comparison to PZT systems. The second generation crystals extended the temperature range and applied electrical field and mechanical stress [22]. The third generation of crystals have minor addition of dopants, similar to the modifications of PZT, allowing for tailoring of the properties of the material. In Table 2.2, the generations of relaxor crystals are shown.

For those who are interested in understanding relaxor ferroelectrics better, it is suggested to read the review by Zhang and Li [22].

2.2.8 Piezoelectric Polymers

Piezoelectricity exists in three different types of polymer categories, as shown in Figure 2.16. Bulk piezopolymers are polymer films that have piezoelectricity because of the molecular arrangement and structure of the monomers. Piezoelectric polymer composites are composite that consist of polymer structures and piezoelectric ceramics, which uses the beneficial mechanical compliance of the polymer structures alongside the greater electromechanical coupling of the piezoelectric ceramics. Lastly, ferroelectrets are a polymer film that has gas voids introduced and charged to form internal dipoles. These materials each serve a different objective and have different properties and will be briefly discussed.

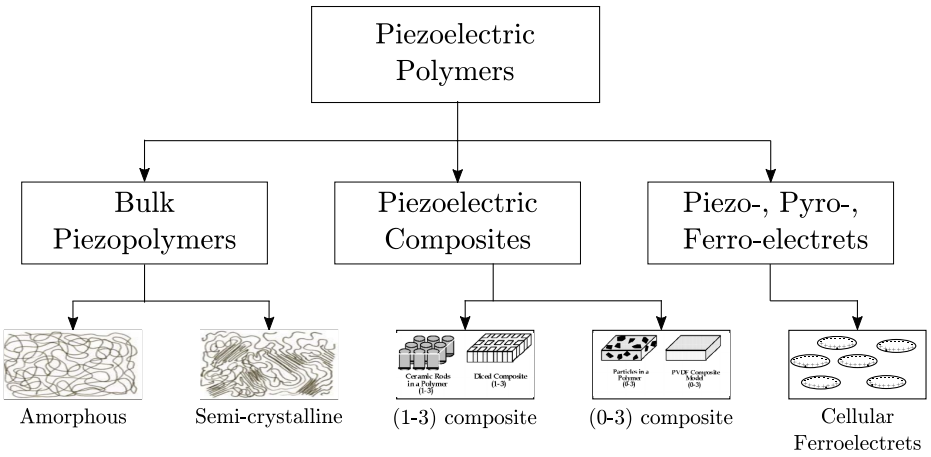

Figure 2.16: Schematic of different piezoelectric polymer categories: bulk piezopolymers, piezoelectric polymer composites and piezo-, pyro- and ferro-electrets (images from [44], and adapted from [45] ©2005 IEEE).

2.2.8.1 Bulk Piezopolymers

The molecular structure of the polymer and its orientation provides the piezoelectric response in bulk piezopolymers. There two type of piezopolymers: semi-crystalline and amorphous. For the sake of brevity, only the commercially available and popular semi-crystalline piezopolymer PVDF will be reviewed. For further information about piezopolymers, read the piezopolymers review by Ramadan et al. [46].

PVDF, PVDF Copolymers and PVDF Terpolymers: polyvinylidene flouride (or PVDF) is the most popular piezopolymer used in transducer devices [46]. PVDF are flexible, mechanically stable and easier to manufacture than piezoelectric ceramics but have lower piezoelectric coefficients [47]. Due to their low piezoelectric coefficents, PVDFs are not used as actuators but are used as sensors, energy harvesters and dielectrics [48]. For a further phenomenological review of PVDF, one should read the seminal review by Lovinger [49] and the more recent review by Qi Li and Qing Wang [50].

PVDF is a thermoplastic semi-crystalline ferroelectric polymer which has ferroelectric properties due to its molecular structure and variety of crystalline forms [51]. The PVDF molecular structure is created by the polymerization of $CH_2 = CF_2$ monomers [46]. Due to the large van der Walls radius of fluorine atoms (1.35 $\AA$ versus 1.2 $\AA$ for hydrogen) and electronegativity of the polymer chain [–CH_2–CF_2–], a dipole moment is formed perpendicular to the chain of each monomer unit [49, 51] and is the elementary unit in PVDF [50]. This elementary unit resides in the crystalline portion of PVDF, which is approximately 50%–60% crystalline [52, 50]. PVDF has four major crystalline phases that relate to the molecular chain conformations (or coiled shapes), see Figure 2.17 [50]. α and δ phase are TG^+TG^- and γ is $TTTG^+TTTG^-$ where T means trans- and $G^{\pm}$ means gauche-torsional arrangements [49]. The β phase consists of chains of all-trans form, which has the largest spontaneous polarization out of the phases [52], and is desirable [52, 51].

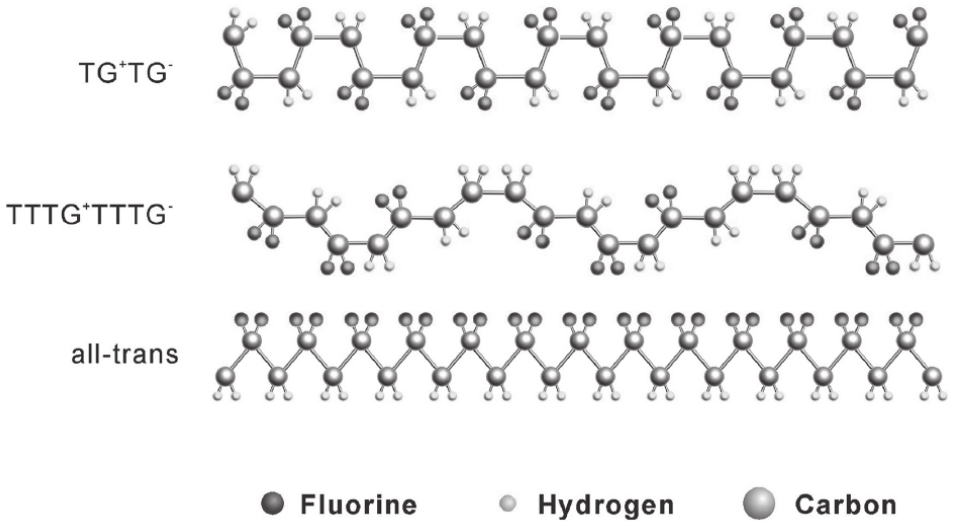

Figure 2.17: Illustration of different chain conformations where T means trans and G means gauche torsional arrangements with substituents taking 180° and ±60° to each other respectively (Reprinted from [50] with permission from John Wiley and Sons).

To create β phase in PVDF, it is necessary to go through post-processing. Stretching the energetically favorable non-polar α or the polar γ phase PVDFs at an elevated temperature can result in extending the conformation and result in *beta* phase present [53, 50]. Poling α phase at ≈500 kV/mm can also induce β transformation [49]. Without electrode poling or corona poling, the PVDF domains will remain random and very little output will be exhibited.

Copolymerization is a defect engineering process that results in the tuning of the material structure by addition of certain comonomers [51]. The comonomer type and composition ratio affects the crystalline structure and intermolecular interaction [50]. A variety of vinylidene flouride (VDF)-copolymers and terpolymers have been introduced, such as trifluoroethylene (TrFE), chlorotrifluoroethylene (CTFE), or hexafluoropropylene (HFP) [51].

The defect engineering process can be understood through the defect-modified P(VDF-TrFE). The defect TrFE is relatively bulky comonomer in comparison to VDF and results in a larger interchain distance [50]. This interchain distance allows for the material to naturally form the β phase at the detriment of the curie temperature [50]. P(VDF-TrFE) copolymers exhibit lower ferroelectric–paraelectric transitions, high strain and dimensional changes (≈10%) but have large hysteresis [54].

It is known, from the study of relaxor ferroelectrics, that the reduction of coherent polarization regions to nanoregions can reduce the energy barrier required between polarization switching [54]. In P(VDF-TrFE) copolymers, the reduction of polarization regions can occur through high-energy radiation that causes defect introduction into the polymer chain. Irradiation can induce a relaxor ferroelectric properties as shown in Figure 2.18. Due to this relaxor ferroelectric properties, irradiated P(VDF-TrFE) is sometimes referred to as electrostrictive, due to electrostrictive relationship between strain and polarization

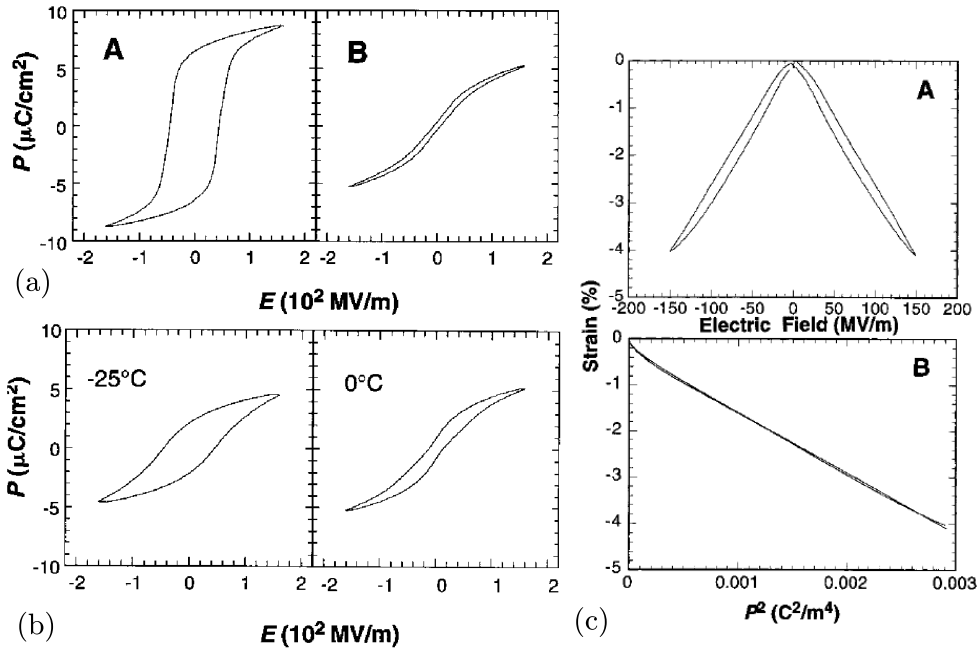

Figure 2.18: (a) Polarization hysteresis loops of P(VDF-TrFE) 50/50 copolymer at room temperature (left) before and (right) after irradiation, (b) Polarization hysteresis loops measured at two temperature showing the increased remanent polarization and hysteresis at low temperatures and (c) (top) Strain-field dependence of irradiated P(VDF-TrFE) 50/50 copolymer and (bottom) electrostrictive relation between strain and polarization, where P≥0 strains overlap P≤0 strains (From [54]. Reprinted with permission from AAAS).

($\varepsilon = Q^2$). The issue with irradiating P(VDF-TrFE) is that it is an energy intensive process and not suited for large scale production [50].

The relaxor ferroelectric behavior is also possible by addition of a ternary monomer. Small additions of a ternary monomers, or defects, with a bulky group, chlorotrifluoroethylene (CTFE) and chlorofluroethylene (CFE), allow for relaxor ferroelectric behavior under the right conditions [48]. These defects must be included in the crystal phase and increase the interchain spacing and reduce the energetic barrier for dipole orientation [55]. This is performed by the introduction of the TrFE defect, which allows for a larger expansion through a terpolymer [17]. The second requirement for relaxor ferroelectric behavior is the reduction of the ferroelectric domain size to nano-scale so that the cooperative polarization is smaller than that found in P(VDF-TrFE) copolymers, which is performed by the addition of the terpolymer [17].

PVDF terpolymers are still being actively investigated and do not have a significant quantity of material properties. Therefore, only certain PVDF polymers are demonstrated in Table 2.3. Similarly, most copolymers manufacturers do not indicate a significant amount of material properties.

Table 2.3: Material property overview of PVDF and PVDF copolymers

Material	T_C (°C)	k_{33} —	$\epsilon_{33}^T/\epsilon_0$ —	d_{33} (pC/N)	s_{33}^E ($10^{-12}m^2/N$)	E_c (kV/mm)	Q_m —	tan δ —	Ref.
PVDF	90	0.27	12	-(13–28)	—	50–120	—	0.018	[46]
P(VDF-TrFE)	100	0.37	12	-(24–38)	—	50–120	—	0.018	[46]
PVDF	—	0.19	7.6	-32.5	472	50–120	13	0.256	[8, 56, 57, 58]
P(VDF-25%TrFE)	119.8	0.116	7.9	-33.5	300	50–120	19.6	0.106	[59, 8, 56, 60]

2.2.8.2 Piezoelectric Polymer Composites

A piezoelectric polymer composite, or piezocomposite, is piezoelectric ceramic that is embedded in a polymer. For this review, the polymer material will be assumed to be have no electromechanical transduction, or non-piezoelectric. The benefit of piezocomposites is that it can be tailored to the application. They combine the high electromechanical coupling and dielectric strength of the piezoelectric ceramic with the high compliance of the polymer. For this reason, piezocomposites are used for acoustic devices due to their ability to match impedance and fewer spurious modes [46].

The piezocomposite properties are a function of how they are connected. The main different connectivities that are available are shown in Figure 2.19. The first number in composite parenthesis indicates number of dimensions of connectivity of the piezoelectric active stage and the second digit is number of dimensions of connectivity of the electromechanically inactive stage [45]. Only the two main connectivities will be reviewed, which is the (1-3) composite, which has arranged or randomly scattered rods in a polymer bulk, and the (0-3) composite which has piezoelectric particles, which are completely separated, embedded in a polymer matrix. For a further description of different compositions, one should read the seminal work by Newnham et al. [61] or for a more contemporary work of Akdogan et al. [45].

Composite material properties are not specified as it depends upon the piezoelectric to polymer ratio, which is application specific. Piezocomposites though are much more capable of achieving excellent results than single bulk piezoelectric material. For example, all piezocomposites achieve much higher $d_h g_h$ coefficient than single-phase piezoelectrics, see Figure 2.20 [45].

(1-3) Piezocomposites: the (1-3) connectivity is the most widely used piezocomposite [62]. The connectivity uses the higher piezoelectric coupling coefficients of the material. The piezoelectric material is generally PZT or the PMN-PT, with the latter having a coupling coefficient of roughly 0.7–0.9 [63, 64, 65].

The (1-3) composite can be constructed in many different methods. Some common manufacturing methods are laminate-and-cut, arrange-and-fill and dice-and-fill [46]. The term pitch for this composite is defined as the sum of the rod width and the spacing between rods [46]. Pitch size affects the upper frequency limit and the coupling coefficient [46].

Two additional commercial piezocomposites are called the Active Fiber Composite (AFC) designed by MIT [66] and Macro Fiber Composite (MFC) created by NASA Lan-

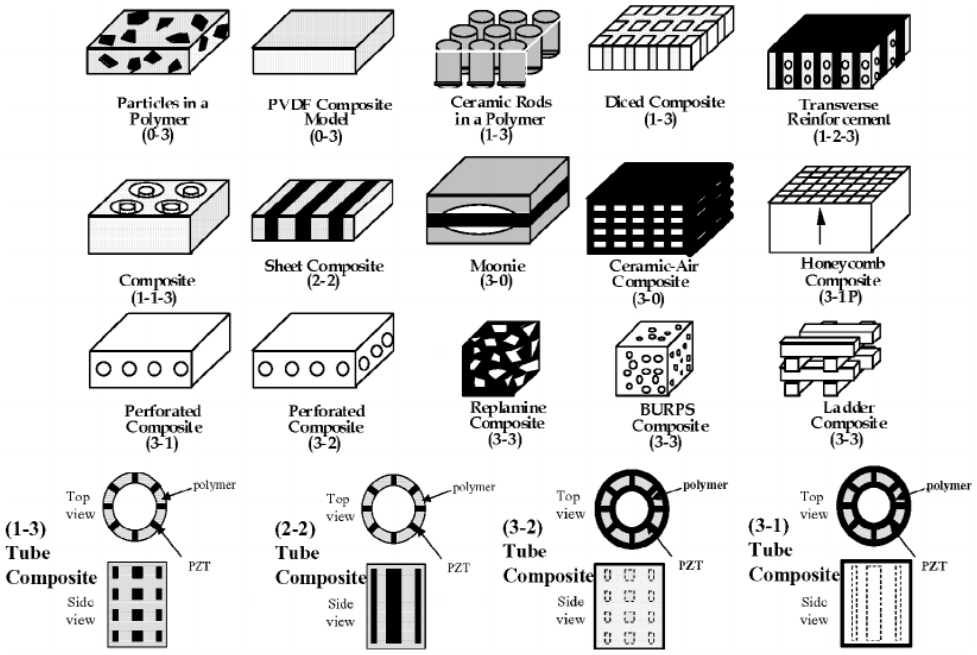

Figure 2.19: Overview of piezocomposite connectivities ([45] ©2005 IEEE).

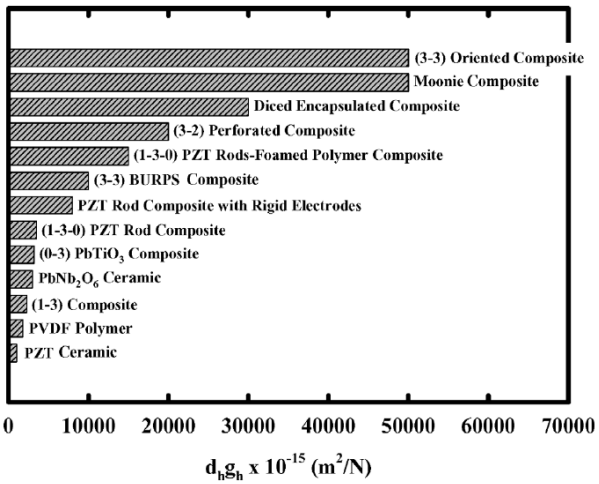

Figure 2.20: Comparison of figure of merit ($d_h g_h$) of various piezoelectric composites ([45] ©2005 IEEE).

gley [67]. These composites are lighter weight, higher strain density than conventional piezoelectrics and piezocomposites [62]. They are constructed with uniaxially aligned piezoelectric fibers with a polymer matrix. The only difference between them and (1–3) piezocomposites is that MFC and AFC contain interdigitated electrodes [62]. These composites are used in micro- to macro-scale structural vibration [68] and energy harvesting applications [69]. An overview of the composite actuators and their benefits has been written by Williams et al. [70].

(0-3) Piezocomposites: the (0-3) connectivity has the lowest manufacturing cost of the piezocomposites [71]. It is easy to manufacture and integrate into structural systems [72] and MEMS [73], but it is also more difficult to model [46]. The (0-3) connectivity composites can be used as a smart structure [71], a sensor [74] and an array of different microelectronics (e.g. embedded capacitors, inductors, antennas, electromagnetic shielding) [73].

The manufacturing process consists of putting piezoelectric ceramics into a matrix and curing. The common matrix is either a concrete for civil structures or polymers for MEMS and other transducers. Common polymers used in (0-3) connectivity is SU-8, PVDF and PDMS [46, 72]. The piezoelectric ceramic depends upon the application. PZT is the quite popular alongside PMN-PT, but for civil applications a lead-free piezoelectric, such as $BaTiO_3$, is important due to lead toxicity [75].

2.2.8.3 Piezo-, Pyro- and Ferro-electrets

The term electret originally meant a dielectric that has quasi-permanent dipole orientation [76]. The quasi-permanent term indicates that the decay time of the charge is larger than the experimental observation time the material [77]. Nowadays, the term is also used for cellular polymers that exhibit piezo-, pyro- and ferroelectric properties. Other names and categories that these materials fall under are space charged electrets [78], dielectric elastomers [79], electroactive polymers [77], voided charged polymers [46] and polymer electrets [77]. Piezo-, pyro- and ferro-electrets have received extensive interest as ultrasonic probes, microphones and more recently as energy harvesters [77].

Cellular polypropylene (PP) is the most common ferroelectret due to its ease of processing and high piezoelectric constant [77]. The phenomenon of piezoelectricity for this voided electret can be described through Figure 2.21. In this case, the polymer is part of a subset called void formation and expansion based voided polymers [80]. First, the voids are formed by introducing some micro-scale particles into the PP, and then stretching to cause voids to precipitate at the particles. Next, the PP void size is adjusted through cycles of pressure and heat. Finally, the material is subject to fields exceeding 100 MV/m, which causes a dielectric barrier discharge in the void. After these processes, the material exhibits piezo-, pyro-, and ferro-electricity, which all have been experimentally validated [76].

Cellular PP has notable characteristics. Due to the cavities, it is extremely soft in the thickness direction (≈1 MPa) while being stiffer in the longitudinal direction (≈1 GPa) [77].

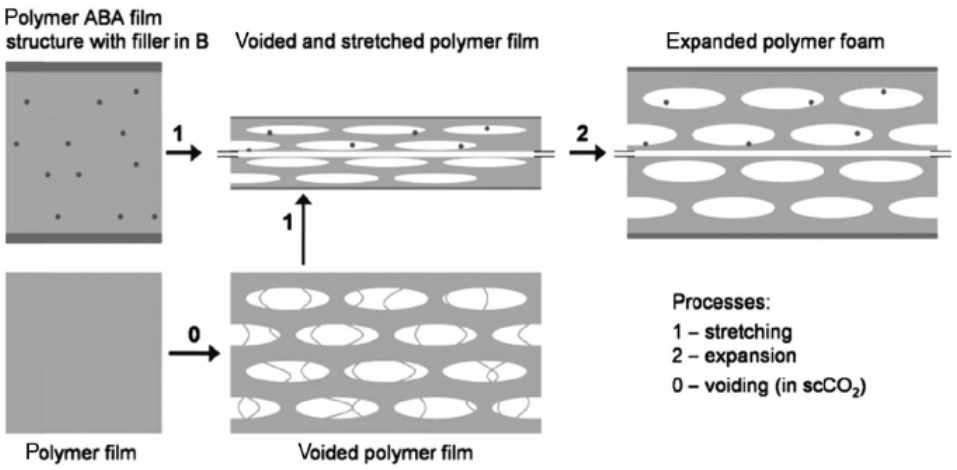

Figure 2.21: Manufacturing process for voided polymers by (top) stretching or (bottom) direct film foaming (Reprinted from [80] with John Wiley and Sons).

Table 2.4: An overview of piezo- and ferro-electret films

	T_{max} ($^{\circ}C$)	d_{33} pC/N	d_{31} pC/N	c_{33} ($10^6 N/m^2$)	ϵ/ϵ_0 —	Ref
Emfit 70 μm	50	170	1.1	<1	1.2	[83]
Emfit*	70	250-400	—	1	1.1± 10%	[81]

* - manufacture indicated Emfit specifications for 70 μ m

From this structure, the material exhibits high d_{33} piezoelectric strain coefficient (250–400 pC/N [81]) and low transverse d_{31} and d_{32} piezoelectric strain coefficient (≈2 pC/N) [77]. Yet, cellular PP has low temperature stability of the d_{33} coefficient. At temperature above $70^{\circ}C$, cellular PP d_{33} decreases from values of 1000 pC/N to 100 pC/N [82]. Although some material properties are available, ferroelectrets are fairly new and actively researched and the few properties have considerable variability from the same supplier, as shown in Table 2.4.

Due to the temperature limitation, other ferroelectrets have been pursued. These efforts have resulted in transducers that have higher operating temperatures but reduced piezoelectric response. The most promising material is the voided fluropolymers [78, 22]. For interested readers, it is suggested to read the seminal review by Gerhard-Multhaupt [76] and a newer review by Mohebbi et al. [80].

2.3 Application Considerations

Piezoelectric ceramics are normally packaged to ensure optimal operation life and tailored to application specifications. The following section will overview some of the more common design features and issues that occur with piezoelectric operation.

In actuators, piezoelectric ceramics are generally produced in thick sheets (≤1 mm)

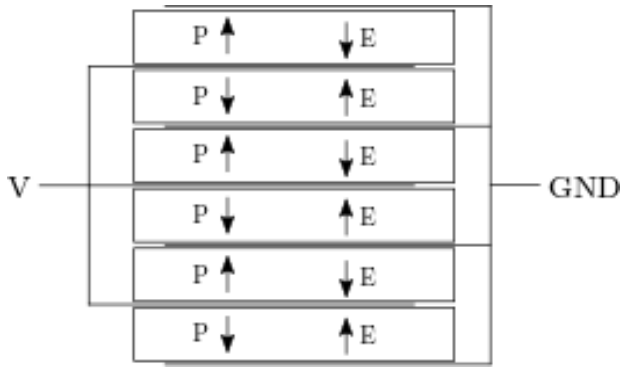

Figure 2.22: (a) Effect of longitudinal expansion on volume of actuator and (b) electrode configuration of longitudinal piezoelectric stack [84].

to reduce excessively high voltages and preloaded to reduce effects of inertial cracking. Resonant actuators and energy harvesters need to consider materials based on the coupling coefficient and losses. Most piezoelectric material devices need to be concerned with temperature-dependent behavior. These properties are important for optimal use and selection within the piezoelectric family. The following discussion will focus on the application of piezoelectric ceramics.

2.3.1 Stacking

PZT actuators generally operate at high electric fields (2 kV/mm). If the piezoelectric disc is thick ($\geq$ 1mm), then high voltage (2000 V) is required to get high electric fields. To avoid this issue piezoelectric actuators are designed to be multilayer. Multilayer, or stack, piezoelectric actuators consist of thin layers (100 μm) of piezoelectric ceramic bonded between electrodes stacked in series so that polarization axis is aligned with the displacement or force axis. The electrodes of a stack are connected in parallel as shown in Figure 2.22 (b). A stack is able to achieve larger displacement than a single chip while keeping response times of less than a millisecond and low drive voltages (from 100 V for high reliability to 1000 V for high force) [84]. Stacking has the disadvantage that it is more demanding production and design process and humidity-driven cracking within the piezoelectric can occur if the stack is not coated in ceramic [84].

2.3.2 Preload

Piezoelectric ceramics have characteristically low tensile strength, 5 to 10 MPa [84]. If the ceramic is dynamically operated, the inertial loads may exceed the tensile strength of the ceramic. To mitigate these effects a mechanical preload is needed. The mechanical preload should be set to ensure sufficient protections against any inertial loads.

As shown in Figure 2.23, the idealized force-stroke curve of piezoelectrics indicates the boundaries of operation available. The largest displacement, Δx_{max}, occurs when the

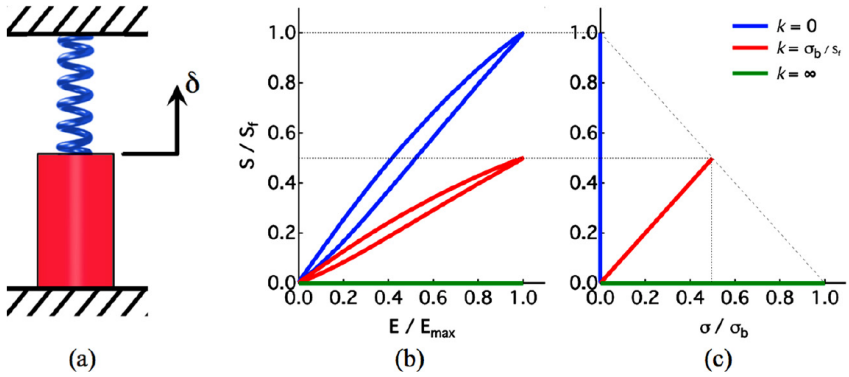

Figure 2.23: Stroke-force relation of a preloaded piezoelectric actuator (Reprinted from [85], with the permission of AIP Publishing.).

actuator is unloaded. The largest force F_{block} occurs when the actuator is fully constrained from expanding. When the piezoelectric is attached to a spring preload, the achievable stroke is less than the maximum displacement and the blocked force.

In reality, the balance between electric field and mechanical preload is more complex than this. It was shown that mechanical depolarization, a decrease in remanent polarization caused by ferroelastic switching, can occur in soft lanthanum doped PZT (PLZT) at stresses of 5 MPa [23]. For piezoelectric operated at high driving levels (2 kV/mm), a moderate preload (≈40 MPa) for PZT stack actuators can increase the unipolar strain output by a notable amount (≈16–20% difference) and a work density increase of 28 % [86]. The exact reason is that the preloading causes increase in in-plane domains through ferroelastic switching. These in-plane domains have weak enough mechanical fields that a strong electric field can cause the ferroelastic switched domains to be ferroelectrically switched, but due to this switching there will be more hysteresis as shown in Figure 2.24. If the spring is too strong, then the mechanical energy field is too strong for electrical energy to induce switching [87].

2.3.3 Creep and Aging

Piezoelectric materials exhibit a low-frequency drift which is called creep. Creep normally indicates a rate-dependent deformation at a constant load or stress. In this case, creep indicates a rate-dependent deformation due to an applied electric field. Creep, like hysteresis, is a result of slow domain realignment to the applied field, see Figure 2.25. Due to creep, any precision positioning requires feedback or feed-forward control. As seen in Figure 2.25, a position of 25 μm will creep to 33.4 μm in 15 minutes. This results in a limitation to the quasi-static uses of ferroelectrics.

Aging is different than creep as it occurs with no applied field and over a greater amount of time. Aging occurs as the material relieves stress in the domain through ferroelastic domain polarization rotation. The gradual relief results in a decrease in piezoelectric

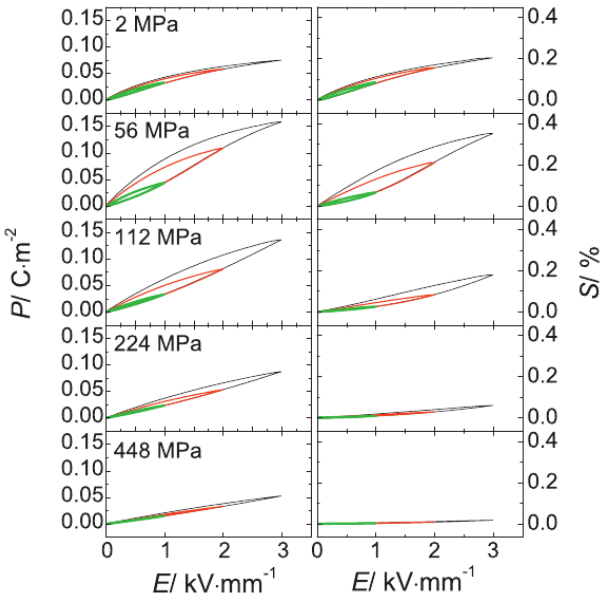

Figure 2.24: Polarization-Field P(E) and Strain-Field S(E) at room-temperature under different electric field amplitudes 1 kV mm^{-}1, 2 kV mm^{-}1 and 3 kV mm^{-}1 (Reprinted from [87], with permission from Elsevier).

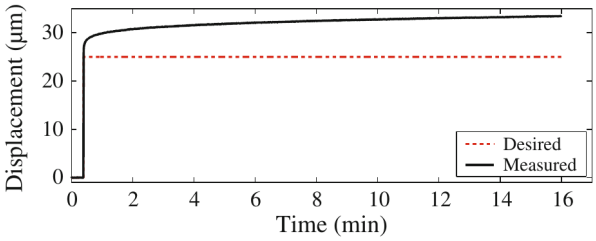

Figure 2.25: Output displacement creep with an applied step input (Reprinted by permission from Springer Customer Service Center GmbH: [88]).

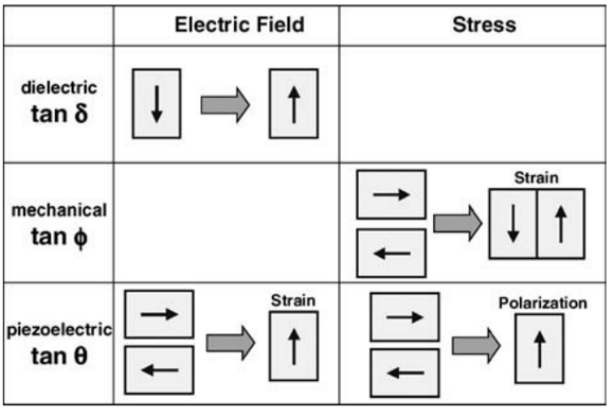

Figure 2.26: Polarization reversal/reorientation model for explaining dielectric, mechanical and piezoelectric losses (Reprinted by permission from Springer Customer Service Center GmbH: [91]).

coefficients and dielectric loss while mechanical quality factor increases [89]. Generally, accelerated aging treatments are performed to ensure that the material is stable.

2.3.4 Dielectric Loss Coefficient and Mechanical Quality Factor

Hysteresis in piezoelectric is also defined as loss. Loss can occur from four different phenomena: domain wall motion, fundamental lattice portion (occurs in single crystals), microstructure portion (occurs in polycrystalline materials), and conductivity part in high ohmic materials [90]. But for the cases of ferroelectrics, the domain wall motion contribution to loss exceeds the other three contributions [91].

The consideration of energy loss is important for piezoelectric systems. For positioning actuators, hysteresis increases the implementation difficulty and limits the resolution. For resonant actuators, or ultrasonic motors, losses result in heat buildup in the material which degrades performance [34]. As well, strain amplification at resonance is related to the mechanical quality factor Q_m (inverse of mechanical loss) where lower mechanical losses results in more strain amplification [91]. For force sensors and acoustic transducers, a low mechanical quality factor results in a higher frequency range [90].

2.3.5 Small- and Large-Signal Piezoelectric Coupling Coefficient

The piezoelectric coupling coefficient is affected by the size of the input signal. The piezoelectric coupling coefficient d_{ij} is called the small-signal piezoelectric coupling coefficient, which is shown by the dashed line in Figure 2.27. At large applied mechanical and electric fields, the domain wall motion and polarization switching become more predominant and causes the piezoelectric coupling coefficient to nonlinearly vary. The large-signal piezoelectric coupling coefficient d^*_{ij} is useful in indicating the performance of piezoelectric during

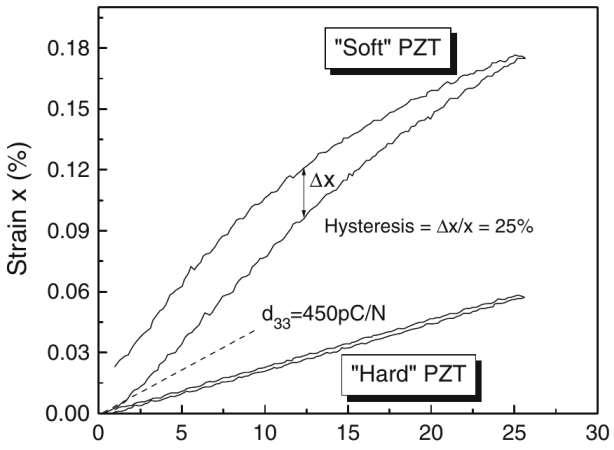

Figure 2.27: Strain-field relation for soft and hard PZT showing large-signal hysteresis (Reprinted by permission from Springer Customer Service Centre GmbH: [27]).

actuation. The large-signal piezoelectric coupling coefficient is roughly double the small-signal coupling coefficient, and is more notable in soft piezoelectrics [38].

The large-signal piezoelectric coefficient is calculated with unipolar electric field and as follows:

$$d^*_{ij} = \frac{S_{max}}{E_{max}} \tag{2.2}$$

2.3.6 Temperature-Dependent Behavior

Piezoelectric properties vary significantly with temperature, which is a problem not only for actuators but sensors. For ferroelectrics, the cause is a function of both its curie temperature and its morphotropic phase boundary.

Ferroelectrics generally exhibit their highest properties when they are nearest to their curie temperature but their properties become more temperature dependent and have reduced polarization stability (caused by aging and increased thermal depoling) [27]. A general rule is that ferroelectrics should be operated at half their curie temperature without significant reduction in piezoelectric activity [27, 12]. When heat buildup occurs below curie temperature, ferroelectrics issues start with increased domain activity (nonlinearity and aging) and shifting piezoelectric coefficients but can result in thermally induced phase transitions that causes thermal depoling and possible loss of preload contact [27, 92].

The orientation of morphotropic phase boundary is the cause of the shifting piezoelectric coefficients and the thermally induced phase transitions. As shown in Figure 2.28, if the boundary is vertical then temperature changes keep the material near its instability condition (between two phases). If the boundary is curved, then the piezoelectric properties will increase nearer to the boundary and decrease further from the boundary. If the morphotropic phase boundary is crossed, then thermally induced phase transition occurs

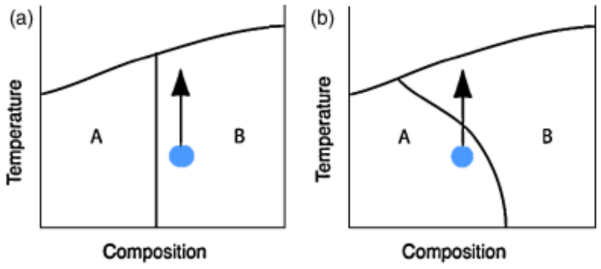

Figure 2.28: A vertical (a) and curved (b) morphotropic phase boundary (Reprinted from [93] with permission from John Wiley and Sons).

causing changes to the domain wall structure and thermal depoling [93]. For those materials that have a curved morphotropic phase boundary, curie temperature is not a good figure of merit. Instead the phase transition or depolarization temperature T_d is used. For the selection between piezoelectric materials, an important factor is the maximum temperature possible and that is quantified as the curie temperature or the depolarization temperature [93]. For a more extensive discussion regarding piezoelectric composition, morphotropic phase boundaries, and thermally induced phase transition, read Shrout and Zhang and Rodel et al. [27, 93].

As a side note, the need to consider the temperature of the piezoelectric is not limited to ferroelectrics. Quartz, which only exhibits piezoelectricity, has accuracy limitations based on temperature. It was shown that the accuracy limitations present in quasi-static load cell test sequence was not attributed to creep, as expected, but temperature dependencies and nonlinearities of the material coefficients [94].

2.4 Summary and Comments

As shown, the family of piezoelectrics is varied and can be complex. The easiest way to define the piezoelectric response is through the linear constitutive equations. The linear constitutive equations work well for most piezoelectrics at low drive input levels, but at higher levels the ferroelectric response can cause large nonlinearities. These nonlinearities are a function of the electric field generated and the stress applied. To add to the complexity, piezoelectric transducers construction typically consists of multilayer stacks that are preloaded whose properties vary with the temperature and material composition and that degrade overtime.

The following properties are a stepping off point for a more thorough application consideration. Most designs will require a consideration of these items, yet these are by no means a complete list. For actuator designers, piezoelectric selection should require the consideration of the large-signal piezoelectric coupling coefficient, the loss coefficient and quality factor, and the maximum operating temperature. If the application require high linearity then the designer needs to consider the effect of temperature rise has on its properties. For a sensor designer this may be the utmost concern. Linearity and accuracy is

affected by temperature-dependent properties, creep and aging, loss coefficients and mechanical quality factor. For the energy harvester designer, the coupling coefficient, quality factor or loss coefficient are required considerations. An overview of the piezoelectric material properties can be found in Appendix B and device-dependent figures of merit can be found in Table B.4.

Lastly, it is important to understand the current market forces in piezoelectrics. Lead-free piezoelectrics are being researched to find material that is in compliance with the restriction of the use of certain hazardous substances in electrical and electronic equipment, or RoHS. The RoHS exemption will stay in force as long as there are no effective substitution [34]. It is important that designer understand the risk associated with designing and selecting leaded piezoelectrics.

Chapter 3

Giant Magnetostrictive Materials

Although magnetostrictive materials have been around for 175 years, they were only considered for some devices (especially actuators) in the past 45 years. The magnetostrictive effect was discovered in 1842 by James Joule in the measurements of iron and steel [95]. The first large-scale usage of this effect was during World War II when nickel-based alloys were used for sonar applications [96]. As most magnetostrictives had weak magnetostriction, magnetostrictive actuators garnered little interest [97]. In 1972, the discovery of giant magnetostrictive materials (alloys of rare-earth terbium and dysprosium with iron) allowed for a high strain output [6]. With these new materials, magnetostrictives strain was comparable with piezoelectrics.

Giant magnetostrictives materials (GMM) transduction properties are similar to piezoelectrics. Both have high bandwidth, good linearity and nano-scale resolution. Magnetostrictives advantage over piezoelectrics is that they can operate at low frequencies, even at DC [97]. The disadvantage of GMMs is their design complexity (requiring a permanent magnet, an actuation coil and a prestress device), cost (uses rare-earth metals), increased power consumption (from joule losses), weight and complex nonlinearities. Magnetostrictives are micro devices as their maximum strain is 0.10–0.18% [98]. Due to this, mechanical amplifications frames are used to increase the displacement [99].

Although GMMs have been around for a while, GMMs have not been used at a large-scale. GMM actuators are ready-made and have been applied to low-frequency acoustic transducer and ultrasonic cleaning [98, 100]. Yet, due to the cost there has been little high-volume applications. GMM load and dynamic force sensors have been built and show promise [101, 102]. Other non-GMM sensors have had successful implementation. For example, the nickel-based magnetostrictives are used for a fairly cost-effective contact-less absolute linear displacement sensor that has excellent range, resolution and temperature range [103]. One reason for the implementation difficulty could be that the bulk material costs are significant (USD \$0.5/g for Terfenol-D or USD \$0.08/g for Galfenol [104]).

To understand magnetostrictives, a discussion of its phenomenon and the application considerations and limitations can provide illumination of where the material is limited and may explain the market implementation difficulties of GMMs.

3.1 Physical Properties of Magnetostrictive Materials

Magnetostrictive materials are ferromagnetic materials operated in a certain manner. When a magnetic field is applied, the material experiences strain. Conversely, when a stress is applied, there is a change in the magnetic state of the material.

A discussion of magnetostrictives requires a phenomenological overview of ferromagnetics. Of interest are the phenomena that affect the magnetostrictive effect and the magnetomechanical effect. These phenomena can be explained by looking at two different scales: atomic scale (magnetic dipole moment orientation) and nanoscopic scale (domain wall motion). An in-depth overview of the origins of the magnetic dipoles will be omitted. For interested readers, Chikazumi's "Physics of Ferromagnetism" is suggested [105].

The following section will go through the elementary unit of ferromagnetics (the magnetic dipole moment orientation) in response to magnetic field and stress, the larger structural characteristic that introduces hysteresis (the magnetic domain structure) and its affect upon magnetization hysteresis, and another complex nonlinearity of ferromagnetics called anhysteretic magnetization. The purpose is to create a greater understanding of magnetostrictives phenomenon before discussing application-specific considerations.

3.1.1 Magnetic Dipole Moment Orientation

The magnetostrictive phenomenon can be described by two effects: the Joule and the Villari effect. The Joule effect is defined as a deformation induced by an applied magnetic field H. When this phenomenon was discovered by James Joule, the initial observation was of negative magnetostriction, or constriction, in iron and steel [100]. The inverse phenomenon is called the Villari effect and is defined as the change of magnetization B caused by an applied stress. The phenomenological explanation of these effects occurs at the atomic scale.

At the atomic scale, these effects are described through magnetic dipole moment orientation which is the elementary unit of magnetostriction. Magnetic dipole moments $\overrightarrow{m}$ are created by electron spins caused by incomplete occupied inner orbitals of an atom [106]. These dipole moments are constrained by the spin orbit coupling and are connected with the electron hull $-e$ shape [107]. This electron hull affects the Coulomb forces which in turn affects the lattice constants. When the material is above curie temperature, the magnetic moment orientation is random, see Figure 3.1 (a). As the material cools below curie temperature, the exchange interaction causes a parallel ordering of atoms [107], as shown in Figure 3.1 (b). When a magnetic field $\overrightarrow{H}$ is applied, the magnetic moments align with the direction of the field, as shown in Figure 3.1. This causes a rotation of the electron hulls and a change of the Coulomb forces throughout the material causing lattice strain which results in macroscopic strain, in both parallel $\lambda_{\parallel}$ and perpendicular $\lambda_{\perp}$ directions to the applied magnetic field. The volume conservation of the material results in the following relation, $\lambda_{\perp} = -\frac{1}{2}\lambda_{\parallel}$ [107].

The Villari effect works in reciprocal sense, as shown in Figure 3.2. When a stress is applied parallel to the direction of magnetic moments in the material, the lattice deforms

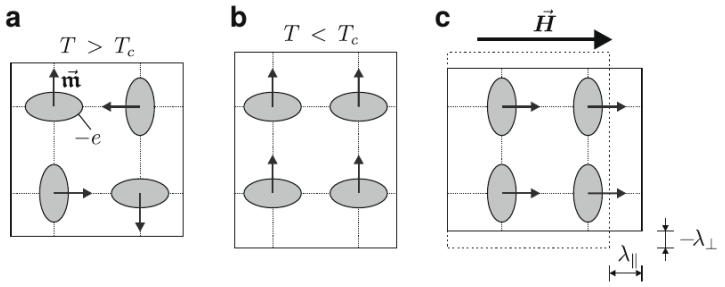

Figure 3.1: An illustration of the Joule effect, where T_c is curie temperature (Reprinted from [107], with permission from Elsevier).

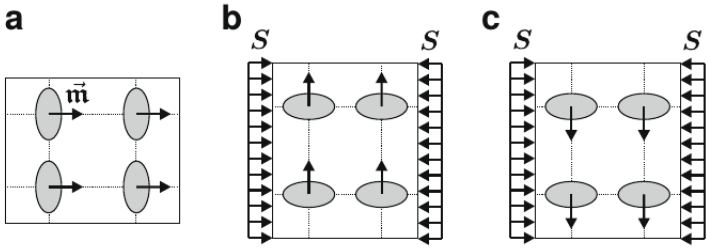

Figure 3.2: An illustration of the Villari effect, where T_c is curie temperature and S is stress (Reprinted from [107], with permission from Elsevier).

and causes a rotation of the magnetic moments, which is a lower energy state. As the stress does not force a certain orientation of the magnetic moment either Figure 3.2 (b) or (c) is possible. As both these states are possible, polycrystalline materials have reduced magnetic response due to conflicting fields [107].

The linear quasi-static constitutive equations shown in Equation 3.1 respectively describe the Joule and Villari relations and was defined in the 1973 IEEE Standard on Magnetostrictive Materials [108].

$$\begin{aligned} S &= s_{33}^{H}\sigma + d_{33}H \\ B &= d_{33}\sigma + \mu^{\sigma}H \end{aligned} \tag{3.1}$$

where S, σ, H, B are the strain tensor (m/m), stress tensor (N/m^2), magnetic field (A/m), and flux density (T), and s, d, and μ are the elastic compliance matrix (m^2/N), magnetostrictive coefficient (m/A), and relative permeability (H/m). The superscript σ like in μ^{σ} represents a measurement taken at constant stress [99]. As magnetostrictives are mainly operated in the 33-mode, the subscripts are normally omitted.

3.1.2 Ferromagnetic Domains

The magnetostrictive constitutive equations provide an approximation for operation of magnetostrictives at quasi-static and low-field operation. At higher field levels and higher

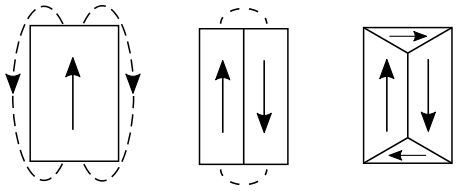

Figure 3.3: (a) Single domain and flux lines, (b) formation of 180° domains to reduce magnetostatic energy and (c) formation of 90° closure domains resulting in zero magnetostatic energy [106].

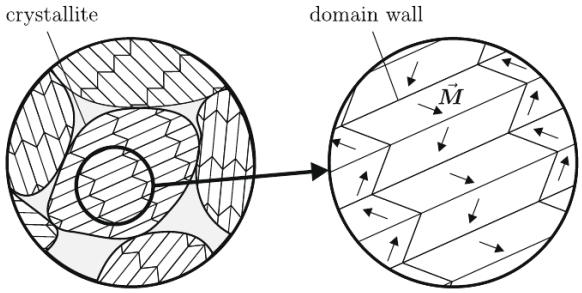

Figure 3.4: Domain structure of a magnetostrictive material (Reprinted from [107], with permission from Elsevier).

frequencies, nanoscopic scale domain interactions create nonlinearity and hysteresis in the output of the magnetostrictive.

Ferromagnetic domains are areas of parallel alignment of atomic moments that spontaneously form below the curie temperature [106]. These domains are created as they reduce the magnetostatic energy of the material, or the magnetic potential energy from the flux lines connecting opposite magnetic poles [106]. As shown in Figure 3.3 (a), a particle with single domain contains magnetic flux lines outside the material — arrows indicate the spin alignment direction of the domain. Domains are formed as long as the energy required to form a domain is less than the drop in magnetostatic energy. Thus a second domain of 180° orientation is formed to reduce the system energy, see Figure 3.3 (b). In some structures, especially cubic, 90° closure domains are formed that reduce the system energy [106]. As shown in Figure 3.3 (c), the creation of 90° domains results in the magnetic flux path never leaving the boundary of the material and creates a low magnetoelastic energy state. Similar to ferroelectrics, these 90° domain are the domains that respond to perpendicularly applied magnetic fields.

In a larger sense, these domains form a domain structure very similar to that seen in ferroelectrics, see Figure 3.4.

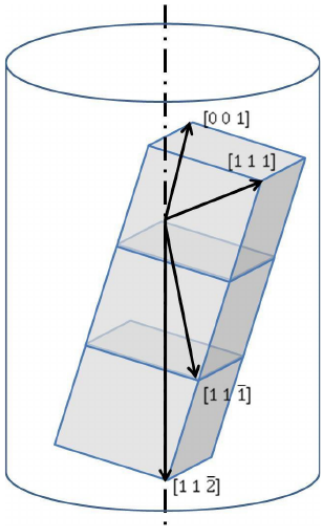

Figure 3.5: Orientation of Terfenol-D crystals ([109] ©1990 IEEE).

3.1.3 Initial Magnetization Processes and Hysteresis

The hysteresis in the magnetization process of ferromagnetics can be described through the two main phenomena: domain wall movement and domain rotation. Domain walls generally form at energetically favorable pinning sites that are made up of inclusions, impurities and stress inhomogeneities [18]. Domain wall movement, or domain growth, occurs as an applied field causes these pinned domain walls to reversibly bow or irreversibly displace [18]. Whereas, domain rotation is categorized as either reversible rotation near a easy axis or the irreversible rotation between different easy axes caused by an applied field. Both of these phenomena can be described through the initial magnetization process and are present, to some extent, during operation.

The following discussion will describe Terfenol-D magnetization process, which is manufactured in a certain orientation to maximize its properties. Terfenol-D should be manufactured with grain growth along the $[11\bar{2}]$ for maximum properties [97], as shown in Figure 3.5. The easy axes lie in the $\langle 111 \rangle$ set of directions at room temperature [18]. The result of the grain grown is that the magnetostrictive response depends on the uniaxial stress and applied magnetic field [97].

Figure 3.6 shows the response of magnetic domains to a magnetic field and the initial magnetization curve. The initial magnetization process starts with a demagnetized state which comprises domains with spontaneous magnetization M_0 yet zero bulk magnetization M due to random domain orientations, see Figure 3.6 (a). At low field levels, changes in magnetization is mainly caused by reversible domain wall movement and moment rotation, see Figure 3.6 (b). As the field levels increase, the dominant mechanism becomes irreversible domain wall growth, in direction near the applied field, and domain moments rotation to the easy axis closest to the field direction. Once in the irreversible boundary displacement region region between Figure 3.6 (b) and (c), the material will exhibit remanent magnetization even after field removal. At high field levels, increasing the applied field

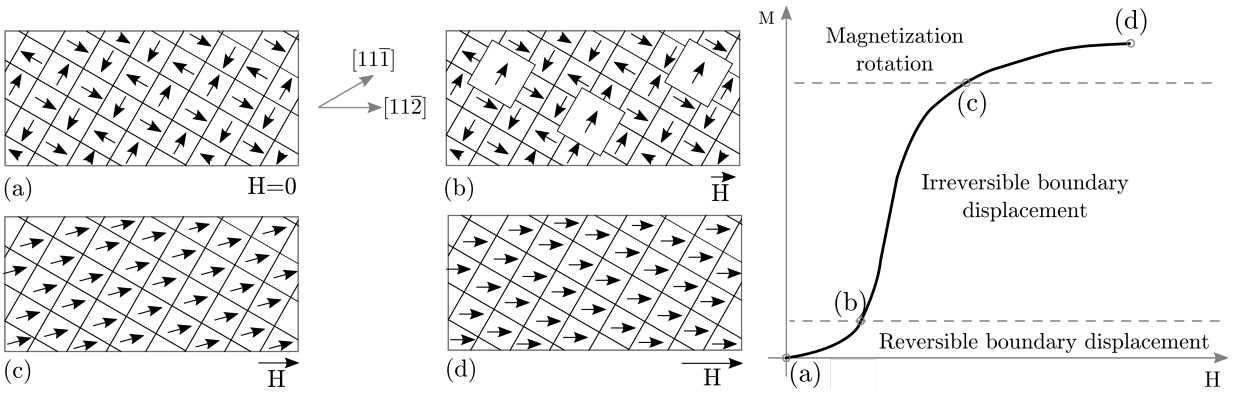

Figure 3.6: Initial magnetization process and dominant mechanism in the $(1\bar{1}0)$ plane of single crystal Terfenol-D due to applied field H in $[11\bar{2}]$ direction (left) and the magnetization flux-field relation(right) at (a) demagnetized state, (b) domain growth from domain wall motion, (c) rotation of moments to easy axis $[11\bar{1}]$, (d) saturation rotation of moments to align with applied field (left [18] and right [106]).

will result in small increase in magnetic flux as the material responds as a single domain and the magnetic moments rotate away from the easy axis to the direction of the applied field, see Figure 3.6 (c) to (d). Removal of applied field in this region will result in the domain returning to the energetically favorable easy axis.

Ferromagnetics have a hysteresis magnetic flux-field shape and the typical butterfly strain-field response, see Figure 3.7. The hysteresis shape is described in similar language to that of ferroelectrics. After the initial magnetization process (point O), the material exhibits a remanent magnetization B_R and remanent strain S_R at zero applied field. If a negative magnetic field is applied, the material will exhibit zero flux when the field strength equals the coercive field H_c. If the negative field is increased, it will result in domain orientation to the applied field. Even though the domains are oriented to the negative field, the strain will be the same as the atomic phenomenon causes an increase in lattice spacing when oriented along the parallel axis. The dashed line indicates the anhysteretic magnetization curve.

3.1.4 Anhysteretic Magnetization and the Magnetomechanical Effect

The anhysteretic magnetization curve represents a global energy minimum that ferromagnetics tend towards [110]. The most common observation of the anhysteretic curve is during the magnetomechanical effect, the change of magnetization by an applied stress cycle [111]. The anhysteretic magnetization process explains why previously unmagnetized structures become magnetized after an application of stress in the presence of the earth's magnetic field and why magnetized materials tendency to reduced magnetization after an application of stress [111]. It introduces a nonlinearity for ferromagnetic sensors and has significant practical implications.

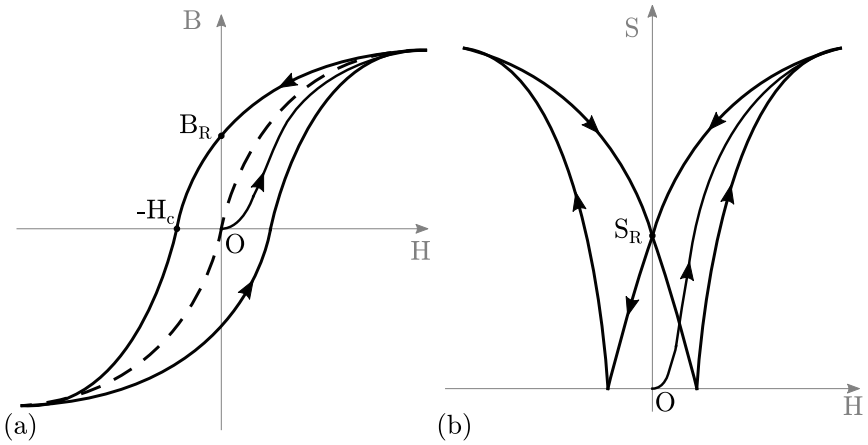

Figure 3.7: A comparison of ferromagnetic magnetic flux B and strain S response to magnetic field (Reprinted from [107], with permission from Elsevier).

The major hysteresis curve represents the domain orientation process during non-reversing applied field. Domains orient to their local energy minima but, due to the lack of sufficient energy, are not capable of tending towards the global energy minimum [18]. The local energy minima is a combination of magnetic easy axes and the local pinning sites. When enough energy is applied, there is enough energy to overcome the local minimia and pinning sites, and the material achieves the global energy minimum which is the called the anhysteretic magnetization curve[18].

The anhysteretic magnetization curve can be described by two phenomena: the tendency of the anhysteretic magnetization caused by the magnetomechanical effect and the dependence of the anhysteretic magnetization curve on the applied stress.

3.1.4.1 Tendency towards anhysteretic magnetization

Figure 3.8 shows how an applied compressive stress causes a specimen that is near to positive and negative remanence to tend towards anhysteretic magnetization. In the experiment by Pitman, a steel specimens, which were put into unmagnetized (not shown in Figure 3.8), positive and negative saturation magnetization, was loaded (400 MPa) and unloaded at constant magnetic field (H = 80 A/m) [110]. In all cases, the stress cycle caused the materials magnetization to change towards anhysteretic magnetization. This indicates that the introduction of an applied stress allowed the material to overcome energy barriers and tend towards the global minimum which is the anhysteretic magnetization curve [18].

3.1.4.2 Stress dependence of anhysteretic magnetization

The anhysteretic magnetic curve and the magnetization is shown in Figure 3.9. In this case, the material is steel and has a positive magnetostriction, or a tensile stress enhances the magnetization of the material. As the compressive stress increases, the magnetization process is further hindered.

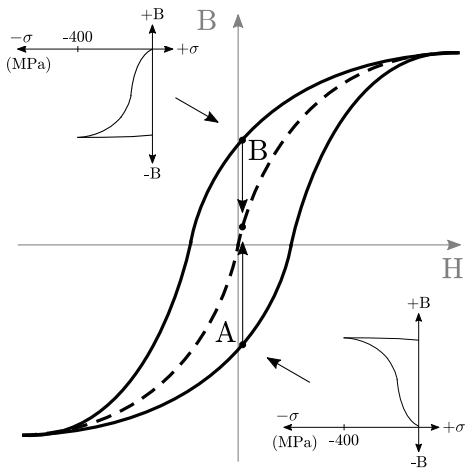

Figure 3.8: Schematic of ferromagnetic material flux density and applied field magnetic history to an applied stress ([110] ©1990).

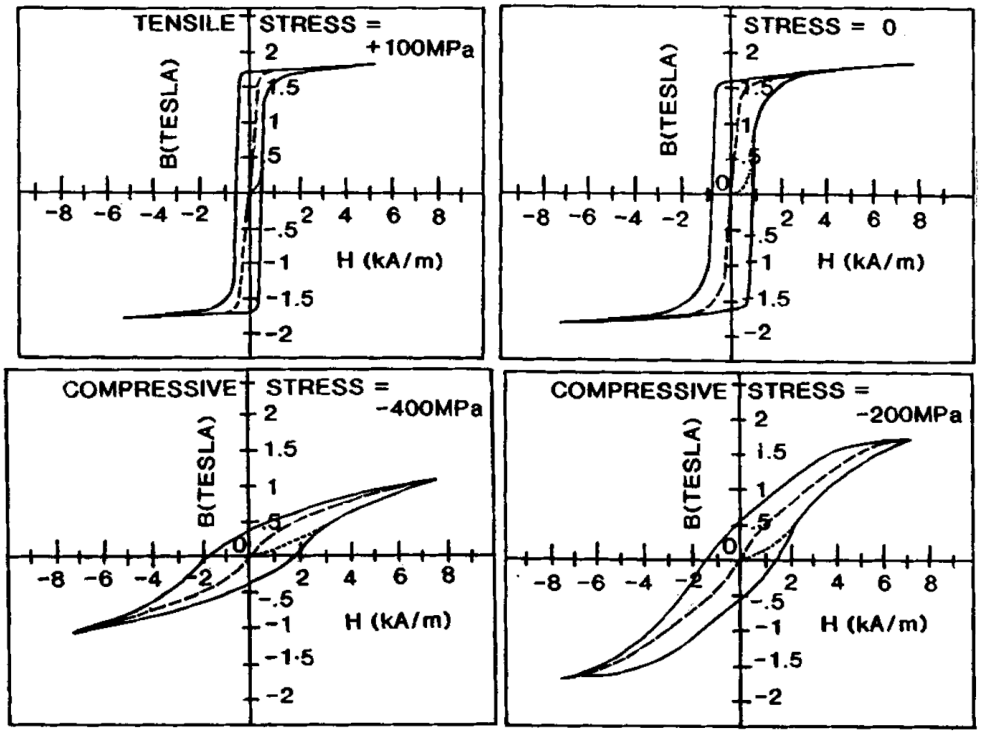

Figure 3.9: Hysteretic and anhysteretic magnetic flux density and applied field relation dependence upon applied stress from 100 MPa to -400 MPa ([110] ©1990).

Table 3.1: Summary of magnetostrictive effects [104].

Direct Effect	Inverse Effect
Joule effect Applied field results in change in dimensions	*Villari effect or magnetomechanical effect* Applied stress causes change in magnetization
ΔE *effect* Magnetoelastic contribution to magnetocrystalline anisotropy	Changes to elasticity caused by magnetic field
Wiedemann effect Torque caused by helical anisotropy	*Matteuci effect* Helical anisotropy and emf caused by a torque
Barret effect (Magnetovolume effect) Change in volume cause by magnetization (most evident at Curie Temperature)	*Nagaoka-Honda effect* Change of magnetic state caused by change in volume

3.1.5 Other Magnetostrictive Effects

Magnetostrictive materials are used in different ways to create actuators, contact-less position sensors and energy harvesters. The Joule effect is used in conjunction with the Villari effect in actuator designs [104, 100, 112]. The Villari effect is used in force sensing and energy harvesting. The non-GMM position sensors use a mixture of the Wiedemann effect and Villari effect to determine position of the movable position magnet, which allows the use of low magnetostriction materials [103]. An overview of all the magnetostrictive effects is shown in Table 3.1

3.1.6 Magnetic Material Coefficients

Some of the initial figures of merit to describe magnetostrictive materials are shown in Table 3.2. Maximum strain S_{max} is used instead of the widely used term called saturation magnetostriction λ_s due to the confusion λ has introduced [108]. While maximum strain shows the total strain output of the material, most actuators are used only in the quasi-linear region: for example, commercial Terfenol-D actuators have a maximum strain of 750–1000 10^{-6} [99]. The saturation induction B_s, or saturation magnetization M_s, indicates the amount of magnetic moments that can reorient in response to a larger applied field. The curie temperature T_c indicates the temperature at which the ferromagnetic–paramagnetic phase transition occurs. Magnetostrictive materials should be operated well away from its curie temperature to ensure proper operation [18].

3.2 Application Considerations

In practice, GMM transducers are packaged to improve functionality and life and designed to be operated dynamically. GMM transducers require mechanical prestress and permanent

Table 3.2: Magnetostrictive materials properties at room temperature except where indicated [18].

Material	S_{max} (10^{-6})	B_s (T)	T_c $(^\circ C)$	Y (GPa)	k	Ref.
Fe	-14	2.15	770	285		[18]
Ni	-50	0.61	358	210	0.31	[18]
Co	-93	1.79	1120	210		[18]
Tb	3000 (@-196$^\circ C$)		-48	55.7		[18]
Dy	6000 (@-196$^\circ C$)		-184	61.4		[18]
Terfenol-D	800–1200	1.0	380	18–90	0.7–.08	[113]
Metglas 2605SC	60	1.65	370	25–200	0.92	[18]
Galfenol	200–250	1.5–1.6	670	40–80	0.6–0.7	[114]

Table 3.3: Comparison of Terfenol and Galfenol Properties [104].

Parameters and properties		Units	Galfenol $Fe_{1-x}Ga_x$ *	Terfenol $Tb_xDy_{1-x}Fe_y$ **
Maximum strain	S_{max}	$10^{-6}m/m$	300–400	1600–2400
Density	ρ	kg/m^3	7870	9210–9250
Curie Temperature	T_c	$^\circ C$	675	375
Young's Modulus	Y^S	MPa	30–80	10–90
Elastic Compliance	s_{33}^H	$10^{-12}m^2/N$	17	42
Magnetostrictive Strain Constant	d_{33}	$10^{-9}m/A$	18	8–20
Magnetic Permeability	μ^S/μ_0		70	2–10
Bias Field (for actuation)		Oe	≈100	≈1000
Coupling Coefficient	k_{33}		0.38–0.78	0.6–0.85

* - 0.14<x<0.3

** - 0.27<x<0.3, 1.9<y<2

magnetic bias field to improve performance and ensure optimal operation life. As well, the dynamic operation causes significant nonlinearities and needs to be understood for a designer to properly operate. The following section will discuss the practical application and limitations of GMM transducers.

3.2.1 Material Selection

There are two main GMMs that are used as actuators, sensors and energy harvesters. Galfenol is viewed as the new and promising material as it is easier to implement in comparison to Terfenol-D, the most popular GMM.

Although Galfenol has 1/3 the maximum strain of Terfenol-D, it requires less than 1/10 the magnetic field to reach maximum strain, or saturation, see Table 3.3 [104]. Due to the reduced coil size requirements, Galfenol has better mass and volume efficiency than Terfenol-D [104]. Galfenol has less hysteresis than Terfenol-D and it is has little nonlinearity in the strain-applied field response, as shown in Figure 3.10 [115]. Furthermore, Galfenol

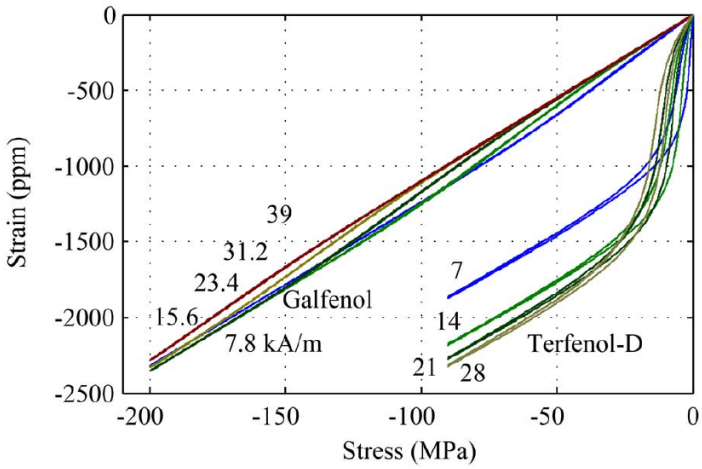

Figure 3.10: Stress-strain response of Terfenol-D and Galfenol at constant magnetic field ([115] ©2007 IEEE).

shows minimal variation in saturation magnetostriction at temperatures of $21°C$ to $80°C$, which indicates that it can be used in a larger range of temperatures without loss of magnetostriction [104]. Lastly, Galfenol has good machinability unlike Terfenol-D [116] and can be used in micro-scale films [117]. For these reasons, Galfenol has an advantage over Terfenol-D in many applications [118]. A full overview of the magnetostrictive material properties of theses GMMs can be found in Appendix B.

3.2.2 Magnetomechanical properties

The material properties previously indicated in Table 3.2 and 3.3 are collected during quasi-static operation. Yet, most applications will not have such stability or single varying inputs. The following section will go through some of the important magnetomechanical properties and how they shift during different operation parameters.

3.2.2.1 Young's Modulus

During normal operation, the Young's modulus of ferromagnetic materials changes from 0.4–18%. Yet, for Terfenol-D, for example $Tb_{.28}Dy_{.72}Fe_2$, the change of Young's Modulus $\Delta Y/Y_0$ can be up to 161% [119]. The constitutive equations have a relation between the Young's modulus of Y^H and Y^B. As it is preferable to show the coupling coefficient k_{33}^2, it will be described with compliance s, which is the inverse of Young's modulus. In Equation 3.2, the compliance at constant magnetic induction s^B is smaller (or stiffer) as all available magnetic energy is converted to elastic strain energy [119].

$$s^B = s^H(1 - k_{33}^2) \quad \text{or} \quad \frac{1}{Y^B} = \frac{1}{Y^H}(1 - k_{33}^2) \tag{3.2}$$

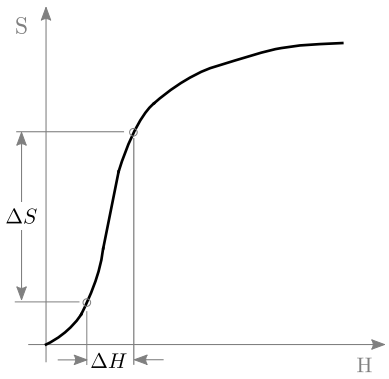

Figure 3.11: An illustration of the magnetomechanical coupling coefficient [97].

Although most designers would prefer to avoid these issues, some designers will find that the variation in Young's Modulus allows for tuning a vibration isolator to the resonant frequency of the system with virtually no impact on the damping signature [119].

Note the formula provided by Olabi and Grunwald ($Y^H = Y^B(1 - k_{33})$ [100]) has two errors: the coupling coefficient k_{33} should be squared and the last term in the bracket is not equal to k_{33}, which is shown in Equation 3.3, but is equal to $e_{33}^2/(\mu_3^S c_{33}^B)$ where $e_{33} = d_{33}/s_{33}^H$ and stiffness $c^B = Y^B$.

3.2.2.2 Magnetostrictive Coupling and Magnetostrictive Coefficients

In the constitutive equations, energy is converted between the magnetic and mechanical domain. The efficiency of this conversion is denoted by the magnetomechanical coupling coefficient. The coefficient varies from 0.5–0.95% based upon the material [100]. The coupling coefficient is described as such:

$$k_{33}^2 = \frac{d_{33}^2}{\mu_3^T s_{33}^H} \tag{3.3}$$

where the s_{33}^H is the elastic compliance at constant field. The magnetostrictive coefficient d_{33} is the slope of the strain over the magnetic field (S – H).

$$d_{33} = \frac{\mathrm{d}S}{\mathrm{d}H} \tag{3.4}$$

The magnetomechanical coupling coefficient is generally calculated at the optimal working range, which occurs when the magnetostrictive has a bias magnetic field applied. As shown in Figure 3.11, the magnetomechanical working range starts at the beginning of the near-linear region that also has the highest slope, which results in a greater magnetomechanical coupling and better linearity.

However, both the magnetomechanical coupling coefficient k_{33} and the magnetostrictive coefficient d_{33} change during operation. In Figure 3.12, the magnetomechanical coupling

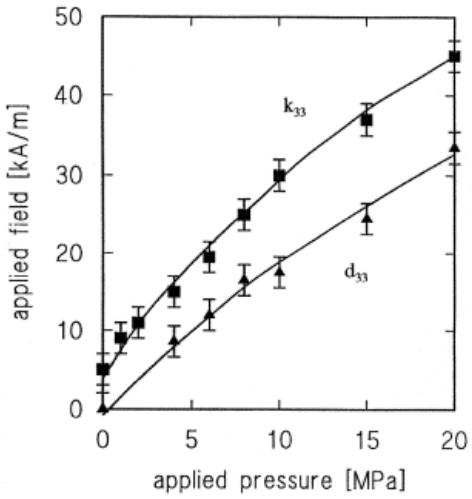

Figure 3.12: Terfenol-D k_{33} and d_{33} coefficients dependence on applied stress (Reprinted from [97], with permission from Elsevier).

coefficient and magnetostrictive coefficient dependence on the applied stress are shown for Terfenol-D. For optimal coupling coefficient or magnetostrictive strain coefficient, a specific prestress and magnetic field needs to applied to maximize these coefficients [97].

3.2.2.3 Quality Factor

An important property for some designers is the quality factor, which is the ratio of energy stored and energy lost per cycle. At resonance, the longitudinal strain produced in a magnetostrictive is defined as:

$$S_{33} = Q_m d_{33} H_3 \tag{3.5}$$

where Q_m defines the amplification at first resonance under quasi-static conditions. The unconstrained quality factor Q_H of unlaminated Terfenol-D is in the range of 3–20 [120]. If the material is laminated, then Terfenol-D can reach quality factors of 112 with a specific bias field and prestress [121]. Unlaminated Galfenol shows values of 13.5 at room temperature [122].

3.2.2.4 Permeability

As ferromagnetic materials have a relatively high permeability, they are described through a relative permeability constant. The relative permeability is the required multiplication of the permeability of free space μ_0 to indicate the permeability of material. So, this factor indicates the magnification of magnetic effects in the magnetic material, which is defined as the amplitude of magnetic flux density in magnetic material with a given magnetic field.

The relative permeability is a function of prestress and the frequency of operation [100]. With increasing prestress, the relative permeability decreases. It is possible that this elastic

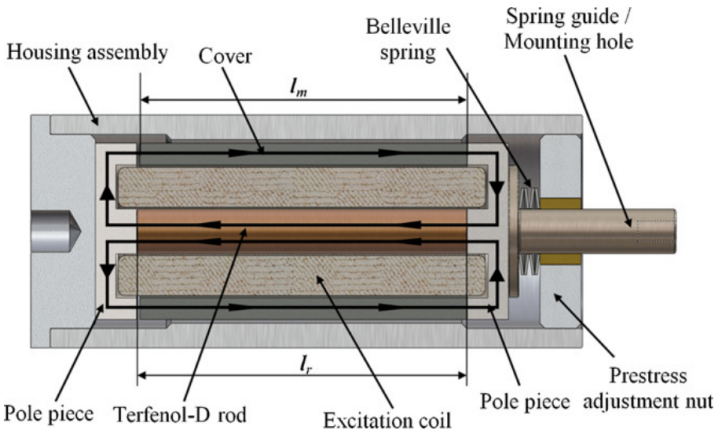

Figure 3.13: Cross section of a typical GMM actuator (Reprinted from [99], with permission from Elsevier).

strain energy constrains the domains from reorienting to the magnetic field, and results in a smaller relative permeability.

The relative permeability is higher at constant stress μ_3^T than at constant strain μ_3^S and is defined as:

$$\mu_3^S = \mu_3^T(1 - k_{33}^2) \tag{3.6}$$

where the relative permeability at constant strain is useful to define the material in its clamped state (S=0). At the clamped state, the magnetic domains are not capable of orientating as the strain is constrained.

3.2.3 Actuation Optimizations

Most GMM transducers are packaged with a mechanical prestress and a magnetic bias, see Figure 3.13. While it is not mandatory, both mechanical prestress and magnetic biasing allows for improved response at the cost of increased design complexity, weight and size.

3.2.3.1 Mechanical Prestress

GMM actuators are designed with a mechanical prestress. This mechanical prestress loads the magnetostrictive material in compression which provides multiple beneficial properties. Terfenol-D, for example, is quite weak in tension (tensile strength $\approx$ 28MPa) in comparison to compression (compressive strength $\approx$ 700MPa), and requires compressive prestress to withstand inertial forces [123]. As well, a compressive prestress improves the magnetomechanical coupling coefficient through improving the magnetic state of magnetostrictive material. If a material is unloaded it will have domain orientation in all eight of the $\langle 111 \rangle$ easy directions and the demagnetized length will not be at a minimum [123]. When a moderate compressive stress is applied, the material will elastically deform and

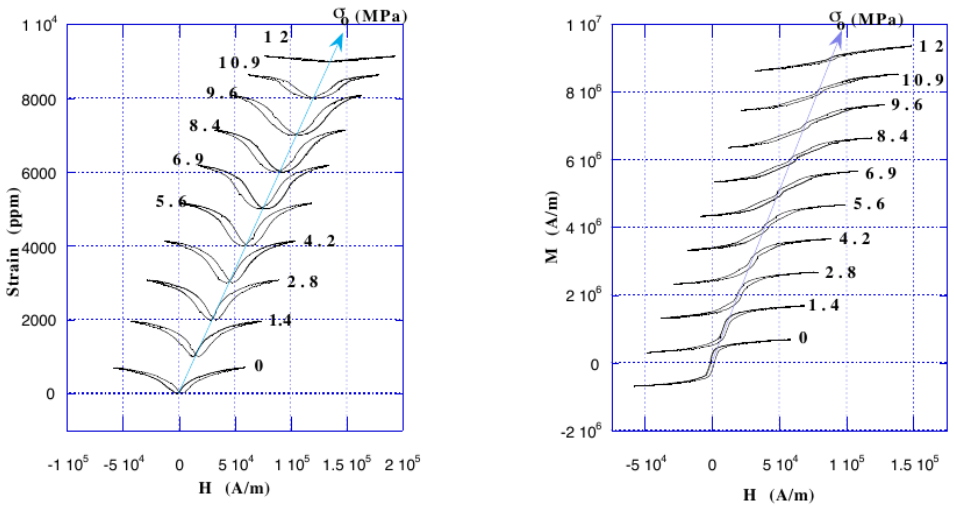

Figure 3.14: (a) Magnetostriction and (b) magnetic Field against applied field at various stresses. ISU transducer, 12.7 mm diameter solid material, near-DC frequency of operation [124].

this, in turn, will cause an increased quantity of domains to orient in the direction perpendicular to the applied stress axis [124]. If the compressive stress is too large, the elastic energy and magnetostrictive effect will be overpowered, as shown in Figure 3.14 where the 12MPa output is almost completely blocked. If the proper bias stress is applied, the strain capability of Terfenol-D can increase by a factor of 3 [112].

3.2.3.2 Magnetic Biasing

Due to the nonlinear nature of the magnetic field-strain response of magnetostrictives, it is common to apply a magnetic field to bring the material to the steepest part of the response curve. The application of a magnetic bias can improve efficiency, coupling, axial strain, permeability and elastic modulus [124]. Furthermore, the use of a permanent magnetic bias can allow the transducer to be used with a bipolar current signal which reduces joule losses [112]. Lastly, the use of biasing allows for the actuator to be operated bidirectionally, see Figure 3.15.

Both the magnetic biasing and mechanical prestress are coupled. Therefore, for a proper understanding of the response of the material to the mechanical prestress and magnetic biasing requires an analysis of both minor and full loops, as shown in Figure 3.16.

3.2.4 Temperature-Dependent Behavior

Magnetostrictive performance is quite temperature dependent. From Figure 3.17, the shift in performance from $-50°C$ to $0°C$ is quite notable, and indicates why Terfenol-D should be operated near to or above room temperature.

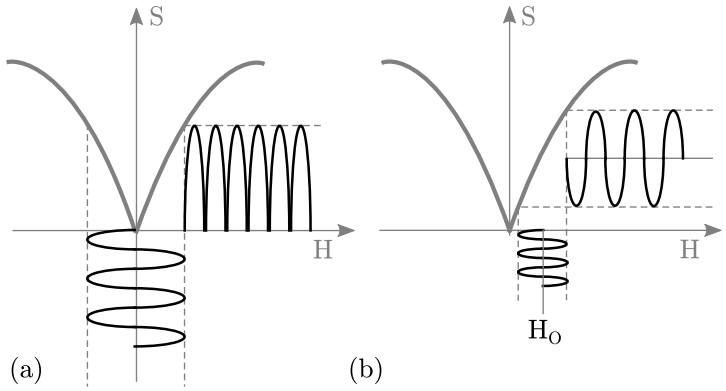

Figure 3.15: Magnetostriction (a) without and (b) with magnetic biasing [99].

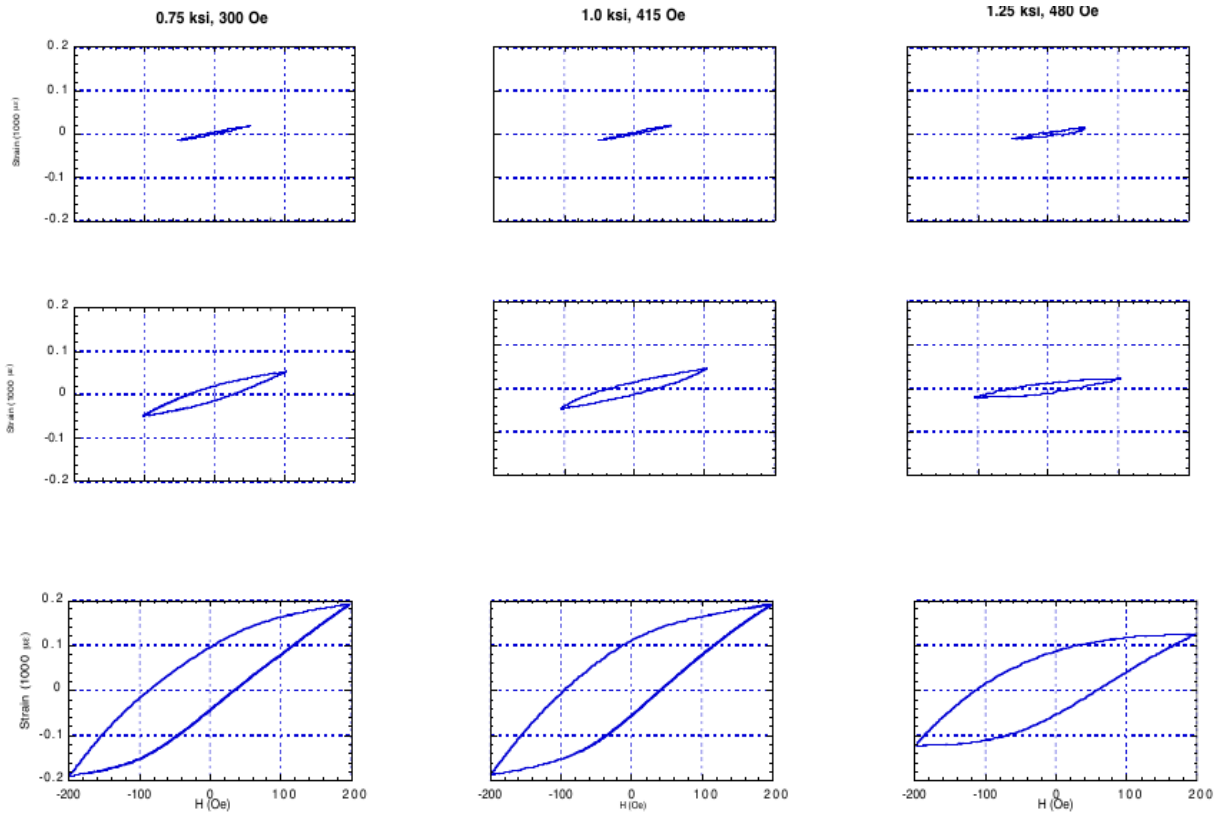

Figure 3.16: Strain-applied field minor loops. Bias Condition (left to right): 5.2 MPa, 24 kA/m (0.75 ksi, 300 Oe); 6.9 MPa, 33.2 kA/m (1.0 ksi 415 Oe); 8.6 MPa 38.4 kA/m (1.25 ksi, 480 Oe). AC Drive Fields (top to bottom): 4, 8, 16 kA/m (50, 100, 200 Oe). ISU 12.7 mm diameter rod transducer, 0.75 Hz excitation [125].

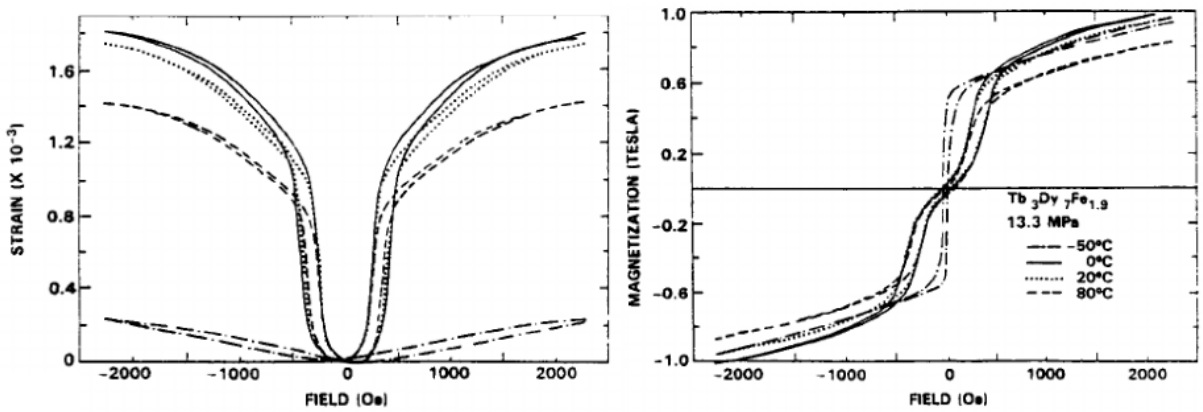

Figure 3.17: Quasi-static temperature effects of Terfenol-D at 13.3 MPa Compressive Stress (Reprinted from [126] with permission from SAGE).

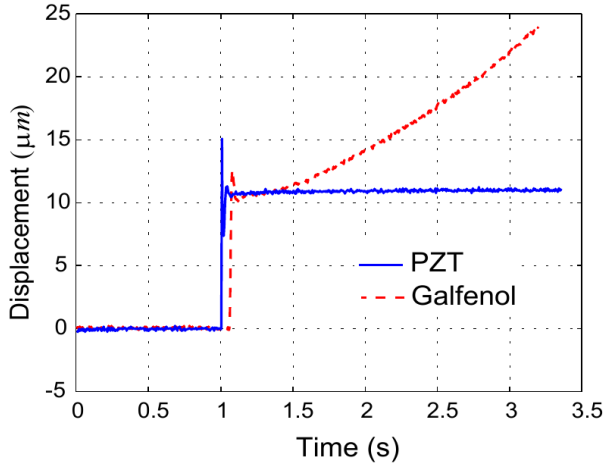

Figure 3.18: Steady-state position of PZT and Galfenol without temperature control (Reprinted from [128] with permission from SPIE).

Heat also can negatively affect the transducer performance. Ohmic heating in the excitation coil can result in one of the largest losses, aside from hysteresis and eddy currents. Other thermal effects can occur and indicate the need to consider thermal effects, such as thermal expansion of the magnetostrictive core, thermal effect on magnetostrictive coefficients, thermal expansion of the coil and other transducer components [124].

The thermal effects is an issue with magnetostrictives. A steady state output will cause heat generation and further degrade performance and steady-state position, see Figure 3.18. To overcome this some have suggested using some form of cooling device, similar to what is found on a electromagnetic motor [127, 128].

3.2.5 Eddy Current Effects

When the material is dynamically operated, there is eddy currents in the material that resist the applied magnetic field. As well, the effect of eddy currents create a skin effect, which creates a non-uniform distribution of current. These eddy currents create a magnetic flux that resists the applied field and can lead to inoperable transduction at higher frequencies [123]. Furthermore, the eddy currents results in ohmic heating, which reduces power transfer, and a reduction in effective permeability. To minimize the eddy current effects, magnetostrictive materials are normally laminated and stacked. This results in smaller eddy current effects at increased manufacturing costs.

3.3 Summary and Comments

As was shown, giant magnetostrictives materials are more complex than piezoelectrics. The linear constitutive equations can be used for quasi-static operation but at higher drive levels the domain interactions can cause greater hysteresis and nonlinearity. These domain interactions are a function of the applied stress, magnetic field and temperature. Furthermore, steady-state position control results in joule heating of the coil which can cause significant nonlinearity and loss of favorable magnetomechanical properties.

For the selection of giant magnetostrictive materials, it is important for the designer to consider application properties. For actuators, the maximum strain, magnetostrictive strain coefficient, saturation magnetization, curie temperature and temperature dependent behavior are important. For sensors, the lack of temperature sensitivity of Galfenol and its ability to be implemented on micro-scale films and its smaller bias magnetic field allows for a more compact design. For energy harvesters, the coupling coefficient, quality factor and elastic modulus should be considered. An overview of the collected material properties for Terfenol and Galfenol can be found in Appendix B.

Although GMMs have been around for a while, they are a difficult material primarily due to material nonlinearity and the significant design complexity that is present. Furthermore, the bulk material cost and manufacturing cost can increase the cost significantly that makes magnetostrictives rarely seem the optimal pick.

Chapter 4

Shape Memory Alloys

Shape memory alloys (SMAs) are promising materials that have a rigorous research effort. SMAs were realized in 1963 by the discovery of nickel-titanium alloy (NiTi or nitinol) by the Navel Ordinance Laboratory but was limited in temperature [2]. In an attempt to expand the property range, the study of SMA ternary additions allowed thermal hysteresis properties, residual strain buildup properties and transformation temperatures to be adjusted which resulted in the first large-scale SMA application using a shape memory effect pipe coupling called Cryofit for the F-14 fighter aircraft [129]. The application of SMAs is varied due to the its phenomena. SMAs can be found in our brasseries, eyeglass frames and orthodontic wires to our cars, planes and satellite structures.

In general transduction terms, NiTi SMAs have excellent biocompatibility, good wear resistance, high energy density, high stress and elasticity [130], but they have large hysteresis, long cycle times, environmental temperature limitations, low efficiency ($\approx$1%) [131] and moderate cycle life ($\leq 10^7$). SMAs are a microscopic to mesoscopic device due to its respectively large strain of up to 8 %, although it is suggested that only 4–5 % strain be performed for cyclic operations [132]. Most SMAs are purchased as bare wires and range in diameter of 20 – 510 μm with most applications using smaller wire diameter since fatigue life and actuation frequency degrades with increasing diameter [133]. The NiTi Miga Motor is one of the few packaged and ready-made SMA actuators — it has a stroke of 9 mm, output force of 11 N and actuation time of 0.5 s [134].

SMA actuators are either found as linear actuators (e.g. automotive climate control flaps and hatch vents) or active thermal actuators (e.g. anti-scald valves and industrial safety valves) [130]. Most of the time SMAs are not solely used as sensor but a self-generating sensor element, which can react to the changing temperature.

SMAs have significant commercial, industrial and academic interest, yet most applications are hindered by the difficulty in understanding and applying the complex properties of SMAs [130]. The underlying issue is that most designers lack knowledge of the technical limitations and application considerations that bar the implementation of SMAs. Therefore, it is necessary to discuss the phenomena, the technical limitations and the application considerations for proper design implementation of SMAs.

4.1 Physical Properties of Shape Memory Alloys

SMAs are a group of intermetallic alloys that exhibit two phenomena: shape memory effect and superelasticity. The shape memory effect (SME) is the phenomenon where the material recovers its shape, or strain, after apparent plastic deformation through heat-induced phase transformation. Superelasticity (SE) is the isothermal recovery of large strains during a mechanical load–unload cycle that occurs near to or moderately above the high temperature phase transition.

This section will go through a nano-scale view of the atomic phase transformation that results in the macroscopic shape memory effect and superelasticity phenomena. Due to these transformations which involve change of crystal structure, SMAs exhibit transformation-induced plasticity that results in fatigue failure at large amount of cycles and limits its uses.

4.1.1 Phase Transformation Phenomena

Shape memory alloys are intermetallic alloys that have a nearly reversible diffusionless phase transformation process. In normal operation, SMAs exhibit two phases which have different crystal structures and properties. The high-temperature stable austenite phase has high symmetry — generally from cubic crystal structure. The low-temperature stable martensite phase has less symmetry — generally tetragonal, orthorhombic or monoclinic crystal structure [2]. When a SMA transforms from austenite to martensite, also known as martensitic transformation, the transformation is diffusionless and is caused by shear lattice distortion. When the martensite crystal is formed, it can take different orientation directions which are called variants. The two forms that the 24 NiTi martensite variants take are twinned martensite M^t, which is an self-accommodated arrangement of martensite twins such that system energy is minimized, and detwinned martensite which is composed of a specific dominant variant M^d [135]. This martensite transformation is reversible from austenite, the parent phase, to martensite, the coherent product phase, and is the elementary phenomenon of SMAs.

When a high-temperature no-load austenite SMA is cooled, the martensite transformation, or forward transformation, takes place and martensitic variants form. The martensitic variants take on a special zig-zag deformation pattern called twinning, see Figure 4.1 [135]. Twinning occurs as the variants next to the grain boundary must satisfy the grain boundary conditions while variants in the middle of the grain attempt to minimize internal energy [135]. If the no-load martensite is heated past the martensite–austenite phase transition, the reverse transformation occurs but results in no macroscopic shape change. The lack of shape change is due to the self-accommodation of martensite, which is the twinning pattern formed that minimizes the internal energy which includes the strain energy.

Both the forward and reverse transformation are shown in Figure 4.1 where four phase transformation temperature variables are indicated. During cooling, or forward transformation, austenite starts and finishes transformation to martensite respectively at the martensitic start temperature M_s and martensitic finish temperature M_f. The material

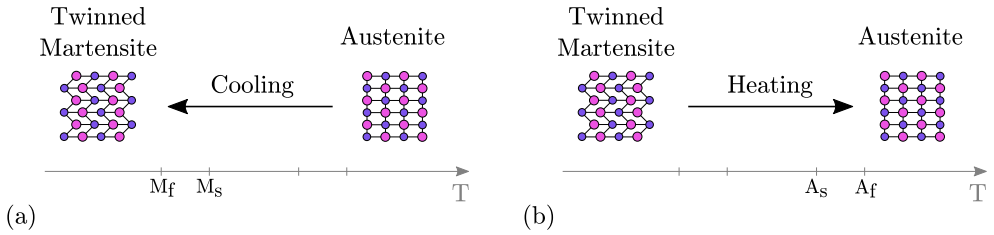

Figure 4.1: (a) Forward transformation of austenite to twinned martensite from cooling and (b) reverse transformation from twinned martensite to austenite from heating, where T is temperature [2].

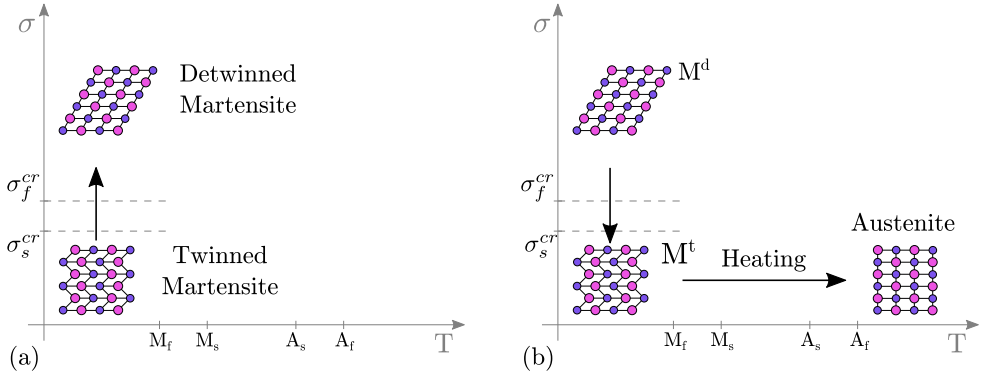

Figure 4.2: (a) Detwinning process and (b) shape memory effect from unloading of detwinned martensite and heating to austenite after load removal [2].

form then is fully twinned martensite. During reverse transformation, or heating, the transformation starts and finishes respectively at austenitic start temperature A_s and austenitic finish temperature A_f.

When a mechanical load is applied to a twinned martensite phase, detwinning begins as martensitic variants reorient, as shown in Figure 4.2 (a). Through the detwinning process, the martensitic variants form in orientation of the stress and macroscopic deformation is exhibited. This detwinning process produces apparent plastic deformation which remains after load removal. The reason for the apparent deformation is that there is not enough energy for the variants to go to the lower energy twinned martensite form. This apparent plastic deformation is fully recovered when the reverse phase transformation from detwinned martensite to austenite occurs through heating, see Figure 4.2 (b). After the reverse transformation, if the material is cooled, or the forward transformation occurs, twinned martensite is again formed. This is known as the shape memory effect (SME). To start the detwinning process a sufficiently large load, called detwinning start stress σ_s^{cr}, is needed, and the detwinning process finishes at the detwinning finish stress σ_f^{cr}.

If a loaded ($\sigma > \sigma_f^{cr}$) austenitic SMA is cooled, detwinned martensite will form and the material will deform. Subsequent heating will result in deformation recovery starting at temperature A_s^{σ}, see Figure 4.3. The transformation temperatures are stress dependent where higher stress results in higher energy, or temperature, required for transformation to occur. The shift of transformation temperature is independent of the sign of the stress

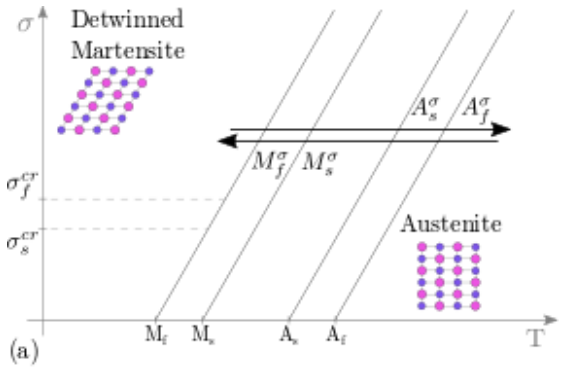

Figure 4.3: Thermally induced phase transformation at a stress above detwinning finish stress σ_f^{cr} from austenite to detwinned martensite [2].

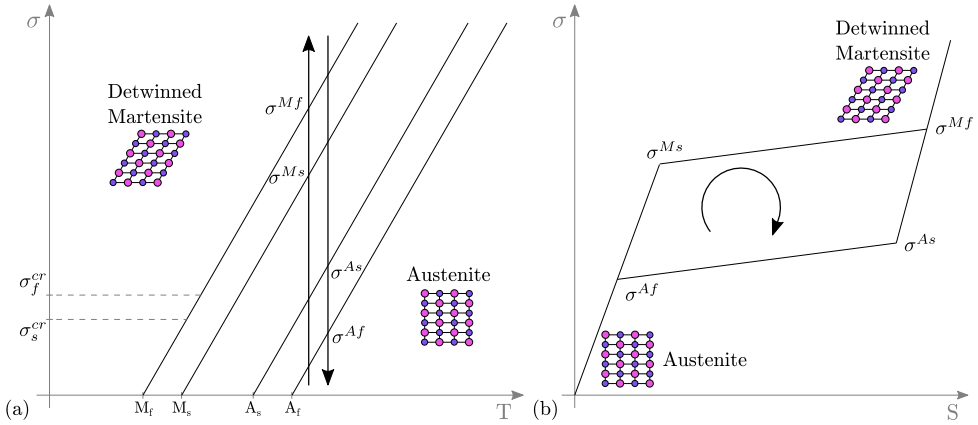

Figure 4.4: (a) Mechanically-induced forward and reverse transformation above A_f and (b) representation of stress-strain behavior of the superelastic effect [2].

so both compressive and tensile stresses resulting in an increase in the transformation temperature.

Mechanically-induced phase transformation, or superelasticity, is also possible if a mechanical load is large enough to create stress-induced martensite. When a increasing load is applied to an fully austenite SMA, the austenite structure starts to shift to detwinned martensite and macroscopic deformation occurs, see Figure 4.4 (a). If the load is removed, the material returns to austenite and the strain is recovered. Figure 4.4 (b) describes the stress-strain phase transformation behavior of the superelastic effect. The start and finish stress of the martensitic transformation is respectively represented by σ^{Ms} and σ^{Mf}. When stress is lowered, the SMA experiences the start and finish reverse transformation to austenite represented by σ^{As} and σ^{Af}. The difference between the martensite and austenite stress is the measure for mechanical hysteresis present in SE SMAs. If the material is partially transformed (i.e., temperature is below A_f) only partial strain is recovered after load removal.

As shown in Figure 4.5, superelasticity and shape memory effect can occur in the same composition and is dependent upon temperature. If the temperature is above A_f and

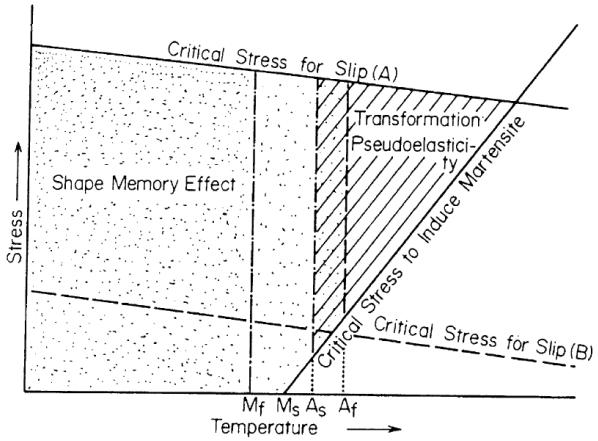

Figure 4.5: Stress-temperature behavior of a SMA showing SME and SE (or transformation pseudoelasticity) (Reprinted from [136], with permission from Elsevier).

the stress is applied below a critical stress for slip, then the material recovers fully upon load removal. If the stress exceeds critical stress for slip (A), then permanent deformation occurs even with stress removal. In some compositions, the critical stress for slip is low enough that superelasticity can not occur before slip (B). For compositions of NiTi that can exhibit both SE and SME effects, the stress-strain relation is temperature dependent as shown in Figure 4.6.

4.1.2 Shape Memory Effect

The shape memory effect is a thermomechanical cycle that can occur through the application and removal of a load, causing apparent strain, and subsequent heating above A_f causing strain recovery. The SME effect can be described through a thermomechanical cycle shown in Figure 4.7.

When an unloaded austenite SMA is cooled, it shifts from austenite to twinned martensite, see segment AB in Figure 4.7. If a load is applied, the martensite exhibits mainly elastic properties until σ_s^{cr} when the applied stress starts to cause shear distortion of the lattice structure. At stresses above σ_s^{cr}, the martensitic variants reorient into favorable orientations and causes an increase in strain at nearly constant applied stress. Once most of the thermally available variants are reoriented, the detwinning process and the plateau is basically complete at a σ_f^{cr} stress and other phenomena become dominant. As the stress is increased to Point C, a function of detwinning, elastic and plastic strain occurs [137] — plastic strain buildup will be discussed in Section 4.1.4 and 4.2.6. From segment CD, the material is unloaded and elastically recovers some strain although apparent plastic deformation caused by the detwinned martensite is still present. As shown in segment DEF, the material is heated and once it reaches the austenite start temperature A_s where the reverse transformation and strain recovery commences. At the austenite finish temperature A_f nearly all the apparent plastic deformation is recovered. The strain recovered from the material going from detwinned martensite to austenite is referred to as recovered strain

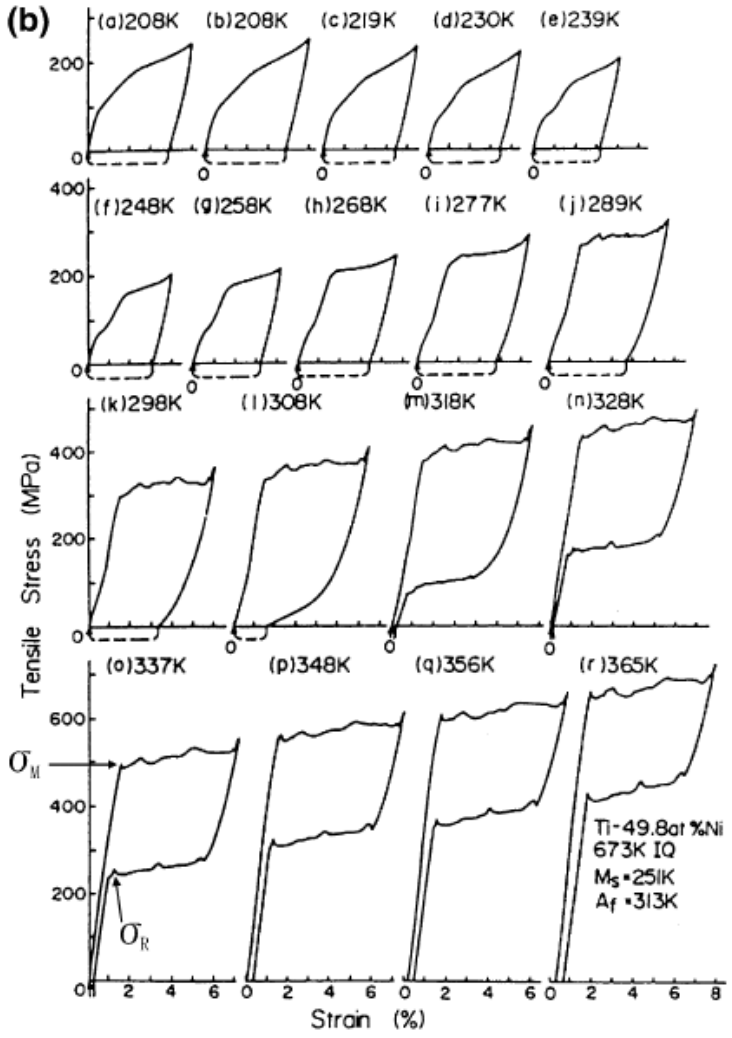

Figure 4.6: The effect of temperature on the stress-strain relationship of a Ti-49.8Ni alloy annealed at 673 K after 1 hr of cold work (Reprinted from [136], with permission from Elsevier).

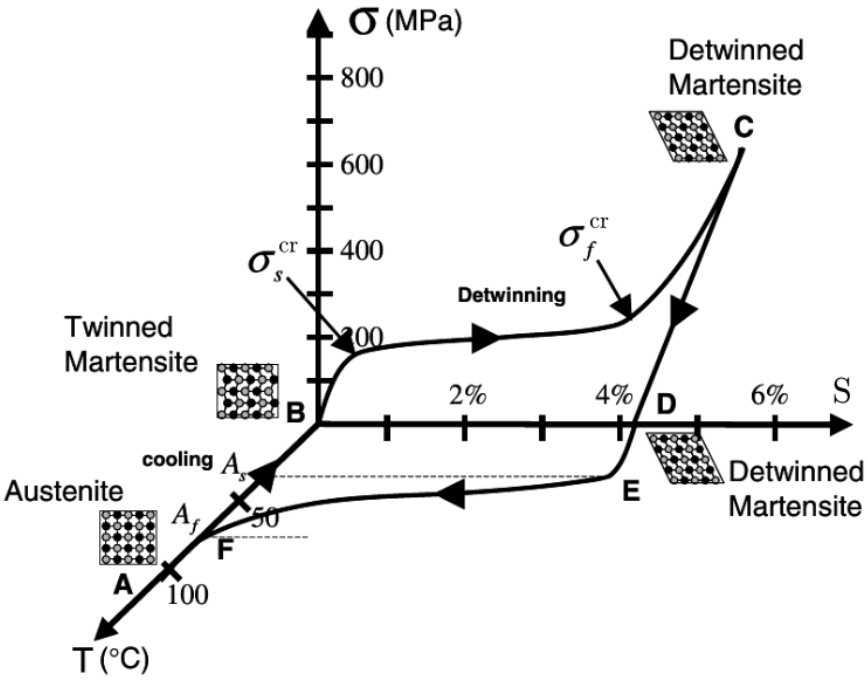

Figure 4.7: Stress-strain-temperature behavior of a NiTi SMA (Reprinted from Springer Customer Service Centre GmbH: [2]).

S^{rec}. Cooling will result in twinned martensite to form and the cycle can repeat. The thermomechanical cycle described is called the one-way shape memory effect (OWSME) as it requires an applied mechanical load (generally a spring or a weight) to deform the SMA.

4.1.3 Transformation Temperatures

The no-load SMA transformation temperature is normally measured by a differential scanning calorimetry instrument and using the tangent method, see Figure 4.8 (a). While this provides an indication of stress-free transformation temperature, the transformation temperature is also a function of the applied stress and measurements should match the application as closely as possible. If the SMA is in a constant-load configuration, then measuring temperature alongside strain measurement is a better indication of the transformation temperatures present, see Figure 4.8 (b).

Furthermore, the NiTi SMA transformation temperature is a function of the composition and thermomechanical history. A compositional decrease of 0.1 at.% Ni can result in a +10 °C shift of martensite start temperature, where the maximum M_s temperature is roughly 67 $°C$ (340 K) [139]. Due to this high compositional dependency, NiTi production requires higher tolerances and thus costs more [135]. As well, the thermomechanical history can have a complex effect on the transformation temperature either through processing, dislocation buildup and aging. For example, the affect of annealing temperature and time on a Ti-50.8Ni at.% can change the austenite finish temperature from -20 to 60 °C [140].

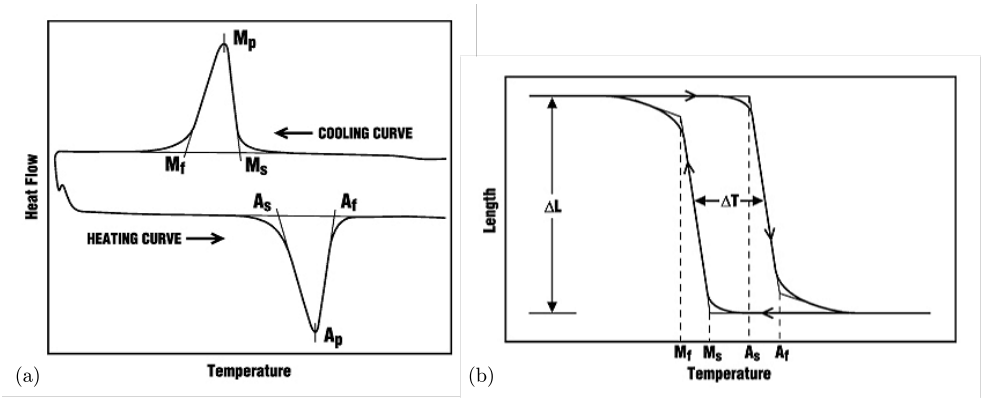

Figure 4.8: (a) Differential scanning calorimetry output and (b) constant-load strain-temperature relationship with the transformation temperatures determined through tangent method [138].

It is well known that the thermal cycling can result in beneficial dislocation buildup that initially shifts the transformation prior to stabilization [141] but it is also dependent upon room-temperature aging after thermal cycling affects the transformation temperature as well [142].

4.1.4 Cyclic Behavior

Normally, SMAs need a recovery force to cause strain. However, SMAs are capable of stress-free shape change during thermal cycling by applying a certain thermomechanical treatment. This phenomenon is called the two-way shape memory effect (TWSME). The TWSME is observed in SMAs that have experienced repeated thermomechanical cycling at constant or variable load, which is also called training or stabilization. Repeated thermomechanical cycling causes plastic strain buildup in the material. This plastic strain causes the material to transform into certain preferential martensite variants [143].

There are many different training techniques to obtain the TWSME in SMAs. The most common training technique is deformation of martensite with constrained or unconstrained recovery [143]. In Figure 4.9, the training technique is thermal cycling at constant stress of 150 MPa. As seen, there is a difference from the strain generated during heating and the recovered strain S_{rec} from cooling. The difference is the plastic strain buildup, or residual deformation (RD) S_{res}. For each thermal cycle, there is an increase in the total RD S_{res}^{total} and a reduction in the rate of the plastic strain buildup per cycle until the plastic strain per cycle is stabilized. Further cycling will result in plastic strain buildup but at a relatively constant amount per cycle, see Section 4.2.6 about fatigue failure. Training is beneficial as it can stabilize the material and is performed by most SMA actuator manufacturers.

The TWSME is caused by changing the internal stress state of the material. Through buildup of defects caused during training, the preferred martensite variants are formed during cooling even when the material is stress-free [143]. The stability of TWSME may change depending upon the thermomechanical and mechanical cycles it experiences.

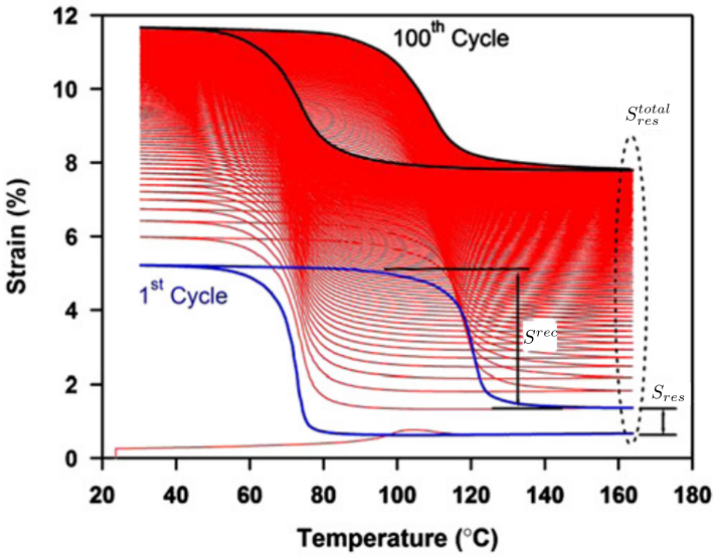

Figure 4.9: An example of the residual strain evolution of a thermally cycled $Ti_{50.1}Ni_{49.9}$ SMA at 150 MPa (Adapted from [143], with permission from Elsevier).

4.1.5 R-Phase Transformation

R-phase is a intermediate phase that is present in NiTi SMAs with certain processing history and compositions [144]. In a normal solution treated nearly equiatomic NiTi SMAs, the material goes from the B2-structured austenite(A) to the B19'-structured martensite phase. Yet, under the presence of crystallographic defects (such as dislocation networks and Ni_4Ti_3 precipitates), an intermediate step from B2-structured austenite to rhombohedral R-phase can be observed before B19' martensite phase is formed.

The transformation temperature, stress-strain and resistance-temperature relationship of R-phase is shown in Figure 4.10. In Figure 4.10 (a), the DSC measurements shows that the transformation peak from austenite to R-phase (R←A) which has very little hysteresis. In 4.10 (b), the stress-strain relationship is different than what occurs with B2–B19' transformation. Starting at stage (i), the R-phase material primarily elastically deforms. At stage (ii), the R-phase detwinning process occurs and favorable oriented variants occur [145]. The stress to induce R-phase detwinning is fairly temperature insensitive unlike B19' martensite reorientation [145]. The stages (iii), (iv) and (v) are the elastic loading and unloading of R-phase and the subsequent thermal-induced shape memory effect. Unlike with B19' shape memory effect, the recovered strain depends upon the testing temperature [145]. Lastly, the presence of R-phase results in a sharp increase in the electrical resistance, as shown in Figure 4.10 (c).

For a designer trying to transform between martensite and austenite, the R-phase can be a nuisance. It can completely suppresses the B19' phase and introduces further non-linearity in the resistance and stress measurements, as shown in Figure 4.10 [146].

Yet, there are notable features of R-phase that have led to some designers making R-phase TWSME actuators [147, 144]. There is small hysteresis of only 2-5°C between R⇄A

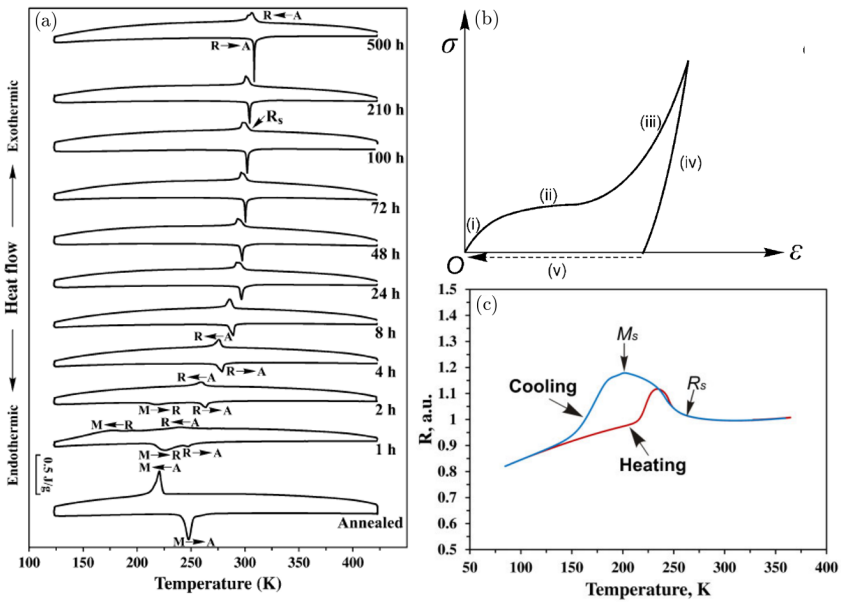

Figure 4.10: Illustration of (a) the effect of annealing time on R-phase presence, (b) stress-strain relationship and (c) resistance-temperature relationship (Reprinted by permission from Springer Customer Service Center GmbH: [146] and reprinted from [145] with permission from SAGE).

[144], R-phase recovery stress and transformation temperature can be controlled by the aging time [146], R-phase has excellent thermomechanical stability and better functional fatigue characteristics than B19' martensite during thermal cycling [145], but R-phase can obtain only 1% strain [144]. These features can be useful for designers looking to create a stable actuator at the expense of strain.

4.2 Application Considerations

For a designer to properly implement SMAs, it is required to consider which material to use, the configuration of the SMA, and to understand strategies to mitigate the limitations of SMAs (e.g. force output, bandwidth and fatigue life). SMAs unlike piezoelectrics and magnetostrictives offer extremely affordable low-force and low-bandwidth actuation solutions because of their simple designs. Unfortunately, most implementation of SMAs are sparse and ad-hoc due to the challenges represented by their microstructural complexities and thermomechanical properties [148].

4.2.1 Material Selection

In the selection of SMAs, the material selection relies upon the requirements of the design (force, stroke and operating temperature), cycle life, hysteresis and/or cost [149].

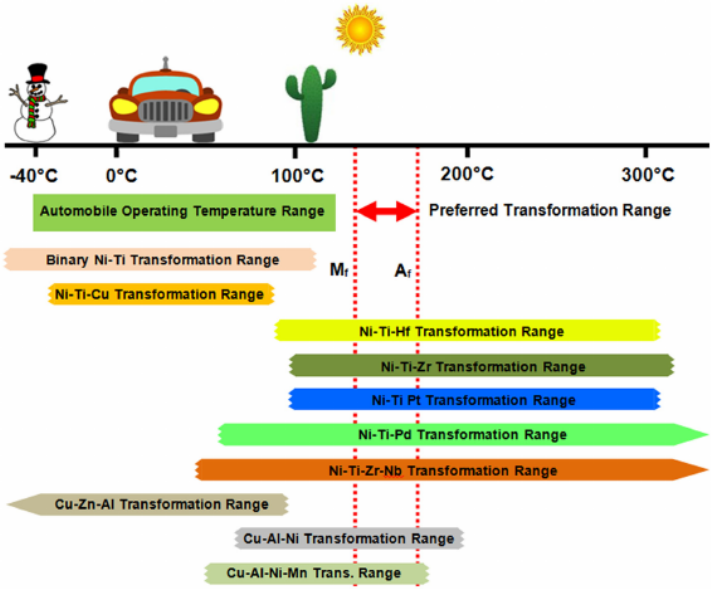

Figure 4.11: Temperature range of different SMA compositions. Automotive preferred temperature range denoted (Reprinted from [149] with permission from SAGE).

Table 4.1: Major SMAs systems and their advantages [151].

Process Factors	NiTi	Cu-based	Fe-based
Maximum Recoverable Strain	8 %	5 %	$\leq$5 %
Cost	High	Low	Low
SME	High	Moderate	Low
Workability	Moderate	Low	Good
Fabrication	Low	Good	Moderate
Processing	Demanding	Easy	Easy

Binary NiTi SMAs are commercially favored due to their high stress, high strain and high cycle life but are limited by the operating temperature and cost, see Figure 4.11 and Table 4.1. Copper based alloys have had been implemented in clamps and fire detector applications [149]. The copper alloys are used for low-cost actuator designs but have limited cycle life ($\geq 10^5$) [150] and are thermomechanically instable [130]. Fe-based SMAs alloys have good workability and ease of production but require large production rates and low recovery applications, such as pipe couplings. Although these Cu and Fe based alloys have been touted as potential replacements for NiTi because of their properties, see Table 4.1, they are still not commercially developed enough [151]. Due to the lack of large-scale commercial implementation of other SMAs, NiTi-based alloys are the suggested material, some material properties are shown in Table 4.2.

Table 4.2: Thermal and Mechanical Properties for NiTi

	Properties	Ref
Mechanical Properties		
Standard Wire Sizes (μm)	20–510	[152, 132]
Max Force Output (grams)	5–3560	[152, 132]
Maximum Recovery Stress (MPa)	500–900	[153]
Normal Working Stress (MPa)	100–150	[152, 132]
Fatigue Strength for N=10^6 (MPa)	350	[153]
Max Transformation Strain (%)		
N* = 1	6–8	
N* < 10^2	6–8	
N* < 10^5	2–4	
N* < 10^7	0.5	
Martensite Young's Modulus (GPa)	28–41	[130]
Austenite Young's Modulus (GPa)	75–83	[130]
Density (kg/m^3)	6400–6500	[132, 130]
Corrosion Resistance	Similar to 300 series SS or Ti-alloy	[130]
Thermal Properties		
Stress-free A_f Temperature Range ($^\circ C$)	-60–110	[154, 132]
M–A Hysteresis ($^\circ C$)	38–41	[139]

*- N is number of cycles

4.2.2 Actuator Configuration

SMAs actuators can be separated by the actuator configuration: the single-direction, bias-force and antagonistic actuator configuration. In each of these configurations, the stress-strain-temperature response changes depending upon the orientation, causing change in convective coefficient [155], and the configuration of the system.

4.2.2.1 Single-Direction Actuators

The single-direction actuator can be used in two different methods: free recovery or constrained recovery. Free recovery actuators have a stress applied and released before heating which causes shape recovery, see Figure 4.12 (a). Constrained recovery actuators have constant strain and generate force upon heating as shown in Figure 4.12 (b). These configurations are generally used for single-action or low-cycle applications . Some of the commercial single-direction actuators are the Cyrofit and the Frangibolt. A recent study showed that constrained recovery can lead to significant reduction in fatigue life ($< 2 \cdot 10^5$) [156].

4.2.2.2 Bias-Force and Antagonistic Actuators

For multiple actuation cycles, the actuator must be able to perform the stroke and return back to the original position. This is achieved in two different methods. For TWSME SMAs, the actuator can operate between two different positions. For OWSME SMAs, the

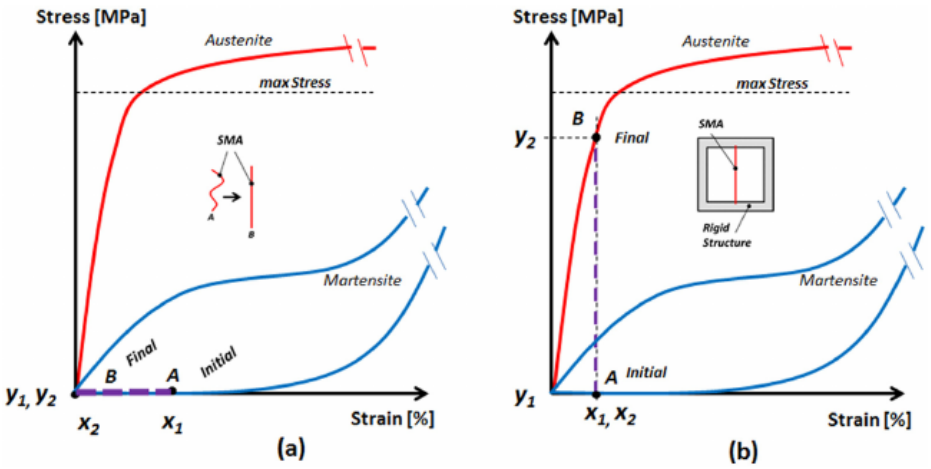

Figure 4.12: Stress-strain relationship of the single-direction actuator design with (a) free recovery and (b) constrained recovery (Reprinted from [149] with permission from SAGE).

actuator requires a resetting force to provide deformation. The most common designs use a bias spring, a weight, or another SMA in antagonistic orientation. Each of these methods introduces different stress-strain responses.

SMA actuators with a bias force are initially deformed as seen in Figure 4.13 point A. This initial deformation x_2 has a corresponding stress y_1. When the actuator is heated up past its austenite finish temperature (point B), it recovers strain and ends up at stain x_1 with a change of stress y_2, due to the expansion of the spring. The maximum possible stress that this design can achieve is the difference between Point A and the elastic limit of austenite.

During the bias spring configuration, the force applied linearly varies with the spring constant. Whereas the deadweight configuration, the force is constant and therefore deadweight configurations has a simpler fatigue behavior. Even though the fatigue behavior of the deadweight configuration is simpler, most actuator designs utilize springs due to the design simplicity, size reduction and weight reduction [149].

In the antagonistic design, two actuators are alternately heated and cooled to provide motion in both directions, see Figure 4.14. The advantage of the antagonistic design is that it acts in both directions, it has possibly better bandwidth than other configurations [149] and reduced hysteresis [157]. As well, there is a three times improvement in the bandwidth by operating the antagonistic actuator in partial transformation [157]. Antagonistic designs have been used as active endoscopes, servos and automotive flaps [149].

4.2.3 Energy Efficiency

SMAs have very low energy efficiency. SMAs have a theoretical energy efficiency of 10–15% [158] but a practical efficiency found to be closer to 1% [159]. Furthermore, the energy efficiency of SMAs is dependent upon the loading configuration, see Table 4.3, where the optimal loading configuration is in tension.

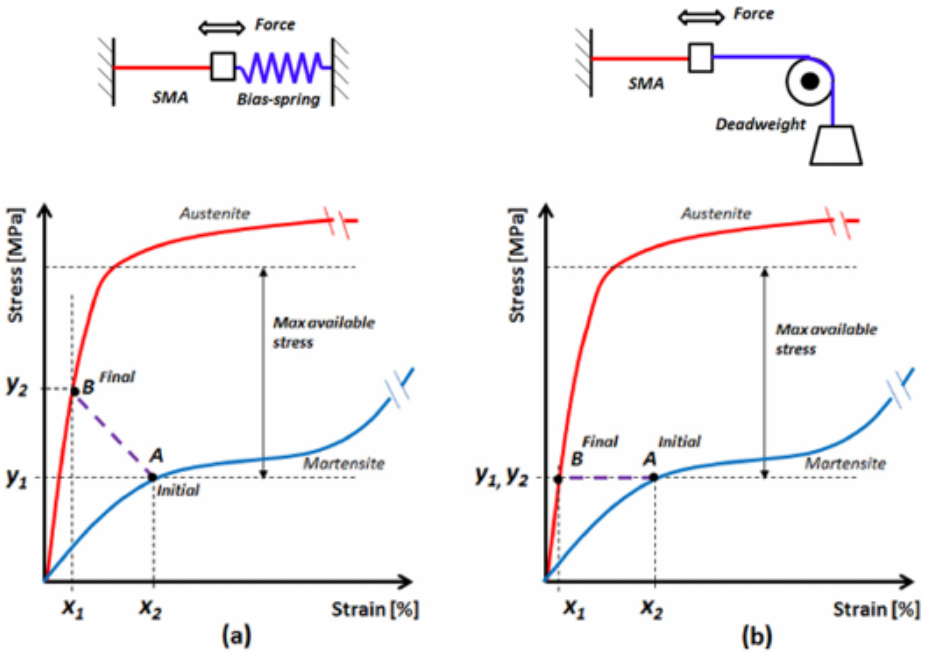

Figure 4.13: Stress-strain relationship of the bias-force actuator design with (a) bias spring and (b) deadweight (Reprinted from [149] with permission from SAGE).

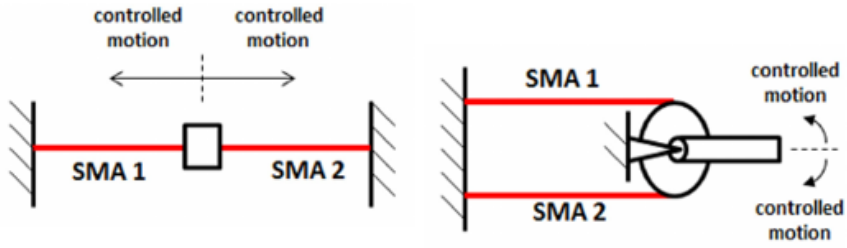

Figure 4.14: Antagonistic designs for (a) linear and (b) rotary motion (Reprinted from [149] with permission from SAGE).

Table 4.3: Comparison of Loading Configuration of SMA Actuators [160].

Loading Configuration	Efficiency(%)	Energy Density (J/kg)
Tension	1.3	446
Torsion	0.23	82
Bending	0.013	4.6

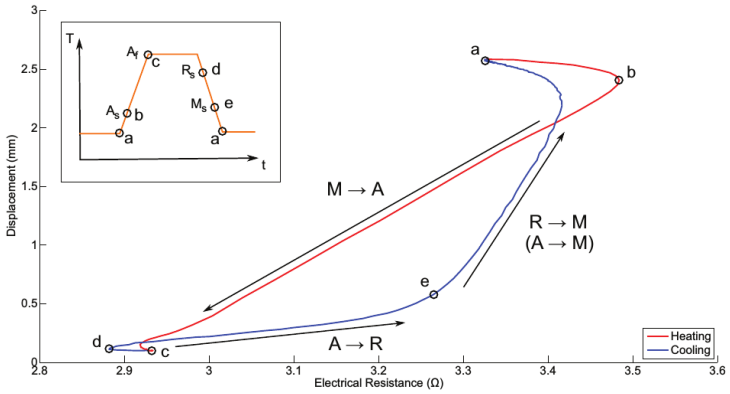

Figure 4.15: Major hysteresis loop behavior of heating and cooling resistance-displacement curve. The inset represents an approximation of the wire temperature over time (Reprinted from [161] with permission from SAGE).

4.2.4 SMA Position Control

The position control of NiTi SMAs has remained a challenging research topic. Many SMA systems use open-loop control in an on–off configuration to avoid the complex thermomechanical properties that are present. While this method works for systems that only have two positions, other systems require more control to compensate for perturbations that occur from environment and external forces [161]. Thus, the requirement for more than two positions requires a closed-loop control system.

Most SMA control algorithms require feedback from a position sensor[162, 163]. But, the use of a position sensor in a SMA actuator system increases the mass, volume and system complexity — causing a detrimental impact upon the factors that generally drives SMA selection [161]. Even though feed-forward control can provide a position prediction, it does not provide precision without some sort of position feedback [161].

Thus, researchers and industry have tried to solve the problem of SMA position control by using SMA self-sensing. Since SMA strain and microstructure changes through actuation, SMA designer have utilized resistance to estimate the strain. Yet, resistance relationship in SMAs is not only dependent upon resistance but stress, temperature and phase fraction [164]. Furthermore, the presence of R-phase which has a high resistivity can introduce non-linearity and resistance hysteresis [161], see Figure 4.15.

There have been many approaches to resolve the SMA self-sensing issue. Some methods involve a set of transformation and mechanical measurements to estimate position [164], curve-fitting of the nonlinear resistance-strain relationship [165] and using only linear portions of complex resistance-strain relationship of a SMA actuator [161]. Others have accepted ≈30% variation between calculations and modeling (see Figure 11 [166]) and deemed it acceptable [167]. In study of SE resistance measurements by Bertolino et al., it was suggested that even in the simplest of conditions, which was a single crystal CuZnAl with uniaxial applied loads, the direct use of resistance measurements for precise positioning is arguable unless quasi-static conditions are assumed, and if the material has high hysteresis (such as NiTi alloys) or complex dynamic conditions the role of temperature

can be deleterious [167]. Furthermore, as indicated by Dynalloy, the makers of Flexinol, precise control may not be feasible due to the variation in the heat loss of the actuator which is dependent upon the convective coefficient [132]. Lastly, the exact relationship between resistance evolution with cycles is not exactly certain and may introduce further complexity in the resistance measurements.

Out of all the approaches, it is my opinion that the best approach is dual resistance measurement technique by Gurley et al. With only the initial length of the actuator and the position of the two resistance measurement points, it had a root-mean-square error (RMSE) of 0.4% and root-mean-square deviation of 1.88% and the test setup was not in an enclosure (indicating lack of control of the convective coefficient) [168]. In other cases surveyed, the RMSE was higher with more information and curve fitting [165] or they do not indicate the RMSE [166, 164]. The issues with this method is that thermal cycling may cause errors in the length calculations as the materials stretch.

4.2.5 Power Output Limitations

Increasing the power output of SMAs is difficult as it is a compromise between higher power output and reduced cycle life. Power output can be increased by having a higher stress and strain on the wire or by increasing the wire diameter. Yet both these strategies have adverse effects to cycle life in much different manners.

By increasing the stress, the wire exhibits one ancillary benefit aside from increasing the power output. As stress increases, the temperature for transition increases since it takes more thermal energy to overcome the strain imposed on the structure. This means that the cooling cycle should be faster since the difference between ambient and wire temperature is greater. The improvement in frequency by increasing stress is 1.2:1 but experimental validation of this concept though seems to show very little cycle time improvement for bias-force actuators [169, 157]. It does seem to be advantageous for antagonistic actuators [157]. Unfortunately, the increased stress also causes increased plastic buildup in the structure resulting in decreased cycle life [143].

Increasing the wire diameter of SMAs allows for higher power output but at the expense of cycle life and frequency. As a NiTi wire gets larger, there is an increase in the size of inclusions and defects which acts as stress risers and crack initiation sites for fatigue cracks [133]. As shown in a study by Norwich and Fasching, the increase from 0.010” to 0.030” wire diameter results in a 80,000 cycle survival rate reduction from 96 to 35% (test performed at 0.8% strain for SE phenomena) [133]. It is posited that the smaller diameter wires are subject to more wire drawing steps which in turn breaks up strings of inclusions [170]. Since large, blocky inclusions are more likely to initiate a fatigue crack, the wire drawing process improves fatigue life by reducing inclusion size [133]. Secondly, even though the wire diameter increases power density, it reduces the surface area to volume ratio which increases the cooling time. For example, the force output for a 0.010” and 0.020” diameter high-temperature Flexinol wire increase from 8.74 to 34.9 N but at the cost of increased cooling time of 4.5 to 14 seconds [132]. The resulting ratio (Force/Cooling Time), which

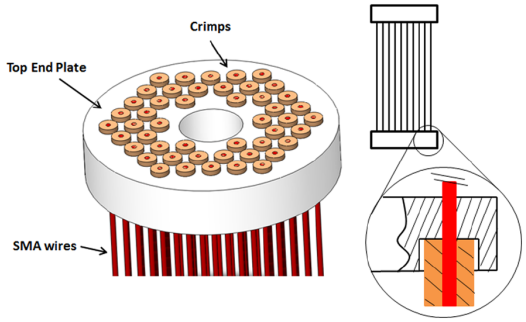

Figure 4.16: Arrangement of SMA wires on end plate (Reprinted from [149] with permission from SAGE).

affects power density, changes from 1.94 to 2.49 which indicates that the power density increase but at the resulting reduction in cycle frequency and life may invalidate the option.

The only two approaches that do not reduce cycle life and cycle frequency — both of which are a concern in SMA applications — is to create a parallel SMA design and improving the cooling times through active and passive cooling.

4.2.5.1 Parallel Designs

In parallel SMA design, multiple small SMA wires are used, see Figure 4.16. The mechanically parallel wires are in electrically in series and must be separated to ensure proper cooling. This arrangement is required to remove the voltage restrictions on the power supply. Even with this setup, it can be difficult to ensure consistent stress distributions in the wires [149]. As well, the number of wires will increase the power requirements of the design [171]. Therefore, the utilization of the bundled SMAs comes at the cost of energy efficiency, design simplicity, cost, volumetric and specific energy and power density.

4.2.5.2 Cooling Time Reduction

One of the most prominent limitation for SMAs is the low bandwidth of the actuator. The methods to improve this are decreasing wire diameter and thermal mass, select a material that can operate at higher temperatures, forced air, heat sinks, increasing stress(increasing transformation temperature), and liquid coolants [132]. Table 4.4 shown an overview of the improvement of speed obtained by these solutions.

Most of these cooling solutions impact upon other performance metrics [149]. As discussed, increased stress can improve the cooling performance but it affects the fatigue life of the wire. High temperature wires, using precious metals, are quite expensive in comparison to NiTi [172, 130]. Heat sinks, forced air, oil immersion, and water with glycol increase the design complexity and actuator specific and volumetric density [149]. Conductive grease in a shell, called lagging media, is probably one of the more promising method [130] due to it being low-cost and a passive system [173], but it affects the specific and volumetric

Table 4.4: Relative Effects of SMA Cooling Methods [132].

	Improvement in Speed
Increasing Stress	1.2:1
Using High Temperature Wire	2:1
Using Solid Heat Sink Materials	2:1
Forced Air	4:1
Heat Conductive Grease	10:1
Oil Immersion	25:1
Water with Glycol	100:1

* - Improvements are not accumulative on the same basis when used together.

density and reduces the already low energy efficiency of SMAs. For a further review, it is suggested to read Jani et al. discussion on design of SMAs [130].

4.2.6 Factors affecting Fatigue Life

SMAs have a relatively low fatigue life in comparison to other electromechanical transducer materials. Plenty of research has been performed to identify techniques to improve the fatigue behavior of SMAs. Fatigue in SMAs can be categorized as structural fatigue and functional fatigue [156]. Structural fatigue is the conventional fracture that occurs from defect accumulation, crack initiation and propagation [141]. Functional fatigue is the residual strain buildup that results in change of transformation temperatures, wire length, recovery strain and recovery stress [156, 141]. To properly utilize the actuator for high-cycle applications, one needs to understand how the configuration and other factors impact the structural and functional fatigue [156].

There are many different strategies to improve the fatigue life of SMAs. The important factors that will be discussed are related to alloy composition and stress-strain-temperature operating regime [141].

4.2.6.1 Alloy Composition

Through the adjustment of alloy composition, better fatigue life in ternary compositions of NiTi, such as NiTiCu [141] and NiTiPd [143], was obtained. Recently, a theory suggest that the thermal hysteresis is an important measure of why certain compositions have better fatigue behavior [174]. The thermal hysteresis is a measurement of the energy lost to lattice friction during transformation [143]. The reduction of thermal hysteresis occurs by improving the crystallographic compatibility of the martensite and austenite, thus requiring less energy lost during transformation [174]. Furthermore, the hysteresis is a measurement of the dissipated work that goes into the creation of structural defects and subsequent crack initiation [175]. Therefore, the smaller the hysteresis width the longer the fatigue life of the actuator [143].

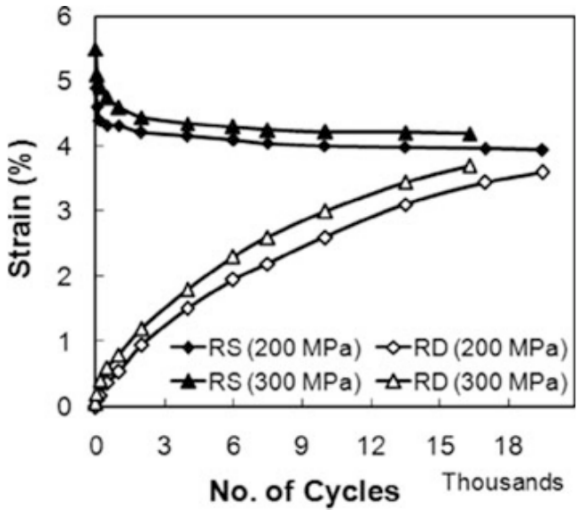

Figure 4.17: Strain and number of cycle relationship for thermomechanical cycles of NiTi SMA wire at 200 and 300 MPa and annealed at 450°C for 15 min. RD indicates residual plastic deformation and RS indicates recovery strain (Reprinted by permission from Springer Customer Service Centre GmbH: [177]).

Separately, any surface defects (drawing defects and die marks) will result in a shorter fatigue life. In a study to determine the effect of NiTi purity on the fatigue performance of the material, the findings indicated that if there is any surface defects then the fatigue crack will initiate there regardless of the oxygen and carbide content [176].

4.2.6.2 Stress-Strain-Temperature Regime

The fatigue properties are dependent upon the stress-strain-temperature operating regime that is present. Each of these have varying degrees of impact upon the fatigue life properties of the SMA.

Although the NiTi SMAs exhibit high stress (600 MPa) and strain (6%) [177], the suggested stress and strain is lower. Dynalloy, the maker of Flexinol, suggest not to exceed 172 MPa, the maximum safe stress of the wire, and 4–5% strain [132]. One author suggests ranges for NiTi SMAs are 200–300 MPa and 2–4% strain [177]. Overall increased stress and strain decrease fatigue life and the suggested operation range is dependent upon many factors including thermomechanical history, composition, energy output and so on.

Stress level does have an impact upon the functional fatigue of the actuator, as shown in Figure 4.17. The reason for the increased residual strain is that the plastic strain buildup increases with increased levels of stress [135].

In comparison, the recovered strain (RS) has a greater impact upon the fatigue life of the SMA, see Figure 4.18. At 200 MPa at 4 % RS, the wire has a fatigue life of about 17,000 cycles, whereas at 200 MPa and 2 % RS the fatigue life is higher (44,000 cycles) [177]. Furthermore, the residual plastic deformation (RD) increases with increased RS.

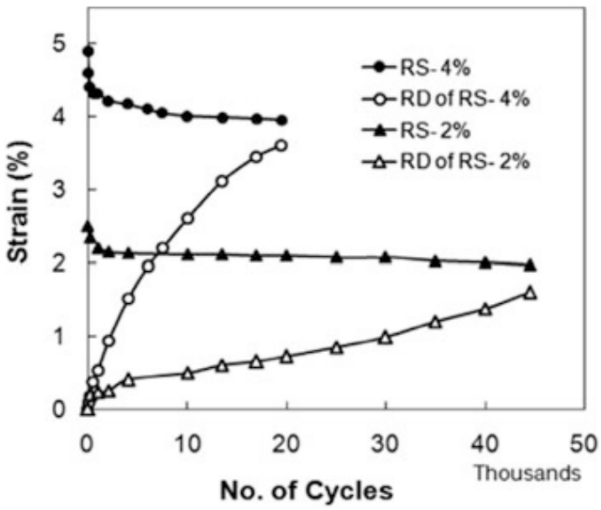

Figure 4.18: Strain and number of cycles relations for thermomechanical cycles of NiTi SMA wire at 200 MPa with 2 and 4 % recovered strain. The wire was annealed at 450° C for 15 min (Reprinted by permission from Springer Customer Service Centre GmbH: [177]).

Although stress and RS have quite a notable impact to impact life, the most damaging factor is heating above the austenite finish temperature, see Figure 4.19. It can be seen that the fatigue life is severely impacted by the maximum temperature experienced by the wire. At a maximum temperature of $A_f + 10°C$ the fatigue life is 18,000 cycles compared to the fatigue life of 5000 cycles at $A_f + 40°C$. The RD can be seen to be more sensitive to the maximum temperature than the RS, which is indicative of the increased defect creation.

Lastly, the type of transformation that occurs has an impact on the fatigue life. For the same amount of RS, the thermomechanical cycle from martensite to martensite and austenite M↔M+A has a much higher fatigue life than the cycle of M+A↔A or M↔A [141]. The reason is that for NiTi SMAs the damage accumulation and crack propagation occurs at different rates depending upon if martensite or austenite phases are present, where austenite is more prone to damage than martensite [177]. Furthermore, it is suggested that the lower temperature range for M↔M+A allows for slower growth of RD [141].

4.3 Summary and Comments

Shape memory alloys are complex transduction phenomenon that is completely different than piezoelectrics and magnetostrictives. The simplest way to describe SMA transduction process is that by heating and cooling the material causes shape change. In further detail, this shape change occurs by a small rearrangement of the microstructure that is nearly reversible at certain temperatures. These transition temperatures can be changed by strain energy present in the microstructure, composition, precipitates, grain size and thermomechanical history. As the number of cycles increase, the material exhibits permanent strain buildup that imposes strain energy on the microstructure that further affects

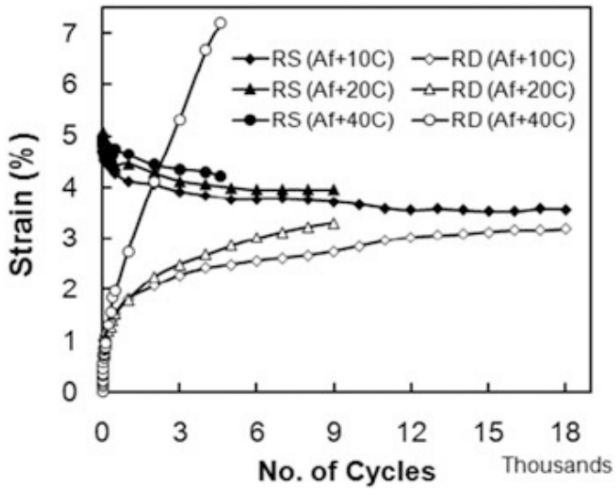

Figure 4.19: Strain and number of cycles showing fatigue life as a function of maximum temperature of the wire which is at stress of 200 MPa (Reprinted by permission from Springer Customer Service Centre GmbH: [177]).

the transition temperature and the speed of strain buildup. Over large number of cycles, the material will structurally fail, by crack initiation and growth, or functionally fail, by changing of thermal or mechanical properties.

SMA actuators have had interest of the aerospace and automotive field because of their simplicity of design, volume and space efficiency. For these designers, the consideration of ternary alloys allows for tailor made materials that have improved fatigue life, higher transformation temperatures which can operate at higher power output than binary NiTi. One issue with binary NiTi, is that the force and stroke output (or power output) affects cycle life. Implementation of secondary systems or a parallel design can improve power output but it negatively impacts the attractive qualities of SMAs. Furthermore, the accurate positioning of self-sensing SMAs is limited by the transient nature of dynamic operation and the complex resistance relationship of NiTi SMAs. For these reasons, SMA actuator implementation has been sparse and fraught with limited viable products [130].

In this chapter, the SMA phenomena has been discussed with an application perspective. Designers considering SMAs should understand that SMAs are limited in size, cycle life and cycle frequency. Some solutions to mitigate these on-going issues of SMAs have been suggested.

Chapter 5

Selection Methods and Performance Criteria

Tools, metrics and performance criteria are created to assist the user in making a qualified decision through a simplified outlook. For example, most designers know when they should use steel, aluminum or cast iron. Each material is quantitatively better when viewed in a certain objective perspective: fatigue life, strength-to-weight ratio and vibration attenuation. These perspectives reduce the number of comparisons needed between material properties and allow for an objective decision of which material has better qualities for the application. It is with this approach that designers come to an effective decision regarding material selection in mechanical design.

In a similar vein, researchers have created metrics that allow for a simplified approach to assessing which active material is better suited for different applications. The approach is very similar to the material selection in mechanical design. These materials are viewed in certain contexts (e.g. efficiency, power density) so that a decision can be formed on which material is better. These decisions are based on certain quantitative measures, or figures of merit. These figures of merit are the justification of why some materials are better.

However, some of these active materials that have excellent figures of merit do not seem to be successfully implemented. While it is possible that these companies and materials are not fortunate, it is also possible that this approach does not accurately translate the complex comparative decisions that are required to determine what is effective. If this approach does not provide an effective solution then the question is whether the problem exists because of the metrics used or the manner in which the optimal is determined.

Therefore, it is necessary to analyze how mechanical material selection method determines what is an optimal material and what assumptions are underpinning the use of these metrics to determine the optimal. As these materials are used in applications, it is necessary to analyze the problem from the application perspective and discuss the assumptions created by those metrics. Throughout this analysis, it will become clear that the simplified material metric comparison is the crux of the criticism. As Goodhart's Law suggests, "[w]hen a measure becomes a target, it ceases to be a good measure" [178]. Therefore, the chapter is capped by an analysis of alternative material selection methods.

Table 5.1: Functions, Objectives and Constraints [179].

Function	"What does the component do?"
Objective	"What is to be maximized or minimized?"
Constraints*	"What non-negotiable conditions must be met?"
	"What negotiable but desirable conditions must be met?"

* It can be useful to distinguish between "soft" and "hard" constraints.

5.1 Selection of Materials

In non-critical mechanical designs, the processes of selecting material is fairly simple. Selection is done through the comparison of single values: strength, weight, cost, vibration attenuation. But this informal process rarely obtains the optimal material. Rather, it is likely to obtain a satisfactory material which is known to the designer. In critical components, the process is more exacting. The selection of the optimal material generally involves multiple competing objectives and a series of constraints that render the informal selection process inadequate.

The formal material selection process that was defined by Michael Ashby is based on utilizing the functions and constraints of the design to meet the objectives, for a description of these terms look at Table 5.1 [179]. Most engineering designs perform multiple *functions*, such as support a load or transfer heat. In the process of designing, the designer has a certain *objectives*: cost, weight, or performance. This objective must be meet through some *constraints* of the design: geometric, force output, working conditions, and so on. These requirements form the selection criteria that reduces the number of material choices and provides a method to quantitatively indicate which of the remaining material is better suited.

Thus, the performance of the material is based upon a measurable *performance metric*, P_j, which depends on a set of *control variables*, x_i [179]. These control variables are the dimensional, mechanical, thermal and electrical requirements of the design as well as the material properties of the design. The performance is defined in terms of the control variables by one of the objectives functions. These objectives function is an equation that describes a performance metric P in such a way that it is inversely related to its value, so it is to be minimized. Equation 5.1 show the base form of the objective functions.

$$P_j = f_j[(Loads, F), (Geometry, G), (Material, M)] \tag{5.1}$$

As an example of the performance metric, assume we have a plate that is in bending, see Figure 5.1, with the objective of minimizing mass [179]. Therefore, the objective function to minimize mass can be defined.

$$m = \ell b t \rho \tag{5.2}$$

where ρ is the density of the material. Assume that the length ℓ, width b, and force per unit width F are specified, and only thickness t can vary. If thickness is reduced, then

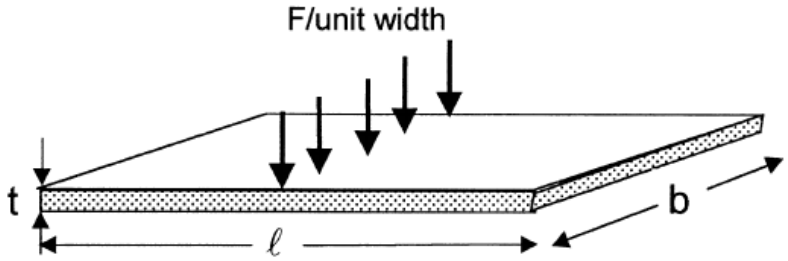

Figure 5.1: A panel of length ℓ, width b, and thickness t, loaded in bending by a force F per unit width (Reprinted from [179], with permission from Elsevier).

the objective will be minimized, but the plate also has a stiffness constraint S, which is the amount of deflection δ under the load Fb.

$$S = \frac{Fb}{\delta} = \frac{C_1 EI}{\ell^3} \geq S^* \tag{5.3}$$

where S^* is the desired stiffness which is a function of the load distribution constant C_1, Young's modulus E, and the second moment of inertia of a section, which is defined as follows.

$$I = \frac{bt^3}{12} \tag{5.4}$$

Using Equation 5.3 and 5.4, to remove thickness t and substituting into Equation 5.2 gives the following performance metric.

$$m = \left(\frac{12S^*b^2}{C_1}\right)^{1/3} \ell^2 \left(\frac{\rho}{E^{1/3}}\right) \tag{5.5}$$

As shown in Equation 5.5, the extrinsic design-dependent quantities are separated from the intrinsic material-dependent properties, which are found in the last parentheses. Therefore, the optimal design will be the one which optimizes those material properties.

The benefit of this approach to material selection is it allows for a separation of the extrinsic properties, the load- and geometry-dependent parameters, and optimizes the intrinsic properties, the material-dependent parameters. As the optimum design will require the optimum material selection, it is needed to be optimized.

5.1.1 Active Material Performance Criteria

When applying the same selection methodology to active materials, there are difficulties. The intrinsic material coefficients that relate to the transfer of energy comes from the constitutive equations, and the constitutive equations are domain dependent. Since one

Figure 5.2: A generalized model of a transducer with A_1 and T_1 are the input across and through variables, and A_2 and T_2 are the output across and through variables

can not quantitatively compare different material coefficients, generalized assessment based on performance requires generalized coefficients that allow for comparison.

A simple generalized coefficient that is employed by all transducer designers is to look at efficiency of the design [180]. Efficiency is viewed as an essential part of a good transducer. The standard definition of efficiency is $\eta = P_{out}/P_{in}$ where P_{out} is the power delivered and P_{in} is the input power. Another equivalent definition refers to a momentary efficiency $\eta = U_{out}/U_{in}$ where U is the energy given per cycle.

Yet the coefficient used for active material comparison is not the previously defined efficiency, it is a term called coupling coefficient which relates to efficiency but is intrinsic. It is based upon how well the material couples the mechanical and non-mechanical domains. The coupling coefficient was initially used to evaluate the electromechanical coupling of piezoelectrics [181]. The metric was used to measure the ratio of energy that was transfered from the electrical–mechanical domains for piezoelectrics. Later, it was employed for the coupling of other transducers, such as electromagnetic and magnetostrictive. The coupling coefficient, which can be expressed as $k^2 = U_{stored}/U_{in}$, indicates the ratio of energy stored at the output, U_{stored} port with no external load, and the total input energy, U_{in} [180]. Basically, the difference between the coupling coefficient and efficiency is that one represents intrinsic material properties and efficiency represents the ratio of energy flowing between the output and input ports.

The generalized coupling coefficient can be simply defined. Assume a linear two-port transducer, reproduced in Figure 5.2, the matrix form of the generalized constitutive equations are as follows.

$$\begin{bmatrix} A_1 \\ A_2 \end{bmatrix} = \begin{bmatrix} q_{11} & q_{12} \\ q_{21} & q_{22} \end{bmatrix} \begin{bmatrix} T_1 \\ T_2 \end{bmatrix} \tag{5.6}$$

The coupling coefficient then is defined as Equation 5.7. The derivation can be found in the works of Bechmann [181]. Note how the coupling coefficient is a solely intrinsic parameter, relating only to the coefficients of the generalized constitutive equations.

$$k^2 = \frac{q_{12}^2}{q_{11}q_{22}} \tag{5.7}$$

The coupling coefficient is widely adopted and became a metric that is published by manufacturers. The benefit of the metric is it allows easy comparisons of different materials, yet one should use caution and not simply compare this value as it can lead to poor

decisions. For example, the coupling coefficient is arguably the essential metric to measure efficiency of an energy harvester material. But, the metric has its limitations as it does not provide any indication of the effect that material stiffness has on the function of the device. Therefore, it is possible that for energy harvesting where the optimal transduction material is the one that converts the most energy is not solely related to the conversion efficiency but the effect the material properties has on the dynamics of the harvester [182].

5.2 Selection of Devices

The formal material selection framework can be adapted to device selection. Since the device defines the function, selection is based on the constraints and performance metrics of the device.

Yet, there is a difference between performance metrics that evaluate the suitability of technology and actualized products [183]. When system designers select devices, their acceptance criteria is not based on whether a technology could be suitable but the ability of the final product (a combination of technology, packaging and controls) to meet the design requirements. In contrast, technology designers and researchers that attempt to apply the emerging technologies to applications are interested in figures of merit that relate the suitability of the technology to the device. Therefore, there is a distinction between the needs of system designers and technology designers.

System designers generally look for manufactured devices that meet their requirements. The purpose of the application of the technology is already known, but their goal is the optimal selection based upon a set of device-based figures of merit. For example, a selection of an actuator would probably involve force, stroke and frequency requirements. The designer is not concerned if magnetostrictive materials are more energy efficient than piezoelectric; this is just a possible objective, such as to minimize mass or maximize energy density [183]. The purpose of the selection process is an attempt to resolve constraints and select the best device based upon their design objectives. In this manner, the approach is similar to the formal material selection process except that it relies upon extrinsic properties.

In comparison to system designers, technology designers solve a different problem. Their goal is either to find the optimal application that uses the beneficial parameters of the technology or the optimal technology for an application. Successful emerging technology designs can be categorized as innovative or disruptive. An innovative emerging technology design introduces a response that was not possible before (e.g. a traveling-wave piezoelectric motor), which is hard to quantify. Other innovative designs are those that are capable of improving constraints that were not possible before, which is measurable. A disruptive design is one that outperforms a manufactured device; more clearly, it outperforms a manufactured device in at least one of the performance metrics, or objectives, such as mass, size and cost. Unlike system designers, these performance metrics are used prior to the realization of a product, and thus they are largely discussed through intrinsic materials properties.

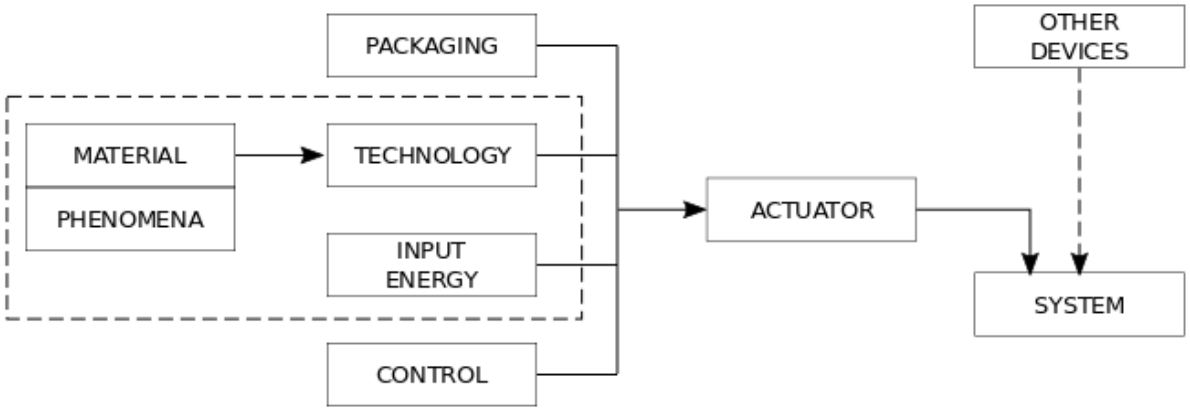

Figure 5.3: Anatomy of an actuator system with a dashed box indicating focus. Based on [183].

Although system and technology designers differ in using extrinsic and intrinsic properties, they both optimize on the same performance criteria. These performance criteria are supposed to define trends in selection. These trends in selection are synonymous with market and technology force. Some of these forces are clear, such as minimization of mass, size and cost. Selection trends in performance are normally not clearly defined and need some explanation.

For actuators and sensors, performance can be broken into the three trends: speed of performance, stability, accuracy [184]. As these figures of merit are time-based and frequency-based metrics, they depend upon a model and will not be covered in this work, see "Sensors and actuators" by Clarence De Silva for a discussion [184]. For energy harvesters, performance is extrinsic energy output, a further argument for energy output is presented in Section 5.2.3.1.

To properly select a device, it is necessary to indicate the device-dependent functions, constraints and performance metrics. Due to the importance these figures of merit have in selecting the proper material, performance metrics will be critiqued. Ultimately, it is determined that material-based figures of merit for actuators are confusing, for sensor there are too few and for energy harvesters figures of merit match perfectly.

5.2.1 Actuators

When integration designers and technology designers describe actuators, there is a discrepancy in their definitions. For an integration designer, all the elements that compose an actuator are discussed, see Figure 5.3, but for a technology designer an actuator is the technology and input energy.

Fundamentally, an actuator is a device that creates useful mechanical work. For it to be called useful mechanical work, the actuator must receive input energy and controllably move a specific distance overcoming specific force requirements within a desired amount

Table 5.2: Overview of Actuator Function, Constraints and Objectives

Function:	Create useful work by receiving input energy and controllably moving a certain distance overcoming a certain force within a desired time

Constraints:	Objectives:	
Stress	Mass	Material
Strain	Size	↓
Bandwidth	Power Consumption	
	Performance	
	Cost	Product

of time [183]. Therefore, the *function* of the actuator is to create useful work by receiving input energy and controllably moving a specific distance overcoming a specific force within a desired time. This function defines the *fundamental constraints* of an actuator: the required force and stroke within a certain time.

The common design objectives of an integration designer are a mixture of intrinsic and extrinsic properties. The designer *objectives* (organized from intrinsic to extrinsic) are mass, size, power consumption (includes auxiliary environmental and control systems), performance (includes control performance parameters), and cost (includes service, auxiliary systems and replacement costs), see Table 5.2. While most technology designers optimize on efficiency, it is not always the design objective. In reality, most systems have an abundance of energy and efficiency is only a secondary objective [183].

5.2.1.1 Figures of Merit

The use of intrinsic figures of merit allow for a mapping of multiple different technologies characteristics into a single metric which can be compared against other constraints or figures of merit. It is used extensively by selection criteria methodologies, academics and industries [185, 186, 10, 183]. The selection criteria methodologies emphasize that the figures of merit are an effective comparative tool for different technologies and it indicates fundamental differences in actuator families [185, 186, 10]. However, the nature of this mapping can result in confusion of the exactly what is being optimized.

The actuator figures of merit shown in Table B.4 indicate effectiveness in designing and are directly or indirectly related to four designer objectives (mass, size, power consumption, and cost).

Energy Density: the measure of energy, or work, per unit volume of mass. It is also called work density. Depending upon the denominator, volume or mass, this should be called volumetric energy density and specific energy density, respectively shown in Equation 5.8 and 5.9.

$$E_V = \frac{F\,s}{V} = \frac{\sigma_{max}\,\epsilon_{max}}{V} = \frac{E_{out}}{V} \tag{5.8}$$

$$E_\rho = \frac{E_{out}}{\rho V} \tag{5.9}$$

where E_V and E_ρ is respectively volumetric and specific energy density, F, s, V, σ_{max}, ϵ_{max}, E_{out} and ρ respectively are force, stroke, volume, maximum stress, maximum strain, output energy and density.

Historically, energy density has been used to indicate space or mass efficiency of energy sources. The earliest usage found with energy density as an actuator figure of merit was related to piezoelectric motors, where the use of piezoelectric motors configuration can increase energy density by a factor of twelve [187]. The purpose of using energy density was to compare different configurations of the same technology, where the limitations of piezoelectrics (low strain) were mitigated by a different configuration.

But, what does energy density indicate in comparison of different technologies? A high energy density indicates that the actuator has a high product of stress and strain (elastic energy) per unit of volume or mass. One productive use of the energy density metric is to indicate that any technology that has higher energy density can be used with the addition of stroke or force amplification mechanisms even if it does not meet the force and stroke constraints [186]. One of the issues of this metric is that it does not consider frequency. Due to this, designs that use energy density should expect long actuation cycle times. The highest energy density actuators, in Figure 5.4, all have a frequency below 10^3 Hz in Figure 5.6.

One glaring error with energy density is that the designer rarely uses it in seclusion. Although SMA have high intrinsic energy density, there are not many articulated cranes that use them or industrial systems that use thermal actuators. The issues created by the metric is that those who want a high energy density are most likely trying to create a system that move a specified loads with less mass or volume. The geometric independence of stress and strain create the illusion that those materials with high values can translate to these systems. Yet, without the consideration of the size limitations, which shape memory alloys are limited to 4.2.5.1, the energy density metric is fairly unsubstantial. Furthermore, shape memory alloys cycle life is reduced by increased loading, see Section 4.2.6. What purpose does energy density serve as a figure of merit if it is predicated on the designer knowledge of the limitations of all the actuators.

Furthermore, energy density calculated from intrinsic material properties can be quite different from packaged products, as shown in Figure 5.5. In some cases packaging is a necessity for performance, such as Terfenol-D actuators. In other cases, bare actuators are possible but the packaging improves the life and environmental stability of the actuator and may be needed. Therefore, the utilization of energy density for an actuator figure of merit has many considerations.

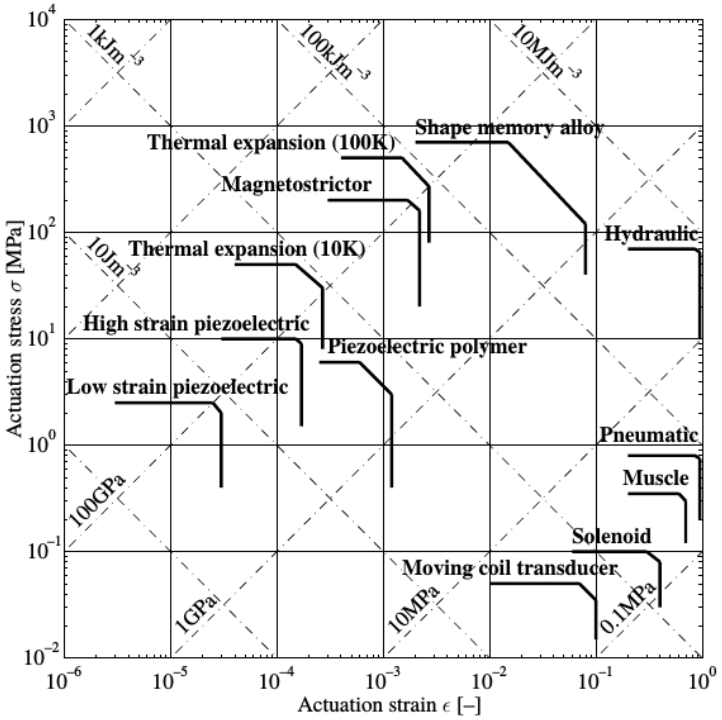

Figure 5.4: Actuation Stress versus actuation strain of various actuator technologies. Heavy lines indicate upper limit of performance. Low-strain piezoelectrics are Quartz (SiO_2), Lithium Niobate ($LiNbO_3$), Lithium Tantalate ($LiTiO_3$) (Reprinted from [185] by permission of the Royal Society).

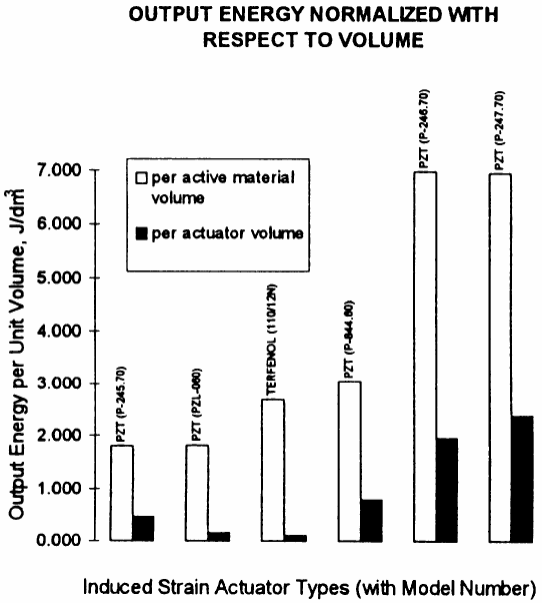

Figure 5.5: Comparison of output energy density per unit volume of 6 induced-strain actuators with casing and prestress mechanism [188].

Table 5.3: Illustration of the loss of information from using power density (inspiration from [191] and data from [185]).

Actuation Type	Max Stress	Max Strain	Max Frequency	Max Power Density
Hydraulic	$20 - 70$	$1 \cdot 10^{-1} - 1 \cdot 10^{0}$	$5 \cdot 10^{1} - 3 \cdot 10^{2}$	$\approx 5 \cdot 10^{8}$
Piezo Polymer	$0.5 - 5$	$2 \cdot 10^{-4} - 1 \cdot 10^{-3}$	$1 \cdot 10^{5} - 1 \cdot 10^{7}$	$\approx 3 \cdot 10^{8}$
Low Strain Piezoelectric*	$1 - 3$	$5 \cdot 10^{-6} - 3 \cdot 10^{-5}$	$5 \cdot 10^{5} - 3 \cdot 10^{7}$	$1 \cdot 10^{8} - 1 \cdot 10^{9}$

* Low-strain piezoelectrics are Quartz, Lithium Niobate, Lithium Tantalate

Power Density: the measure of power per unit volume or mass of certain actuation technology. In this text, the term volumetric power density and specific power density will be used, as respectively shown in Equation 5.10 and 5.11.

$$P_V = \frac{F\, s\, f}{V} = \frac{\sigma_{max}\, \epsilon_{max}\, f}{V} = \frac{P_{out}}{V} \tag{5.10}$$

$$P_\rho = \frac{P_{out}}{\rho\, V} \tag{5.11}$$

where P_V and P_ρ is respectively volumetric and specific power density, P_{out}, F, s, f, V and ρ are output power, force, stroke, frequency, volume and density respectively.

Historically, volumetric power density as an actuator figure of merit was used to discuss improvement of induction motors [189]. The earliest application of power density for active materials indicates that power density was used to compare maximum experimental results within quartz piezoelectrics, or the same family of the technology [190]. Therefore, the historical application of power density does not seem to be to compare different fields of actuation technologies.

However, what does the comparison of power density of different actuation technologies indicate? If power density is high, then the candidate produces more power in a unit of volume or mass. But, power density as a calculation can favor devices that have excessive frequency compared to stress and strain. In Table 5.3, hydraulics, which has high stress and strain, is low power compared to piezoelectrics, which is low stress and strain. Similarly to energy density, the comparison of different actuation technologies through power density reduces fidelity of the information. It begs the question when power density is better than a table of values.

The issue with power density, alongside the inaccuracy between theoretical and actualized actuators density, is that it is more vague than energy density. Power density changes depending on the conditions for continuous operation and whether cooling systems are included. In Huber et al., power density for materials is calculated as continuous operation [185]. Yet, it is not certain whether the power density for piezoelectrics and magnetostrictive materials is calculated with the upper temperature bound being at curie temperature or at the suggested temperature limit of half the curie temperature (see Section 2.3.6 and Section 3.2.4). Furthermore, the indicated values for piezoelectric max stress is a factor of ten lower compared to what PI ceramic suggests (50–75 MPa) [192]. Nor, does power density indicate that some technologies fail quite quickly at high stress and strain, such as

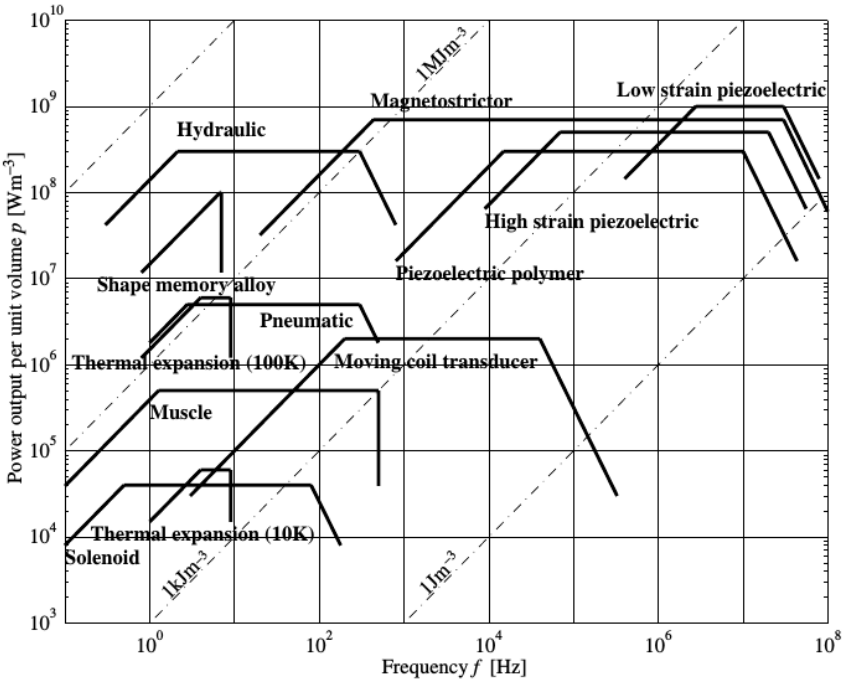

Figure 5.6: Volumetric power versus frequency of various actuator technologies. Lines of slope +1 indicate equal volumetric work output per cycle (Reprinted from [185] by permission of the Royal Society).

SMAs. In most actuation systems, cooling systems can allow for more power output at the cost of increased power consumption [193]. Power density calculations should not include auxiliary systems since it directly impacts the criteria that is optimized, yet then power density does not indicate the limits of the actuator technology.

Energy Efficiency: the conversion of power from input domain to the output domain. In fact, both energy and power density are efficiency metrics relating to energy, power, size and mass but conventional terminology for efficiency is related to the conversion of energy between input and output domains. Equation 5.12 shows the common methods of defining efficiency [194].

$$\eta = \frac{P_{out}}{P_{in}} = \frac{P_{in} - \sum P_{loss}}{P_{in}} = \frac{P_{out}}{P_{out} + \sum P_{loss}} \tag{5.12}$$

where P_{loss} indicates the quantifiable power losses in the system.

Due to the increasing environmental regulations and energy costs, efficiency is lasting market force which is important for some devices. Having high efficiency means reduced power consumption, reduced heat buildup during cyclic operation and lesser operation costs. In high-bandwidth operations, efficiency becomes increasingly important since the energy lost results in an increase in temperature which may increase nonlinearity, reduce cycle life and degrade performance. With high-cycle operations, operation costs becomes

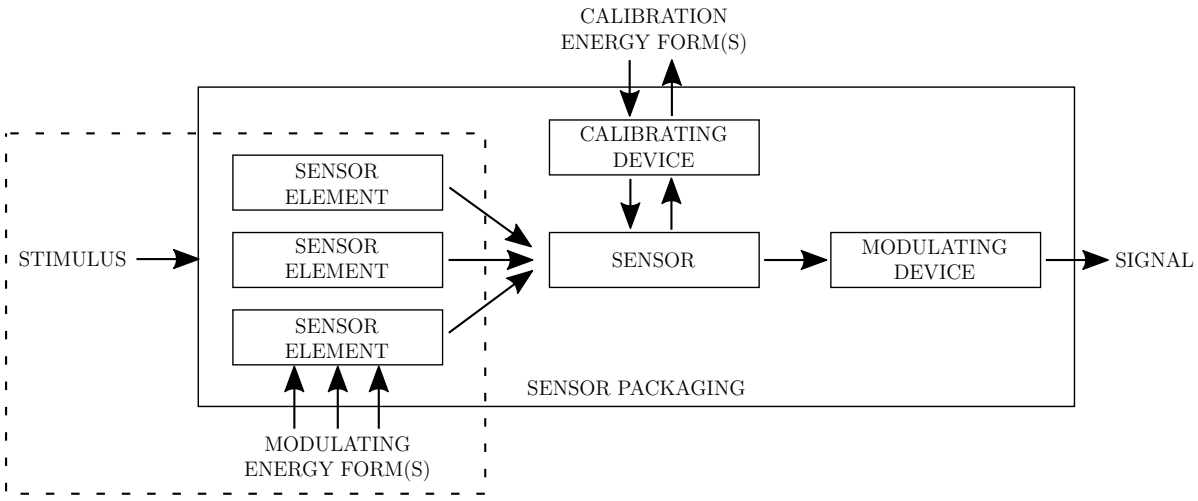

Figure 5.7: Anatomy of a Sensor System. Dashed box indicates scope of work (Adapted with permission from [196]).

significant and a high cycle life ensures less cost. While energy efficiency is important, energy is generally abundant and other figures of merit generally take precedence.

5.2.2 Sensors

The term sensor or transducer has different definitions depending on the technical discipline of the individual and geographical location. The following terminology used to define sensors is in agreement with the *International Vocabulary of Measurement*(VIM) created by the Joint Committee for Guides in Metrology. A sensor is the element that is directly affected by the phenomenon that carries the measurand [195]. The sensor output is converted by the measuring transducer into a useful output that has a specific relationship with the input quantity [195]. In Figure 5.7, these definitions clearly denote what an integration designer and technology designer, dashed box, view as a sensor.

The *function* of a sensor is to make accurate measurements in a desired time. The fundamental *constraints* that define a sensor are its boundaries of operation and accuracy. The boundaries of operation are defined as the measuring interval, resolution, rated operation condition and limited operation condition. Accuracy is defined loosely and includes linearity, hysteresis and the effect of temperature on sensitivity.

The *objectives* of the designer correspond to the market forces. Miniaturization, decreased power consumption, increasing accuracy, increased reliability and decreased cost are all trends in sensor development. These generally can be placed into categories related to mass, size, power consumption, performance characteristics and cost, see Table 5.4. Sensor performance is essentially how integration and technology designers select. Performance figures of merit that are also used by actuators can be found in Table B.4.

Table 5.4: Overview of Sensor Function, Constraints and Objectives

Function:	To make accurate measurements in desired time	
Constraints:	Objectives:	
Operation Boundary	Mass	Material
Accuracy	Size	↓
Bandwidth	Power Consumption	
	Performance	
	Cost	Product

Table 5.5: Sensor Characteristics [196].

Static	Dynamic
Sensitivity	Step Response
Nonlinearity	Operating Range
Hysteresis	Dynamic Error Response
Minimum Detectable Signal	Hysteresis
Threshold	Noise
Selectivity/Specificity	Repeatability
Accuracy	Instability and Drift
Distortion	

5.2.2.1 Figures of Merit

Unlike in actuators, sensor performance metrics, shown in Table 5.5, are largely extrinsic experimental measurements. Thus, it is hard to select based upon material properties as most values are extrinsic and readers are directed to the review by Shieh et al. for an overview of resolution, sensing frequency and range for displacement, accelerometers, force and temperature sensors [197].

The problem with sensor performance metrics is not the metrics used, since the metrics perfectly defines market and technology forces, but the importance that sensitivity has over other results. While sensitivity is an important metric, most manufacturers have accepted that stability is more important [197]. Out of the characteristics, available material data only provides information upon sensitivity and hysteresis, see Table B.4. If the material is operated at resonance, then the mechanical quality factor is important.

Sensitivity: the "quotient of change in an indication of a measurement instrument and the corresponding change in a value of a quantity being measured" [195]. For piezoelectrics and magnetostrictives, the stress coefficient ($g = d/\epsilon$ or $g = d/\mu$) term is generally viewed as an acceptable figure of merit.

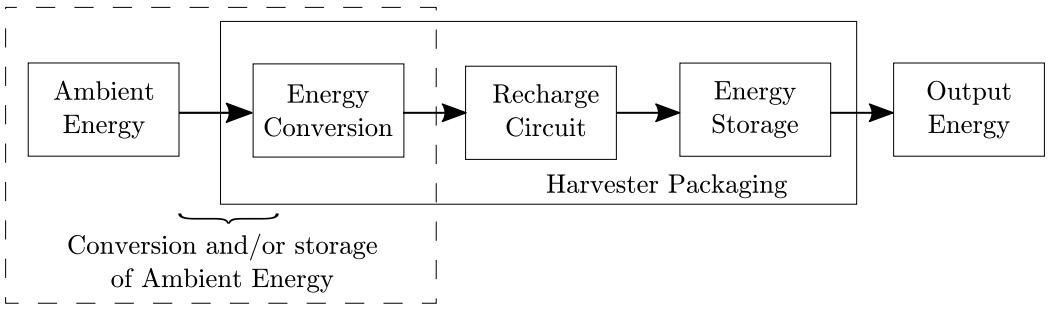

Figure 5.8: Anatomy of Energy Harvesting System. Dashed box indicates scope of work.

5.2.3 Energy Harvesters

The *function* of an energy harvester is to convert ambient energy to electrical energy. Normally, the term energy harvesting is separate from power generation. The separation is related to the scale; energy harvesters are micro devices. The main sources of ambient energy harvesting are light, mechanical, thermal, and radio-frequency (RF). As shown in Figure 5.8, the energy harvester stores or converts instantaneous ambient energy. In the case of storing energy, there needs to be some mechanism (e.g. heat sink or inertial mass) that is able to store the energy while the active material converts the stored energy into electrical energy. The electrical energy is conditioned for the energy storage device, then it is stored. The integration designer is more interested in the usage of the energy harvester as a secondary power source for their system, whereas the technology designer will be focused on optimizing the conversion by material selection and design.

The fundamental *constraints* of an energy harvester is the ambient energy source (including character) and the energy stored. Essentially, an energy harvester is a sensor whose output is conditioned and stored. But, an energy harvester is designed for maximum energy output rather than stability and accuracy. Although actuators are energy or power producing devices, the favorable properties of an actuator(e.g, maximum strain and stress) do not necessarily indicate favorable properties for an energy harvester. Therefore, the optimal selection of material for an energy harvester may not be the same for an actuator or a sensor.

Aside from improving the energy output, the *objectives* of energy harvester (ordered from intrinsic to extrinsic properties) are related to mass, size, lifetime and cost. As the field of energy harvesting is not mature, the academic effort has been on improving power output and minimizing size. In this way, both energy and power density are representative of the technology forces. Furthermore, energy harvesters are a disruptive device to energy storage devices, where the dominant market forces are energy and power density.

Yet, which one is the best figure of merit for energy harvesting?

5.2.3.1 Figures of Merit

Power and energy density commonly are used to indicate performance of energy storage devices. They are the dominant figures of merit used by industry and both provide different

Table 5.6: Overview of Energy Harvester Function, Constraints and Objectives

Function:	To make convert ambient energy to electrical energy.	
Constraints:	Objectives:	
Energy Output	Mass	Material
Ambient Energy	Size	↓
Environment	Lifetime/Reliability	
	Cost	Product

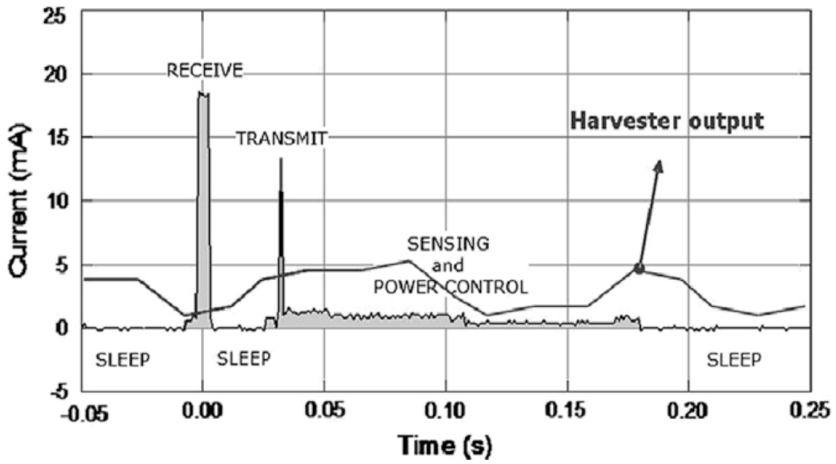

Figure 5.9: A typical power consumption of a sensor node. Due to consumption not matching harvester output, an energy buffer and power management is needed (Reprinted from [198], with permission from Elsevier).

information. Power density indicates the rate of energy release and energy density indicates amount of energy stored. Power and energy density indicate power and capacity abilities of the energy storage device. Yet, the difference between energy storage devices and energy harvesters is that the ability of meeting system power requirements. Energy harvesters provide micro levels of power that are lesser than what is required by the low-power wireless sensor node, see Figure 5.9. Hence, the usage of an energy storage device.

For energy harvesters, power density indicates the instantaneous power that is at the output terminal of the transducer for a cubic centimeter. Energy density indicates the amount of energy that the output terminal delivered over a period of time for a volume or mass. Both metrics indicate that increasing output for a certain volume or mass is optimal. Power density indicates that the optimal energy harvester is obtained at the maximum instantaneous power output. Whereas, energy density indicates that the optimal energy harvester is obtained by maximizing power output over time.

A different classification would be to indicate that power density is an instantaneous optima and energy density is the global optimum of energy output. This does not indicate that power density can not provide a global optimum. If the magnitude and frequency of the ambient energy is constant, optimizing power density results in the global optimum.

If not then optimizing energy density is necessary. Furthermore, power density provides issues related to what power measurement to use. If it is not peak power but RMS power, it is energy density. If it is peak power, it provides little information except that the near-perfect parameters managed to output high power.

The goal of the energy harvester is to provide enough energy for a system. Therefore, the amount of energy extracted per unit volume for some period of time is far more indicative of a performant energy harvester.

5.3 Alternative Selection Methods

The utilization of intrinsic figures of merit was supposed to simplify the optimal material selection process. Yet, the assumptions linked to these figures of merit indicate that sometimes multiple values need to be compromised to get the optimal, that the intrinsic variables belies extrinsic size limitations and that some figures of merit lose fidelity by reducing variables. So, the optimal selection based on figures of merit is all but simple.

This issue can be examined in a different perspective where the question is, what is the best way to simplify the material selection process?

The figures of merit approach reduces the number of coefficients needed to be compared. At the surface this reduction seems useful, but it requires intimate knowledge of the materials to avoid wrong conclusions and is limited by the number of comparisons that the designer is able to compare. Other selection methods simplify the comparative process by ordering of the alternatives by a designer defined preference of criteria. The advantage of the method is that it allows for a complex comparative selection to be obtained.

The figures of merit approach is also called the Ashby's method and is used in a commercial product called the Cambridge Engineering Selector (CES). CES is a combination of an extensive database and the figure of merit approach. Other selection methods are found under the field of Operational Research and use multi-criteria decision making (MCDM) method.

The comparison between Ashby's method and MCDM methods has been covered in literature. While Ashby's method provides accurate results and the figure of merit approach provides insight into the scaling process [199], the method has problems. It does not provide ranking [200, 201], if more than two figures of merit are used it becomes laborious [201] and does not provide any direction for how to select between tangibles (e.g. coupling coefficient) with intangibles (e.g. machinability) [202]. For these reasons, it is not considered as suitable for material selection and will not be used.

The MCDM methods that will be discussed are the Analytic Hierarchy Process (AHP), Technique for Order Preference by Similarity to Ideal Solution (TOPSIS) and Vlsekriterijumska Optimizacija I Kompromisno Resenje (VIKOR), which means Multicriteria Optimization and Compromise Solution.

Table 5.7: The fundamental scale of absolute numbers [202].

Intensity of Importance*	Definition
1	Equal importance
3	Moderate importance
5	Strong importance
7	Very strong importance
9	Extreme importance
Reciprocals of above	If activity i has one of the above non-zero numbers assigned to it when compared with activity j, j has the reciprocal value when compared to i

* - 2, 4, 6, 8, are used as intermediate values between levels of importance

5.3.1 Analytic Hierarchy Process

The AHP is the most popular MCDM method [203]. It is a formalized decision making process comprised of the following steps [202]:

1. Define the problem and what is the goal
2. Create a decision hierarchy with the goal at the top, then outline the objectives in a broad perspective as a second row, create lower levels with criteria that depend upon the objectives, and the lowest level usually contains the alternatives.
3. Create sets of pairwise comparison matrices using linguistic values for preference between elements. Each element in a matrix is used to compare elements in the level below it.
4. Using a quantitative scale for linguistic values, the priorities are obtained through the comparison matrix. These priorities are used to weight the priorities of the level below it. Once all elements are weighted, the global priority can be obtained. Each element in the level below adds its weighted value until the final priorities of the alternatives at the lowest level are found.

To quantify the linguistic comparisons there needs to be a scale of numbers that indicates the level of preference between criteria. The scale commonly used for AHP is shown in Table 5.7.

AHP has been used in many settings to make decisions [202]. A proprietary software called Expert Choice uses AHP and has been used by multiple industries, [204]. The AHP process is better explained with an example and thus it will be shown in Sections 6.2.3.1 and 6.1.2.

5.3.2 Order Preference By Similarity to Ideal Solution

TOPSIS [205] posits that the optimal solution is the alternative that has the shortest distance to positive-ideal solution and the furthest distance from the negative-ideal solution.

In TOPSIS, the attribute in the decision matrix is either monotonically increasing or monotonically decreasing utility. This means that the larger the attribute value, the greater preference for the benefit criteria and the lesser the preference for the cost criteria. Furthermore, any qualitative attributes (such as excellent linearity) will need to converted to a numerical scale through a scaling technique. As the attributes are not of equal importance to the decision maker, this method requires assigned set of weights. The following steps are the steps for utilizing TOPSIS.

1. Create a decision matrix which consists of m alternatives with n attributes, or criteria. The structure is shown below:

$$D = \begin{array}{c} \\ A_1 \\ A_2 \\ \vdots \\ A_i \\ \vdots \\ A_m \end{array} \begin{array}{c} \begin{array}{cccccc} X_1 & X_2 & \dots & X_j & \dots & X_n \end{array} \\ \begin{pmatrix} x_{11} & x_{12} & \dots & x_{1j} & \dots & x_{1n} \\ x_{21} & x_{22} & \dots & x_{2j} & \dots & x_{2n} \\ \vdots & \vdots & & \vdots & & \vdots \\ x_{i1} & x_{i2} & \dots & x_{ij} & \dots & x_{in} \\ \vdots & \vdots & & \vdots & & \vdots \\ x_{m1} & x_{m2} & \dots & x_{mj} & \dots & x_{mn} \end{pmatrix} \end{array}$$

   where A_i indicates the alternative i, where i = 1,2,...,m and x_ij indicates the numerical value for the ith alternative with respect to the jth criteria.

2. Calculate the normalized decision matrix **R** where the normalized value is calculated using vector normalization:

$$r_{ij} = \frac{x_{ij}}{\sqrt{\sum_{i=1}^{m} x_{ij}^2}} \tag{5.13}$$

   Normalization allows for each attribute to have the same unit length of vector. There are many other methods to calculate the normalized decision matrix. Interested readers should review the work by Jahan and Edwards about the influence of normalization techniques in ranking [191].

3. Create the weighted decision matrix by multiplying each column of the normalized decision matrix **R** with its associated weight w_j. The weighted normalized value is calculates as so:

$$v_{ij} = w_i \cdot r_{ij} \text{ for i = 1,2,...,m and j = 1,2,...,n} \tag{5.14}$$

   where w_i is weight to the ith attribute or criteria.

4. Determine the positive-ideal and negative-ideal solutions.

$$\begin{aligned} A^* &= ({}^{max}_{i}\ v_{ij}|j\epsilon J), ({}^{min}_{i}\ v_{ij}|j\epsilon J')|i = 1, 2, \dots, m \\ &= v_i^*, v_2^*, \dots, v_j^*, \dots v_n^* \end{aligned} \tag{5.15}$$

$$\begin{aligned} A^- &= ({}^{min}_{i}\ v_{ij}|j\epsilon J), ({}^{max}_{i}\ v_{ij}|j\epsilon J')|i = 1, 2, \dots, m \\ &= v_i^-, v_2^-, \dots, v_j^-, \dots v_n^- \end{aligned} \tag{5.16}$$

   where J is associated with the benefit criteria and J' is associated with the cost criteria.

5. Calculate the separation measure. This is performed by calculating the n-dimensional Euclidean distance. The separation from the positive-ideal solution S_i^* and negative-ideal solution S_i^- are calculated as follows:

$$S_i^* = \sqrt{\sum_{j=1}^{n}(v_{ij} - v_j^*)^2},\ \text{i} = 1,2,\ldots,\text{m} \tag{5.17}$$

$$S_i^- = \sqrt{\sum_{j=1}^{n}(v_{ij} - v_j^-)^2},\ \text{i} = 1,2,\ldots,\text{m} \tag{5.18}$$

6. Calculate the relative closeness to the ideal solution. The relative closeness of alternative A_i with respect to A^* is calculated as follows:

$$C_i^* = \frac{S_i^-}{S_i^* + S_i^-},\ 0 < C_i^* < 1,\ i = 1, 2, \ldots, m \tag{5.19}$$

   where the closer alternative A_i is to the ideal solution A^* the more C_i^* approaches 1.
7. Rank alternatives by sorting by relative closeness.

TOPSIS is used when the decision maker has information on attributes and wants to determine an order of preferences between different alternatives [206]. In a survey from 2000 to early 2012, a total of 269 publications have been published about TOPSIS with 62 publications (23%) related to design, engineering and manufacturing systems [207]. A form of TOPSIS has been used for material selection of gears [208], MEMS [199], tool holder under hard milling conditions [209], pipes [210], gate dielectrics [200] and MEMS electrostatic actuators [201].

5.3.3 Multi-criteria Optimization and Compromise Solution

The VIKOR method was created to optimize multiple criteria in complex systems [211]. In the VIKOR approach, the optimal selection is determined by comparing the closeness to the ideal solution. If the solution are too close together, then multiple alternatives may be given in order of their ranking. The following is referred to as the comprehensive VIKOR as it allows benefit, cost and target objectives to be used [212].

The VIKOR method in the following steps looks at a set of m alternatives and n criteria.

- Step 1: Indicate the favorable values T_{ij} for all criteria

  $$T = T_1, T_2, \ldots, T_j, \ldots, T_n = \text{Most desirable element } r_{ij} \text{ or target value for criteria j} \tag{5.20}$$

  where r_{ij} is an element of the decision matrix related to alternative i with respect to criteria j $|i = 1, 2, \ldots, m$ and $j = 1, 2, \ldots, n$.

- Step 2: Calculate the group utility S_i and individual regret Q_i values.

$$S_i = \sum_{j=1}^{n} w_j \left(1 - e^{\frac{|r_{ij} - Tj|}{-Aj}}\right) \tag{5.21}$$

$$R_i = \overset{\max}{j} \left[w_j \left(1 - e^{\frac{|r_{ij} - Tj|}{-Aj}}\right)\right] \tag{5.22}$$

where $A_j = 1$ if elements of criteria j are normalized between 0 and 1, or $A_j = \max r_j^{max}, T_j - minr_j^{min}, T_j$.

- Step 3: Calculate the aggregating index Q_i.

$$\mathcal{Q}_\rangle = \begin{cases} \frac{R_i - R^-}{R^+ - R^-} & \text{if } S^+ = S^- \\ \frac{S_i - S^-}{S^+ - S^-} & \text{if } R^+ = R^- \\ \frac{S_i - S^-}{S^+ - S^-}\upsilon + \frac{R_i - R^-}{R^+ - R^-}(1 - \upsilon) & \text{otherwise} \end{cases} \tag{5.23}$$

where $S^- = \min S_i$, $S^+ = \max S_i$, $R^- = \min R_i$, $R^+ = \max R_i$, υ is the weight for the strategy of the majority of criteria, or maximize group utility, and 1-*upsilon* is the weight for the strategy of individual regret. The value for υ lies between 0 and 1, where $\upsilon = 0.5$ is vote by consensus [213].

- Step 4: Sort results in three different list showing S, R and Q in decreasing order.
- Step 5: Suggest alternative $A^{(1)}$, which has the lowest Q value, if the following conditions are met:
  - *Condition 1:* Acceptable advantage:

$$Q(A^{(2)}) - Q(A^{(1)}) \geq DQ \tag{5.24}$$

where $A^{(2)}$ is the second best alternative, or the second lowest Q value, where $DQ = 1/(m-1)$ and m is the number of alternatives.

- *Condition 2:* Acceptable stability in decision making:
The alternative $A^{(1)}$ should be the best ranked in S and/or R.

If the conditions are not met, then the suggest a set of solutions following this procedure.

  - Alternative $A^{(1)}$ and $A^{(2)}$ if only condition 2 was not satisfied.
  - Alternatives $A^{(1)}, \ldots, A^{(i)}$ if C1 was not satisfied. $A^{(i)}$ is determined by the relation $Q(A^{(i)}) - Q(A^{(1)}) > DQ$.

VIKOR has been used significantly in selection methods. In a survey from 2004 to 2013, a total of 176 papers have been published using VIKOR with 35 papers ($\approx$ 20 %) related manufacturing and material selection topics [214].

5.3.3.1 AHP+MCDM Method

The combination of both AHP and another MCDM method (AHP+MCDM) allows for simple calculations of weights and the implementation of benefit, cost and target criteria. This AHP+MCDM method consists of the following steps: 1) identify criteria, 2) AHP weight computations and 3) evaluate alternatives with TOPSIS and VIKOR. These methods have been implemented frequently and have had used extensively in MCDM material selection methods and readers are directed two these two literature surveys [207, 214]. Of the 176 papers surveyed in the VIKOR review, 70 papers either compared or integrated TOPSIS and AHP [214].

There have been many discussion over which MCDM method is better [215]. To actually select the optimal MCDM can be considered a MCDM problem by itself. Luckily, most reviewers indicate the best approach is to utilize multiple MCDM and review the result [216]. Technically, the modified VIKOR has been proven to provide correct answers at edge cases unlike TOPSIS, but both methods will be used as TOPSIS is the most popular [211].

5.4 Summary and Comments

An overview of how one should select based on actuators, sensors and energy harvesters and selection methods have been discussed in this chapter.

Actuators can be viewed either as energy or, if they are operated withing a certain time frame, power devices. The actuator figures of merit provide the least clarity even though actuator can easily be related to intrinsic material properties. Sensors are devices that make accurate measurement within a desired amount of time. Sensor figures of merit are largely statistical and are device dependent where the only possible material figures of merit are sensitivity and hysteresis. Energy harvesters are devices that transfer ambient energy to useful electrical energy. For the present, the energy harvester figures of merit should be related to the energy output as the harvester output is too low to power devices without some storage circuit.

The optimal material selection method is in fact a multi-criteria decision making problem. For the case of material selection, the use of AHP and two MCDM methods are suggested. AHP is a decision making framework that will assist in creating relationships between criteria and sub-criteria and weighting. TOPSIS and VIKOR are the two most popular methods to be used, aside from AHP, and will be used in the ranking of the alternatives.

Chapter 6

Implementation of Selection Method

The three most popular active material have been discussed with an emphasis on understanding the phenomenon and the application limitations. Afterwards, the discussion of selection methods and performance criteria has indicated some issues of the contemporary application specific figures of merit and indicated that using a procedure called AHP integrated with two MCDM methods called TOPSIS and VIKOR can create a ranking of alternative materials based upon the designer-specified criteria. Thus, this chapter delves into application of the knowledge base created to select material in two different topics.

Mechanical energy harvesting is a burgeoning field that is actively pursued in academia. While many different designs have been developed and applications discovered, the market implementation has not occurred. One of these reasons is that energy harvesters still have not provided enough energy output. One factor in improving energy harvester output is proper material selection. While some designers have selected based upon material parameters, it seems that practically all piezoelectric and magnetostrictive material have been employed at some point. Through an analysis of literature, selection strategies are ascertained from these designers and used to create an optimal list of materials based upon a designer-specified weighting. The AHP+MCDM material selection for energy harvester will be used to demonstrate the process which is simpler shown than defined.

The second optimal material selection was for ultrasound transducer because ultrasound transducers exemplifies the compromise decision between the acoustic transmission matching, transmitting (actuating) and receiving (sensing) performance. Some designers select using two figures of merit that represent transmission and receiver performance [217]. Others indicate the most important task is to select based upon impedance matching between the tissue and the actuator [218]. Yet, these simplifications are not necessary using the proposed AHP+MCMD methods. Thus, the optimal material selection can be selected.

While the material selected is referred to as ‘optimal’, this method is dependent upon the criteria selected and designer preference. Thus, there is an optimal material for a specified application and a designer preference, but there is no optimal material.

6.1 Mechanical Energy Harvesters

Mechanical energy harvesters are categorized by the manner in which mechanical energy is transfered to the transducer [219]. In direct force energy harvesters, the transducer converts a time-varying force into electric energy. In inertial energy harvesters, the kinetic energy is stored between an inertial mass on which the transducer acts as a damper to extract electric energy. Of the two, inertial energy harvesters have greater ability for miniaturization as the structure only requires one attachment point [220].

A traditional inertial energy harvester is a cantilever beam with a mass at the end, see Figure 6.1. In this structure, the base excitation is converted into kinetic energy of the tip mass that is transferred into potential energy of the cantilever beam. The transducer is situated on the beam and is deformed resulting in electric energy generation.

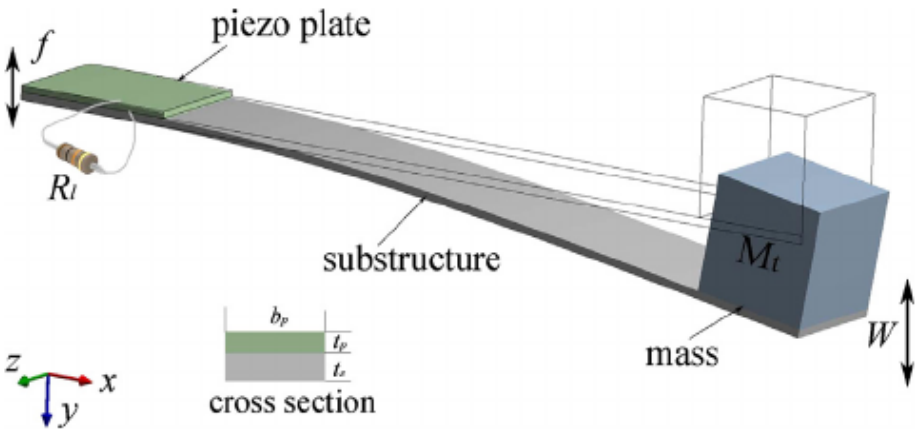

Figure 6.1: An illustration of cantilever piezoelectric energy harvester (Reprinted from [221], with permission from Elsevier).

The energy harvester function, constraints and objective can be found in Table 5.6. Due to the low energy output of energy harvesters, there still has not been large-scale commercial usage and most research has been focused upon improving the energy output of the device. Thus, energy output is the objective of the technology designer.

The energy output is dependent upon a few generic parameters. Material selection determines the ability of the system to convert energy from the mechanical to the electrical domain. Electrical impedance matching ensures optimal power transfer. Since the system is dynamic, the power output is dependent upon the frequency of input vibrations.

In this study, resonant energy harvester will be considered. Although there are designs for a broadband energy harvester, the design will only consider narrow-band resonant energy harvester. The materials considered will be both piezoelectric and magnetostrictive. Both materials have similar constitutive equations, which allows for an easier comparison.

6.1.1 Resonant Energy Harvester Figures of Merit

In the selection of material, there are many strategies that designers use to justify their selection. Most designers use generalized figures of merit that define electromechanical coupling, transmission coefficient [222], normalized power output [180] or efficiency [223]. Others indicate a set of material parameters such as coupling coefficient, mechanical quality factor and, for piezoelectrics, permittivity that drive their selection [224]. In some instances, the decision is based upon a comparison of the advantages and disadvantages of different transduction methods [225]. Each of these methods have merit and can be used to derive proper material selection methods.

In the selection of what criteria to be used, the decision will be limited to generalized figures of merit and intangibles that were defined in the comparison of advantages and disadvantages of different transduction methods. The criteria that will be used are energy output, design complexity and specific density. While some criteria may be of such low importance that they could be null, it should be still included in the review as the weight of this criteria is clearly indicated.

6.1.1.1 Energy Output

The simplest figure of merit is the coupling coefficient, which was defined in Equation 5.7. As was discussed in Section 5.1.1, the coupling coefficient can be defined as the ratio of energy stored at the output port from the total input energy. Yet, the coupling coefficient and efficiency are different as one considers the energy stored at the transducer port and the other considers the energy output. In this way, the coupling coefficient which is independent of the state of the output does not provide a measure of the efficiency of the device and will not be considered as a figure of merit in this analysis.

The piezoelectric, and magnetostrictive, equation for maximum power is derived from the generalized maximum transmission coefficient. It represents the maximum power output of a vibration-based generator and can be used to determine the theoretical maximum output that a system can obtain based upon material and model based parameters. The derivation of this coefficient can be found in Roundy [180] and is defined as follows:

$$P_{max} = \frac{k^2 m (QA)^2}{4\omega} = (k^2 Q^2)\frac{mA^2}{4\omega} \tag{6.1}$$

where k^2 is the coupling coefficient, m is the inertial mass, Q is the mechanical damping, A is area and ω is the frequency. It will be assumed that the damping of the cantilever will not vary by different material selection and thus $Q = Q_m$ the mechanical quality factor of the material. With this assumption, the first selection criteria C_1 can be defined:

$$P_{max} \propto k^2 Q_m^2 \tag{6.2}$$

$$C_1 = k^2 Q_m^2 \tag{6.3}$$

Table 6.1: Physical Characteristics of power conversion devices and calculated efficiency [223].

Configuration	k^2	Q	k^2Q^2	Efficiency
Stack	0.581	1.63	1.54	0.531
Bulk	0.029	1079	33200	0.941
Cantilever	0.08	229	4200	0.909
Cantilever	0.043	200	1720	0.818
Diaphragm	0.053	135	966	0.791
Diaphragm	0.125	53	351	0.791

While P_{max} is a useful figure of merit and indicates that for maximum power output the coupling coefficient and quality factor should be maximized, it does not provide guidelines of how the values of Q and k^2 have on the efficiency of the system which in some cases dictates the selection, see Table 6.1.

Of particular note is the last two items which show equal efficiency but completely different k^2Q^2. Efficiency, which was theoretically derived in Richards et al. [223] and experimentally validated in Cho et al. [226], is defined as follows:

$$\eta = \frac{1}{2}\frac{k_{sys}^2}{1-k_{sys}^2} \Bigg/ \left(\frac{1}{Q_{sys}} + \frac{1}{2}\frac{k_{sys}^2}{1-k_{sys}^2}\right) = \frac{0.5k_{sys}^2 Q_{sys}}{(1-k_{sys}^2) + 0.5k_{sys}^2 Q_{sys}} \tag{6.4}$$

where k_{sys}^2 indicates coupling coefficient and Q_{sys} indicates quality factor of the system. The coupling coefficient $k_{sys}^2 = C/(C_0+C)$ is determined from the material properties and electrode configuration through C_0 [223], and is referred to as the clamped capacitance [227]. The C parameter is motional capacitance, or structural stiffness, of the device. The quality factor $Q_{sys} = (m\bar{s})^{1/2}/b$ depends upon the mass m, stiffness $\bar{s}$ and damping of the structure b. It is assumed here that a higher material quality factor Q_m improves the quality factor of the system and that k_{sys} is improved by a higher electromechanical coupling coefficient k^2.

In an article by S. Priya, this figure of merit is used but it is erroneously indicated that it can be simplified to k^2Q_m [228]. In Table 6.2, the variation between theoretical values of k^2Q_m and η are shown. While a high value of k^2Q_m results in better efficiency, k^2 value has an effect on the efficiency, which is simple demonstrated by looking at η. Efficiency, though, will be considered as the second criteria C_2 for an optimal energy harvester material selection:

$$C_2 = \eta = \frac{0.5k_m^2 Q_m}{(1-k_m^2) + 0.5k_m^2 Q_m} \tag{6.5}$$

6.1.1.2 Design Complexity

In the selection of materials, some designers indicate their decision somewhat rests upon reducing the dielectric constant of piezoelectric for more current [224], the high electrical

Table 6.2: Difference between k^2Q_m and η

	Q_m			
k^2	1000	100	10	1
0.0001	0.048	0.00498	0.0005	0.0001
0.001	0.334	0.048	0.00498	0.001
0.01	0.835	0.336	0.048	0.00503
0.1	0.982	0.847	0.357	0.053

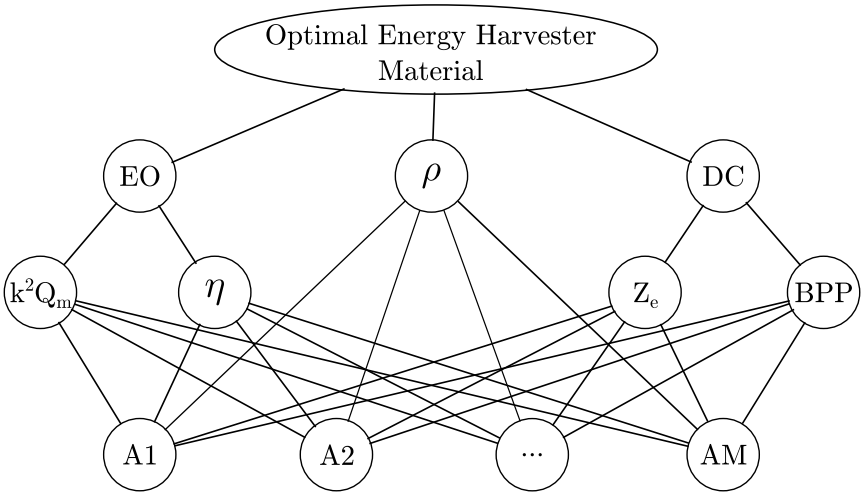

Figure 6.2: Decision hierarchy for energy harvester selection. The top is the goal. Second row is the criteria, where EO is energy output, ρ is density, DC is design complexity. Third row is the sub-criteria, where k^2Q_m is the maximum power, η is efficiency, Z_e is the boolean value for impedance matching, and BPP is the boolean value for requiring bias field, prestress mechanism and a pickup coil.

impedance of piezoelectrics or bulky secondary systems required to be used for magnetostrictives [225].

As it is hard to indicate the relative merits of matching different levels of electrical impedance to the bulkiness of the magnetostrictive system, two criteria have been to selected to indicate a boolean value if it requires impedance matching Z_e or the system requires a bias field, prestress mechanism and a pickup coil (BPP). Some value of weight addition or cost could be constructed for these systems, but both these criteria are viewed quite unimportant compared to energy output.

6.1.2 Generation of Weights

The AHP process is used to generate weight for different criteria and sub-criteria. A summary of the selection criteria and their relationship in the AHP scheme is shown in Figure 6.2.

In Table 6.3, the criteria pairwise comparison matrix using the AHP scale, Table 5.7,

Table 6.3: Pairwise comparison matrix of energy harvester criteria

	EO	DC	ρ
EO	1	9	9
DC	1/9	1	1/2
ρ	1/9	2	1

is shown. Energy output (EO) was viewed as extremely important compared to design complexity, where extreme importance has a value of 9 on the AHP scale. Therefore, the second element of the EO row was given a weight of EO/DC = 9. The comparison between design complexity compared to energy output was given the reciprocal value. Thus, in the second row and first element DC/EO = 1/9. Energy output was deemed to be extremely important over density, and thus EO/ρ = 9 and ρ/EO = 1/9. Lastly, design complexity was viewed to be slightly less important than ρ, so DC/ρ = 1/2 and ρ/DC = 2. All values on the diagonal are 1 as they compare the same criteria.

In an ideal scenario, the decision making is entirely consistent. By consistent, each element would be equal to a product of two others. For example, the product of DC/EO (1/9) and EO/ρ (9) should equal DC/ρ (1/2), but it does not. As the pairwise comparisons of tables greater than 2 elements are likely somewhat inconsistent, the AHP process employs an eigenvalue calculation to measure the consistency index of the table. Where the consistency index (CI), as defined by Saaty [229], is calculated as follows:

$$CI = \frac{\lambda_{max} - n}{n - 1} \tag{6.6}$$

where λ_{max} is principal eigenvalue and n is the number of elements in the square matrix. If the matrix is completely consistent, then λ_{max} = n and CI = 0. Otherwise, the CI then is compared to the average value CI for random matrices using the Saaty scale, which is referred to as the mean of random matrix consistency indexes (RI) [230]. The following consistency ratio (CR) is calculated:

$$CR = \frac{CI}{RI} \tag{6.7}$$

where the decision matrix is deemed to be consistent if the CR¡0.1. The RI value can be found in tables or calculated with Equation 6.6 where principal eigenvalue λ_{max} is equal to an empirical formula for the mean of the random matrices principal eigenvalue $\overline{\lambda_{max}} = 2.7699n - 4.3513$, where $\overline{\lambda_{max}}$ is the mean of the random matrices principal eigenvalue and n is the size of the square matrix.

In the case of Table 6.3, the table is deemed to be consistent, CR<0.1. Since the CI = 0.02681 and RI = 0.4792, results in a CR of 0.05595. The lower the CR, the more consistent the comparisons.

The eigenvector calculated is used to determine the weight of elements. Thus, the weights calculated for the criteria matrix are shown in Table 6.4. As was indicated in Table 6.3, the extreme importance of energy output results in a higher weight. Similarly,

Table 6.4: Eigenvector weights generated from the pairwise comparison matrix of criteria

	EO	DC	ρ
Weights	0.8142	0.07180	0.1140

Table 6.5: Pairwise comparison matrix of energy output sub-criteria

	$k^2Q_m^2$	η
$k^2Q_m^2$	1	3
η	1/3	1

density was viewed to be mildly more important than design complexity and received a higher weight.

Following this method, the energy output sub-criteria and design complexity sub-criteria pairwise comparison were done, see Table 6.5 and 6.6 respectively. Since the size of the matrix is only two, there is no need to measure the CR, since it will be completely consistent. The weights for the sub-criteria was generated and is shown in Table 6.7.

Using Table 6.4 and 6.7, the complete weights for each criteria can be calculated, see Table 6.8. The weights for $k^2Q_m^2$ and η were calculated by multiplying the weight of energy output (0.8142) by the sub-criteria weight generated for $k^2Q_m^2$ (0.75) and η (0.25).

While the use of this system is to introduce more objectivity in the decision making process, weight generation is fundamentally a subjective process. There is no guarantee that two decision makers will generate the same pairwise comparison matrix. In an effort to reduce this variance, some MCDM methods use fuzzification of the weights [231, 232]. While this reduces the subjectivity of the weights, it also affects the transparency of the decision making process and will not be used.

6.1.3 MCDM Material Selection for Energy Harvesters

The criteria values for different alternatives is shown in Table 6.9. Some of the values were missing and were calculated through piezoelectric relations which can be found in Jaffe [16].

In TOPSIS, the designer is required to define the positive-ideal solution (PIS) and the negative-ideal solution (NIS), which in this case is the opposite of PIS. In VIKOR, only the desired values are needed to be declared, and thus are identical to PIS. These design objectives for the criteria are shown in Table 6.9.

Table 6.6: Pairwise comparison matrix of design complexity sub-criteria

	BPP	Z_e
BPP	1	7
Z_e	1/7	1

Table 6.7: Eigenvector weights from the pairwise comparison of sub criteria

	$k^2Q_m^2$	η	BPP	Z_e
Weights	0.75	0.25	0.875	0.125

Table 6.8: Weights for selection criteria

	$k^2Q_m^2$	η	BPP	Z_e	ρ
Weights	0.6107	0.2036	0.0628	0.0090	0.1140

Table 6.9: Criteria Values for different alternatives. **Bold = estimated through piezoelectric equations**.

#	Name	k_{31}	Q_m	$k^2Q_m^2$	η	BPP	Z_e	ρ
	Design objective	–	–	max	max	min	min	min
A1	$BaTiO_3$	0.21	300	13	0.87	0	1	6020
A2	$LiNbO_3$ (36 Rotated Y-cut)	**0.022**	10000	**4.9**	**0.71**	0	1	4628
A3	PZT 4	0.33	500	54	0.97	0	1	7500
A4	PZT 5A	0.34	75	8.7	0.83	0	1	7750
A5	PZT 5H	0.39	65	9.9	0.85	0	1	7500
A6	PZT 8	0.295	1000	87.0	0.98	0	1	7600
A7	PMN-28%PT Type A	0.43	120	22	0.93	0	1	8100
A8	PMN-32%PT Type A	0.44	120	23	0.94	0	1	8100
A9	PIN24%-PMN-PT (2nd Gen)	0.46	180	38	0.96	0	1	8122
A10	PIN33%-PMN-PT (2nd Gen)	0.47	180	40	0.96	0	1	8141
A11	PVDF	0.12	20	0.29	0.13	0	1	1800
A12	P(VDF-TrFE)	0.07	20	0.1	0.05	0	1	1900
A13	PVDF	0.1	13	0.13	0.062	0	1	1780
A14	P(VDF-TrFE) 75/25	**0.070**	19.61	**0.10**	**0.046**	0	1	1880
A15	AlN	**0.12**	2490	**33**	**0.94**	0	1	3300
A16	CdS	**0.12**	1000	**14**	**0.88**	0	1	4820
A17	GaN	**0.11**	2800	**33**	**0.94**	0	1	5986
A18	ZnO	**0.18**	1700	**56**	**0.97**	0	1	5680
A19	Emfit 70μm thick	**0.00061**	1100	**0.00041**	**0.00021**	0	1	330
A20	Emfit 80μm thick	**0.00064**	1100	**0.00045**	**0.00023**	0	1	330
A21	Terfenol-D	0.75*	20	11	0.93	1	0	9250
A22	Galfenol	0.65*	24.6	10	0.90	1	0	7800

* - Magnetostrictives cantilever operate in 33-mode [225]

Table 6.10: Energy Harvester MCDM ranking results for TOPSIS and VIKOR(v=0.5). **Bold = ranking partially based upon estimated values**.

		TOPSIS				VIKOR			
#	Name	S^*	S^-	C^*	Rank	S	R	Q	Rank
14	**P(VDF-TrFE) 75/25**	**0.3731**	**0.0534**	**0.1251**	**22**	**0.5347**	**0.3858**	**0.9996**	**22**
13	PVDF	0.3728	0.0536	0.1258	21	0.5322	0.3857	0.9968	21
12	P(VDF-TrFE)	0.3693	0.0535	0.1265	20	0.5322	0.3834	0.9933	20
11	PVDF	0.3716	0.0540	0.1268	19	0.5263	0.3853	0.9898	19
19	**Emfit 70μm thick**	**0.3738**	**0.0570**	**0.1322**	**18**	**0.5204**	**0.3860**	**0.9846**	**18**
20	**Emfit 80μm thick**	**0.3738**	**0.0570**	**0.1322**	**17**	**0.5204**	**0.3860**	**0.9846**	**17**
2	**$LiNbO_3$(36° Rotated Y-cut)**	**0.3497**	**0.0657**	**0.1581**	**16**	**0.4713**	**0.3730**	**0.9117**	**16**
22	Galfenol	0.3317	0.0660	0.1660	15	0.4790	0.3586	0.8977	15
21	Terfenol-D	0.3280	0.0698	0.1755	14	0.4776	0.3557	0.8918	14
4	PZT 5A	0.3342	0.0743	0.1818	13	0.4613	0.3624	0.8846	13
5	PZT 5H	0.3290	0.0777	0.1910	12	0.4529	0.3589	0.8701	12
1	$BaTiO_3$	0.3154	0.0868	0.2159	11	0.4308	0.3498	0.8323	11
16	**CdS**	**0.3109**	**0.0907**	**0.2259**	**10**	**0.4173**	**0.3468**	**0.8131**	**10**
7	PMN-28%PT Type A	0.2780	0.1159	0.2941	9	0.4035	0.3214	0.7588	9
8	PMN-32%PT Type A	0.2738	0.1196	0.3039	8	0.3981	0.3180	0.7479	8
17	**GaN**	**0.2307**	**0.1567**	**0.4046**	**7**	**0.3497**	**0.2824**	**0.6407**	**7**
15	**AlN**	**0.2299**	**0.1580**	**0.4073**	**6**	**0.3285**	**0.2824**	**0.6178**	**6**
9	PIN24%-PMN-PT (2nd Gen)	0.2106	0.1759	0.4551	5	0.3392	0.2630	0.5992	5
10	PIN33%-PMN-PT (2nd Gen)	0.2022	0.1837	0.4761	4	0.3312	0.2549	0.5781	4
3	PZT 4	0.1432	0.2400	0.6264	3	0.2635	0.1928	0.4090	3
18	**ZnO**	**0.1335**	**0.2485**	**0.6505**	**2**	**0.2422**	**0.1830**	**0.3711**	**2**
6	PZT 8	0.0291	0.3765	0.9282	1	0.0692	0.0635	0.0000	1

Using the algorithms described in Section 5.3.2 and 5.3.3, the material ranking for the energy harvester was completed, see Table 6.10. Both algorithms resulted in the same rank. In TOPSIS, PZT 8 had the shortest distance to the PIS S^* and furtherest distance away from the NIS S^- which resulted in a relative closeness ranking C^* of nearly unity. As well, ZnO and PZT 4 seem to have nearly identical rankings. VIKOR, which suggests one or more alternatives depending upon conditions stated in Section 5.3.3, indicated that the solution is only PZT 8. Similarly to TOPSIS, PZT 8 had a noticeable improvement in group utility S, where $\min S$ indicates majority rule, and individual regret R, where $\min R$ indicates a decision with the least amount of opponents [211].

For the designer preference indicated, the preferred candidate for a resonant cantilever energy harvester is PZT 8, which is preferred by a large margin. The only caveat is this is dependent upon the assumption that the quality factor can be defined as the mechanical quality factor of the material.

6.2 Ultrasound Imaging Transducers

Ultrasound imaging is based upon a transducer that acts as a transmitter and receiver. This is achieved by using the transducers with an input electric signal which is converted to mechanical energy and creates an acoustic wave (transmitter) and converting the mechanical energy of the acoustic wave echo back into the electric domain (receiver). During the receiver operation, the wave intensity reflected from the organs is recorded as a function of time. To achieve both transmitting and receiving, the transducer acts as an actuator and a sensor at different times. Thus, the function of the ultrasound imaging transducer

is to create images of tissue by measuring the time between transmitting and receiving ultrasound acoustic waves.

Depending upon what organ is to be investigated, the transmitter must be operated at different frequencies, where 2.5–5 MHz for deep organs and 20–100 MHz for skin, arteries and other tissues [233, 234]. There are two modes to operate ultrasound transducers, the conventional pulse-and-echo or continuous wave modes [233]. Therefore, the constraints of the ultrasound imaging transducer considered will be the operation bandwidth (which fixes the type of tissues that can be investigated) and operation method (pulse-and-echo or continuous wave modes). In this selection, we will looking at the traditional pulse-and-echo mode and operating at low MHz frequencies.

A good ultrasound imaging transducer transmits acoustic waves effectively, sensitively responds to acoustic echoes with minimal noise and is simple to construct. The objectives can be used to measure performance and will be described as transmission performance, receiver performance and design complexity.

Although designers have used magnetostrictive ultrasonic transducers, it seems that the ultrasound transducers are predominantly piezoelectric. The exact reason is not explained. The reason likely is explained somewhat by Table B.4 and the application requirements. Piezoelectrics offer a more compact design (no coil and magnetic bias) at a fraction of the price, have less loss and heat buildup at high frequencies. Thus, they will be omitted from the selection.

6.2.1 Basic Piezoelectric Transducer Design

The traditional ultrasound transducer element is shown in Figure 6.3. The transducer consists of a piezoelectric disc that is operated in thickness mode. The thickness mode indicates that the material thickness is poled and vibrates, where the thickness is much smaller that the lateral dimensions resulting in all strain components to be zero except along the thickness [227]. If the two surfaces of the piezoelectric element are counted as separate vibrators, the resonance can be determined:

$$f_0 = n\frac{\upsilon}{2t} \tag{6.8}$$

where f_0 is the resonant frequency, υ is the sound velocity in the transducer, n is an odd integer and t is the thickness [235]. This ensure the reflected signal is in phase [236] and it indicates acceptable thickness for the active material. Resonance occurs when the thickness t is equal to odd multiples of the half wavelength λ, where $\lambda = \upsilon/f_0$. In actuality, designers reduce the thickness of the active material to less than $\lambda/2$ to account for mass loading effects and the attenuative losses during acoustic transmission and reception [237].

To achieve better performance, matching and backing layers are bonded to the electroded piezoelectric disc.

At the front side of the transducer which faces the medium that acoustic waves are transmitted and received, one or more impedance matching layers are used to improve

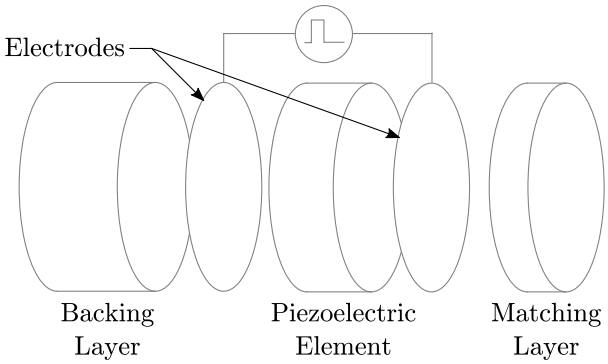

Figure 6.3: Schematic of a piezoelectric ultrasound transducer (Adapated from [45] ©2005 IEEE).

energy transfer between the active material and the medium. These matching layers are required in conventional piezoelectric materials used have an acoustic impedance of piezoelectrics is high (30–35 MRayl where 1 MRayl = 10^6 kg/m^{2}s) compared to the tissue which is low (1.5–5 MRayl) [234]. If no matching layer is used, the energy transfer to the medium is low and the transducer temperature will increase which will reduce the SNR of the receiving mode.

For 100% acoustic transmission between the piezoelectric and the tissue, it requires certain matching layer thickness (generally $\lambda/4$) and the impedance between the matching layer should be set to a certain value. The acoustic impedance of a narrow-band transducer matching layer should be equal to $Z = \sqrt{Z_{piezo} Z_{medium}}$, where $Z_{piezo} = \rho \upsilon$ and ρ is density of the piezoelectric element [235]. Whereas for a broadband transducer, Desilets et al. [238] showed that for a single matching layer the acoustic impedance Z_m should be:

$$Z_m = (Z_1 Z_2^2)^{1/3} \tag{6.9}$$

where Z_1 is the impedance of the piezoelectric element and Z_2 is the impedance of the load medium [239]. If there are two matching layers, then the ideal inner matching layer impedance Z_{m1} and outer matching layer impedance Z_{m2} should be:

$$Z_{m1} = (Z_1^4 Z_2^3)^{1/7} \tag{6.10}$$

$$Z_{m2} = (Z_1 Z_2^6)^{1/7} \tag{6.11}$$

The use of the matching layer improves sensitivity and reduces the acoustical resonance of the active element [45]. This is shown in Figure 6.4 where the matching layer improves the impulse response and the resonance decays quicker.

On the back side of the transducer, a backing layer is sometimes used to mechanically damp the active material oscillations. The damping increases as the acoustic impedance between the backing layer and active element are matched, see Figure 6.5. While this results in a lower sensitivity, the axial resolution is improved [45]. This indicates the backing layer

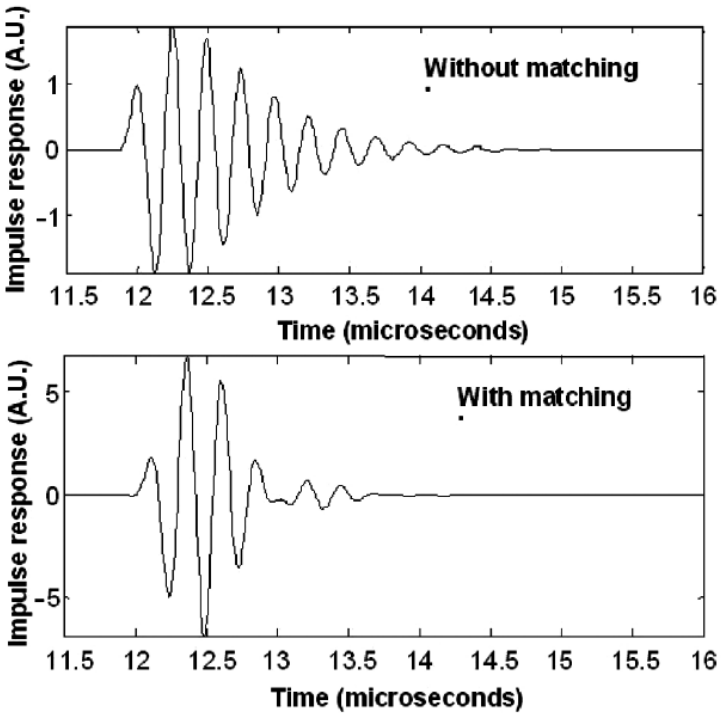

Figure 6.4: Impulse response of a lightly backed (Z = 4 Rayl) piezoelectric ultrasound transducer without and with matching layer ([45] ©2005 IEEE).

selection is dependent upon the trade-off between axial resolution and sensitivity. The typical backing layer acoustic impedance is 3–7 MRayl [237] compared to heavy backing of 10 MRayl for PZT ultrasound transducers [45]. The backing material should attenuate the echo by 90 to 100 dB [237]. If no backing layer is used, then it requires a low Q_m material [217].

Lastly, the optimizing of energy transmission requires that the piezoelectric impedance should match the electrical impedance of the coaxial cable and electric circuitry. Typically, the value of 50 Ω is used for the electrical impedance and the piezoelectric impedance is inversely related to the capacitance and proportional to the thickness of the transducer [234], see Equation 6.13.

$$R \propto \frac{1}{j\omega C} \tag{6.12}$$

$$C = \frac{\epsilon A}{t} \tag{6.13}$$

where R is the electrical impedance, C is capacitance and A is area. Due to the thickness constraint for the resonant frequency, the variable to change the electrical impedance is the dielectric constant. Some designers at high frequencies indicate material selection should be based upon achieving a lower electrical impedance [240, 241].

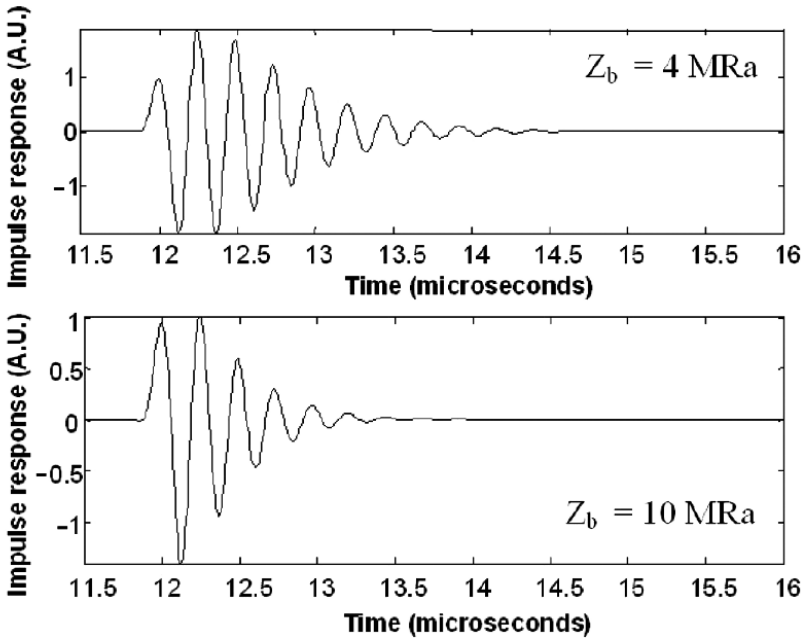

Figure 6.5: Impulse response of a light backed (Z = 4 MRayl) and heavy backed (Z = 10 MRayl) piezoelectric ultrasound transducer ([45] ©2005 IEEE).

6.2.2 Review of Piezoelectric Ultrasound Figures of Merit

Alongside the design considerations related to impedance matching, there are some piezoelectric ultrasound figures of merit that are used to indicate ultrasound imaging performance. The criteria related to the ultrasound transducer material selection are transmission performance, receiver performance and design complexity.

Through the following review, it was found that different designers offered contradictory relations for some figures of merit. For example, some designers say dielectric constant should be low at high frequencies [242, 241, 234] and others say that it should be high for ease of electrical impedance matching [235, 240]. Similarly, there is no consensus on the material quality factor. Some say it is not important [217], others say it should be low [242, 243, 65], others say it should be high [218, 240, 244, 234], and some show it is not important [245].

It is the author's opinion that the dielectric permittivity should be low as it improves the piezoelectric voltage ($g = d/\epsilon$), whereas there is no certainty that having a high permittivity will ensure electrical impedance matching is not required. For quality factor, it will be assumed that it is not important as there has been good results with $LiNbO_3$ (Q_m = 10,000) and $PbTiO_3$ (Q_m = 120) [245].

The following review identifies sub-criteria that will be used in the AHP+MCDM method.

6.2.2.1 Transmission Performance

One of the functions of a ultrasound transducer is the ability to create strain from an electric input. Thus, a simplified figure of merit used by multiple authors [246, 247, 248, 243, 234] indicates that transmission performance is derived by solving the equations of motion for x_t, which is the amplitude of motion at the front surface caused by 1 volt input across the terminals, see Appendix A. If we assume quasi-static operation, a simple parameter, derived by Callerame et al. [217], is the transmission efficiency:

$$TP = \frac{k_t}{1 - k_t^2}\sqrt{\frac{\epsilon_{33}^S}{c_{33}^D}} \tag{6.14}$$

where k_t is the thickness coupling coefficient, ϵ_{33}^S is the dielectric constant during constant strain and c_{33}^D the elastic stiffness at constant electrical displacement [217]. Yet, this figure of merit is just the piezoelectric strain coefficient d, see Appendix A for proof. While this figure of merit is useful as an actuator performance metric, it assumes that the σ is constant. Since the transducer is not running freely, stress is not constant.

Thus, it is necessary to use a figure of merit called transmission coefficient which accounts for the loading condition. The transmission coefficient (TC), Equation 6.15, is a generalized ratio between input and output energy terms, which uses the generalized coefficients shown in Equation 5.6, and is derived by Roundy [180].

$$TC = \frac{T_2(q_{21}T_1 + (1/2)q_{22}T_2)}{T_1((1/2)q_{11}T_1 + q_{12}T_2)} \tag{6.15}$$

where T_1 indicates the through variable at the input port and T_2 indicates the through variable at the output port, see Equation 5.6. The maximum transmission coefficient, derived by Roundy [180], occurs when the output load is half of the maximum generative through and across variables and results in the following equation:

$$TC_{max} = \frac{k^2}{4 - 2k^2} \tag{6.16}$$

Thus, the higher the coupling coefficient the higher the maximum transmission coefficient. This figure of merit will be used to determine the ability of the transducer to produce a pressure wave in the tissue.

As well, designers have indicated that having a high curie temperature is necessary to ensure ease of manufacturing [242, 14, 218, 241, 65]. Generally, conventional piezoelectric ultrasound transducers have a curie temperature of roughly 210° C [14]. As was discussed in Section 2.3.6, the half curie temperature is the suggested temperature limit for piezoelectric operation. For this analysis, any materials with a half curie temperature below $41°C$, the temperature which causes patient discomfort [237], will be omitted. Thus, cellular polypropylene is viewed as too low and is omitted from the analysis. Curie temperature, or the lower transition temperature T_{RT} for relaxor ferroelectrics, will still be viewed as a

figure of merit for transmitter performance as it determines actuation stability and ease of manufacturing.

6.2.2.2 Receiver Performance

The receiver figures of merit, Equation 6.17 are related to the voltage sensitivity of the sensor to pressure R_{VS} [217] and the signal-to-noise ratio R_{SNR} [15].

$$R_{VS} = \frac{k_t t}{\sqrt{c_{33}^D \epsilon_{33}^S}} \tag{6.17}$$

$$R_{SNR} = \frac{d_{33}}{\sqrt{\epsilon_{33}^T \tan \delta_e}} \tag{6.18}$$

where k_t is the thickness coupling coefficient, c_{33}^D is the stiffness coefficient at constant electric displacement, ϵ_{33}^S is the permittivity at constant strain, ϵ_{33}^T is permittivity at constant stress and $\tan \delta_e$ is the dielectric loss coefficient. From Equation 6.17 and 6.18, the best receiver would have a low ϵ and $\tan \delta_e$ coefficient. Both of these figures of merit will be used in the material selection algorithm.

Multiple different sources have indicate that there is a theoretical basis that higher coupling coefficient results in a higher bandwidth and pulse response [249, 237, 234]. There is a discrepancy between what is viewed as a good metric. Kino uses a relation between bandwidth and thickness coupling coefficient, Equation 6.19, whereas Zhang et al. refers to Equation 6.20. Equation 6.20 was from a book by Sherman [250], yet it indicates that the bandwidth is related to the inverse of the mechanical quality factor. This likely means that it is referring to the coupling coefficient and mechanical quality factor of the device not the material. Therefore, Equation 6.19 will be used as a measurement of a high bandwidth ultrasound transducer.

$$\Delta f(3\,dB)/f_0 \propto k_t \tag{6.19}$$

$$\Delta f(3\,dB)/f_0 \propto k/\sqrt{1-k^2} \tag{6.20}$$

Another important consideration for receiver performance is the effect temperature has on the material property stability. As shown in Section 2.3.6, the general consensus is the material is more stable the further it is away from the curie temperature. Thus, ultrasound designers have discussed the temperature stability of the material as an important consideration [242, 241, 65, 244, 234]. While curie temperature, or T_{RT} is important for transmitters as well, it is likely the temperature-dependent coefficients cause significant noise for ultrasound receiver performance and would likely be more important.

6.2.2.3 Design Complexity

Generally, ultrasound designers that use piezoelectric polymers indicate that the benefit of polymers is the low acoustic impedance [218, 251]. Thus, there is no requirement for adding matching layers. Yet, the impedance mismatch between piezopolymers (≈4 MRayls) and tissues (1.5 MRayls) is still large. While all ultrasound designers indicate that the acoustic impedance matching is extremely important, there does not seem to be a simplified metric to calculate transmission through multiple layers, see Saffar et al. [252]. Naturally, the selection of matching material and piezoelectric would expand the problem and is out of the scope of the selection. For this study, if the material requires a matching layer (ML) or not falls under increasing the design complexity and it has only a boolean value.

While electric impedance matching (Z_eM) was viewed as a less important than a high piezoelectric voltage constant, it will still be counted as selection criteria.

6.2.3 AHP+MCDM Piezoelectric Ultrasound Material Selection

In most instances of piezoelectric material selection, the author cannot deal with the complex compromise decision between matching acoustic and electrical impedance while achieving high transmitter and receiver figures of merit [217, 45, 15, 234]. Each of these authors utilize different strategies to reduce the number of comparisons: Callerame et al. indicate a few metrics should be considered (high coupling coefficient, low acoustic impedance and low stiffness) and offers no optimal [217], M. Lethiecq et al. simplify by indicating that the coupling coefficient and acoustic impedance are the most important parameters [45], Wersing and Lerch utilize an assumption ($d_{33} \approx \sqrt{C_E}$) to reduce the receiver figures of merit to one value C_E [15] and Zhang et al. use only the thickness coupling coefficient because it accounts for resolution, high power efficiency and broad bandwidth [234].

The benefit of the use of the AHP+MCDM material selection is that all figures of merit can be shown and the designer pairwise comparison are clearly indicated. The following segment will cover the selection of weights using AHP and the ranking using both TOPSIS and VIKOR.

6.2.3.1 Generation of Weights

The criteria and sub-criteria identified in Section 6.2.2 are shown in Figure 6.6. The pairwise comparison matrices are shown in Table 6.11. The calculated weights from the pairwise comparison matrix are shown in Table 6.12, where T_c was the sum of the product of the respective criteria and sub-criteria weights (0.4737*0.1+0.4737*0.0423 = 0.0674).

6.2.3.2 TOPSIS and VIKOR Ranking

The TOPSIS and VIKOR ranking were calculated using the weights for the selection criteria, Table 6.12, and table of alternative values, Table 6.13. The remaining values used

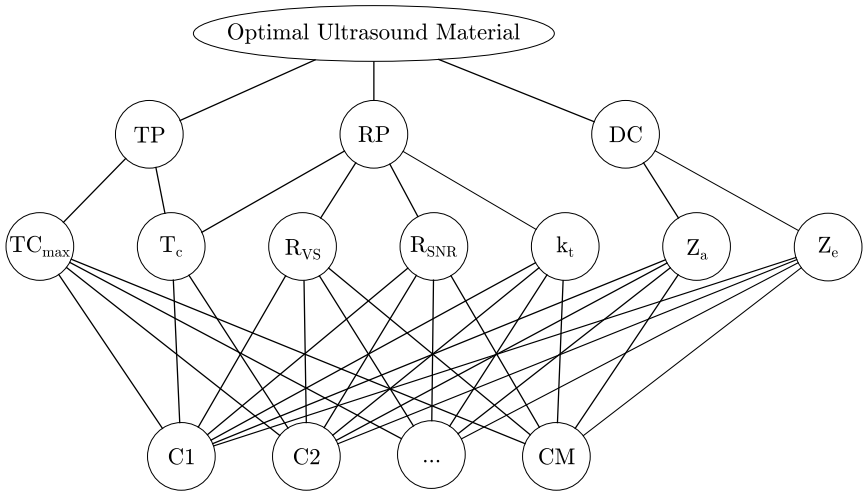

Figure 6.6: Decision hierarchy of the ultrasound material selection, where TP is transmitter performance, RP is receiver performance, DC is decision complexity, TC_{max} is the maximum transmission coefficient, T_c is the curie temperature, R_{VS} is the receiver voltage sensitivity, R_{SNR} is the receiver signal-to-noise ratio, k_t is the transducer thickness coupling, Z_a is the number of matching layers and Z_e is electronic matching.

Table 6.11: Pairwise comparison matrices of ultrasound criteria and sub-criteria.

Criteria comparison

	TP	RP	DC	Weights
TP	1	1	9	0.4737
RP	1	1	9	0.4737
DC	1/9	1/9	1	0.0526

Consistent (CR = 0)

Transducer performance sub-criteria comparison

	TC_{max}	T_c	Weights
TC_{max}	1	9	0.9
T_c	1/9	1	0.1

Receiver performance sub-criteria comparison

	k_t	R_{VS}	R_{SNR}	T_c	Weights
k_t	1	5	1	9	0.4296
R_{VS}	1/5	1	1/5	3	0.0985
R_{SNR}	1	5	1	9	0.4296
T_c	1/9	1/3	1/9	1	0.0423

Consistent (CR = 0.0120)

Design complexity sub-criteria comparison

	Z_a	Z_e	Weights
Z_a	1	1	0.5
Z_e	1	1	0.5

Table 6.12: AHP generated weights for ultrasound material selection

	TC_{max}	T_c	k_t	R_{VS}	R_{SNR}	Z_a	Z_e
Weights	0.4263	0.0674	0.2035	0.0467	0.2035	0.0263	0.0263
Design objective	max	max	max	max	max	min	min

in the calculation of the selection criteria can be found in Appendix B. Many different piezoelectric values lacked too many coefficients and were omitted, such as Quartz, $PbTiO_3$, CdS, GaN and ZnO.

Table 6.13: Alternative material values and criteria. **Bold = estimated through piezoelectric equations**.

#	Material	ϵ_{33}^S –	s_{33}^E [pm^2/N]	s_{33}^D [pm^2/N]	c_{33}^D [10^{10} N/m^2]	TC_{max} –	T_c [C]	k_t –	R_{VS} –	R_{SNR} –	Z_a –	Z_e –
1	$LiNbO_3$ (36° Rotated Y-cut)	27.9	5.026	4.89	**20.4**	0.0625	1150	0.485	**6.83E-02**	1E-05	3.40E07	3.94E09
2	AlN	10	2.824	**2.7**	**37**	0.0011	1000	0.065	**1.1E-02**	2E-05	1.61E07	9.50E09
3	PZT 5A	830	18.8	9.46	14.7	0.064	365	0.49	1.5E-02	3E-05	3.37E07	6.65E07
4	PZT 4	635	15.5	7.9	15.9	0.070	328	0.51	1.7E-02	5E-05	3.45E07	8.69E07
5	PZT 8	600	13.9	8.5	**12**	0.051	300	0.44	**1.8E-02**	4E-05	3.50E07	1.13E08
6	PZT 5H	1470	20.7	8.99	15.7	0.0681	193	0.505	1.12E-02	3E-05	3.420E07	3.32E07
7	PIN33%-PMN-PT (2nd Gen)	905	56.15	11.52	15.97	0.079	**85***	0.54	1.5E-02	1E-04	3.721E07	2.49E07
8	PIN24%-PMN-PT (2nd Gen)	868	49.04	9.78	16.49	0.067	**95***	0.50	1.4E-02	1E-04	3.71E07	2.47E07
9	PMN-32%PT Type A	700	49.18	6.82	15.77	0.11	**108***	0.62	2.0E-02	1E-04	3.73E07	1.61E07
10	PMN-28%PT Type A	895	36.15	7.06	16.66	0.099	**125***	0.60	1.7E-02	9E-05	3.73E07	2.05E07
11	P(VDF-TrFE) 75/25	**7.8**	300	**296**	**0.34**	0.017	119.8	0.262	**5.4E-01**	1.2E-05	4.51E06	1.43E10
12	$BaTiO_3$	1260	9.5	7.1	**14**	0.037	115	0.38	**9.6E-03**	2E-05	3.29E07	6.65E07
13	P(VDF-TrFE)	**10**	**300**	**259**	**0.39**	**0.0076**	100	**0.17**	**2.9E-01**	2.2E-05	4.6E06	9.42E09
14	PVDF	**11**	**472**	**438**	**0.23**	**0.0021**	90	**0.092**	**1.9E-01**	1.5E-05	4.0E06	9.42E09
15	PVDF	**7.3**	472	**455**	**0.22**	0.0054	**90**	0.146	**3.9E-01**	7.83E-06	3.92E06	1.49E10

* - using T_{RT}

Table 6.14: Ultrasound MCDM ranking results for TOPSIS and VIKOR(v=0.5). **Bold = ranking partially based upon estimated values**.

		TOPSIS				VIKOR			
#	Name	S^*	S^-	C^*	Rank	S	R	Q	Rank
14	**PVDF**	**0.2279**	**0.0166**	**0.0677**	**15**	**0.5931**	**0.2680**	**0.9968**	**15**
2	**AlN**	**0.2262**	**0.0394**	**0.1484**	**12**	**0.5749**	**0.2695**	**0.9819**	**14**
15	**PVDF**	**0.2229**	**0.0278**	**0.1109**	**14**	**0.5793**	**0.2632**	**0.9724**	**13**
13	**P(VDF-TrFE)**	**0.2136**	**0.0296**	**0.1218**	**13**	**0.5616**	**0.2598**	**0.9476**	**12**
11	**P(VDF-TrFE) 75/25**	**0.1992**	**0.0508**	**0.2031**	**11**	**0.5249**	**0.2448**	**0.8783**	**11**
12	**$BaTiO_3$**	**0.1652**	**0.0784**	**0.3219**	**10**	**0.4845**	**0.2082**	**0.7578**	**10**
5	**PZT 8**	**0.1327**	**0.1079**	**0.4485**	**9**	**0.4144**	**0.1783**	**0.6226**	**9**
1	**$LiNbO_3$ (36° Rotated Y-cut)**	**0.1266**	**0.1312**	**0.5089**	**8**	**0.3707**	**0.1507**	**0.5186**	**8**
3	PZT 5A	0.1176	0.1292	0.5235	7	0.3777	0.1469	0.5172	7
6	PZT 5H	0.1144	0.1363	0.5436	6	0.3676	0.1362	0.4836	6
4	PZT 4	0.0999	0.1440	0.5905	5	0.3343	0.1311	0.4393	5
8	**PIN24%-PMN-PT (2nd Gen)**	**0.0965**	**0.1588**	**0.6221**	**4**	**0.2672**	**0.1391**	**0.3905**	**4**
7	**PIN33%-PMN-PT (2nd Gen)**	**0.0791**	**0.1776**	**0.6912**	**3**	**0.2192**	**0.1056**	**0.2694**	**3**
10	**PMN-28%PT Type A**	**0.0576**	**0.2064**	**0.7819**	**2**	**0.1570**	**0.0421**	**0.0682**	**2**
9	**PMN-32%PT Type A**	**0.0535**	**0.2282**	**0.8101**	**1**	**0.0882**	**0.0424**	**0.0007**	**1**

The ranking for TOPSIS and VIKOR are shown in Table 6.14. TOPSIS and VIKOR both gave similar rankings until ranks greater than 11. VIKOR indicated the solution consisted of three alternatives 9, 10 and 7. The reason for the three alternatives is that one of the VIKOR ranking condition was not met. Specifically, the top ranked alternative, 9, did not have an acceptable advantage over 10 or 7. This can be confirmed by looking at the TOPSIS top three alternatives.

From the ranking results, the relaxor ferroelectrics single crystals seem to have an advantage over all other materials. Experimentally, relaxor ferroelectrics have shown to have increased sensitivity (5 dB) and bandwidth (25%) over the equivalent PZT[241]. Relaxors ferroelectric ultrasound transducers have gained commercial acceptance as well [253]. Thus, the material selection criteria, weighting and material selection was consistent with academic and industrial results.

6.3 Selection Criteria Issues

Throughout the material selection, a nascent issue has been identified that reduces the confidence of the results of this process. In the collection of data from vendors which the author assumed to be more consistent, it became evident that there was some problems with this assumption as:

- some vendors, such as Boston Piezo-Optics [254], would use material constants determined in articles (where s^D, g_{22}, g_{31}, g_{33}, h_{22}, h_{31} and h_{33} came from Warner et al. [255] and s^E, d, c^E constants came from Smith and Welsh [256]),
- manufacturers, such as CTS Corporation [257], would use theoretical calculations of values to fill holes in data,
- in both these cases, there was no mention of the material constant variation, such as the manufacturer tolerance Noliac indicates in their documentation [30],

- lastly, in some cases vendor cited values and what is received is quite different (Emfit published value of d_{33} without preaging [81] was ≈300% percent error (using the conservative d_{33} value of 250 pC/N) compared to experimental results (≈60 pC/N) [258] — which begs the question, why if they knew aging was an issue not indicate the aged values as well) and PZN-PT single crystal values from Microfine Materials Technology Pte. Ltd. showed a 20% difference within the received samples [221].

Therefore, the designer must accept that the published values of some vendors and manufacturers are not sacrosanct. It can have significant uncertainty because the data comes from multiple different sources (like Boston Piezo-Optics [254]), is calculated from a set of values (like the CTS Brochure [257]), no indication of manufacturing tolerances, a possible cherry-picking of optimal values — Dynalloy, an SMA manufacturer, seems incapable of clearly quantifying fatigue life [132] — and sample-to sample variation such as 5% for PZT or 20% for relaxor ferroelectrics. Yet as technology designer generally have little financial resource to perform a material property study on the material used in a selection method, there is not much one can do except ensure that one does not further the practice. When publishing values that are calculated, estimated or taken from different resources, it should be clearly **indicated**.

6.4 Summary and Comments

In this chapter, the AHP+MCDM method was used to select the optimal material for a resonant cantilever energy harvester and a piezoelectric ultrasound transducer. Using the AHP process, it was possible to identify the weights for different criteria and sub-criteria through pairwise comparisons. Using both TOPSIS and VIKOR, the result would be ranked based upon the weights generated by the pairwise comparison. Thus, not only did the process provide a material selection but it also provided clarity in the selection process, since the weighting between different criteria and sub-criteria.

In the first example, PZT 8 was greatly preferred over the other alternatives. In the second example, the ultrasound selection had a large number of criteria. The results indicated that relaxor ferroelectrics were the best material based upon the designer-defined weights and was shown to be consistent with literature and experimentation.

Lastly, the discussion of the issues with material selection indicate that a fastidious designer should be careful of what values and where those values come from, but, aside from measuring all the values, the designer is stuck dealing with a large amount of uncertainty.

Chapter 7

Conclusions and Future Work

The objective of this thesis was to identify a method for a designer to select an optimal active material based upon their application.

In an effort to do this, the three most researched active materials (piezoelectrics, magnetostrictives and shape memory alloys) were discussed with emphasis on creating a phenomenological understanding of the material and the practical limitations that have been discovered in their application.

In the Ashby's material selection method, the designer would be able to select all materials based upon a set of generalized coefficients, a definition of the function, the constraints and the optimizing objective of the device. In active material transducers, the same frame for material selection can be used but the set of coefficients that designers have is domain-dependent, and this dependence introduces issues when comparing different active material families. To address this problem it is common practice to use a set of generalized figures of merit to dictate which material should be selected. In the case of actuators, the generalized metrics are energy density, power density and efficiency provide some guidance to the selection but are fraught with simplifications that need to be understood. To address these simplifications, the designer requires a larger set of data for each material. Yet the increased number of comparisons, introduces complexity in the decision making process. To resolve this complexity a formalized decision making process called analytic hierarchy process (AHP) and two multi-criteria decision making (MCDM) methods, TOPSIS and VIKOR, are employed. AHP is utilized to simplify, and clarify, the process of assigning importance to different tangible and intangible criteria. Afterwards, the ranking of different materials is performed by TOPSIS and VIKOR.

The AHP+MCDM method was used for optimal material selection for resonant cantilever energy harvester and an ultrasound transducer. In the first case, the high power output and efficiency of PZT 8 makes it an excellent choice. PZT 8 has a high mechanical quality factor which results in it being selected. This selection is dependent upon the fact that coupling coefficient and quality factor can be assumed to be only dependent upon the material properties. In the second case, a few relaxor ferroelectric single crystals were deemed to be the optimal material over PZTs. Similarly, experimental verification indicated that the relaxor single crystals had a significantly better sensor parameters than

PZTs. The reason for the improved performance is there extremely high coupling coefficient which results in high transmission coefficient and bandwidth at the expense of a low receiver voltage sensitivity, receiver signal-to-noise ratio and curie temperature. The low curie temperature has been an issue for some ultrasound manufacturing and ideally the third generation relaxor ferroelectric crystals, which have a high curie temperature, would likely be used. Unfortunately, third generation relaxor ferroelectric single crystals are not commercially available, and academic sources lack important material properties, so they were omitted from the analysis.

Unfortunately, at the end of this work another issue was identified, which is how trustworthy is the material data. Published values from scholars are subject to part-to-part, batch-to-batch variation and possible experimental errors, so they will have significant noise. Most vendors and manufacturers are likely more concerned with being solvent than the stating the statistical fluctuation in their manufacturing. In an ideal selection method, the designer would be able to state at different levels of confidence which materials could be optimal and thus a new VIKOR algorithm should be created which would suggest materials based upon the confidence required (TOPSIS does not suggest a solution set of alternatives). To do this properly an understanding of what causes the driving force for material variation, which would be an arduous task at best, but at least making the algorithm and assuming normal distributions would be a start.

Furthermore, more work should be done to improve the selection using the hybrid AHP+MDCM method through adjusting the pairwise comparison process, using fuzzy weights to reduce subjectivity and applying a sensitivity analysis. While the pairwise comparison used a scale of absolute numbers, there are many different ways that the pairwise comparison can be adjusted. For example, the spacing between moderate to equal importance results in a ratio of 3:1 but the ratio between very strong and extreme importance (9:7) is much smaller. In reality, there should be an equal ratio between orders of preference or more weight applied to the stronger preferences. Selection can also be improved by using a fuzzy set theory at the cost of clarity. In classical MCDM methods, the decision maker uses crisp values for weights but fuzzy set theory allows for uncertainty in judgments. The fuzzy MCDM method can account for the vagueness and imprecision of the pairwise comparison process but the values no longer exactly represent the linguistic values selected. Lastly, it would be important to see how variations in the decision makers selection affects the ranking of alternatives, which is called sensitivity analysis. Sensitivity analysis, which consists of varying an independent weights to see the change in ranking, increases the complexity of the decision making process but provides increased information to ensure that the decision maker can make a more informed decision.

Although the trustworthiness of the data lowers the confidence of the optimal material selection process, the designer who follows this method is more likely to select what is optimal. With some further work, the hybrid AHP+MCDM material selection process could be more accurate and the decision maker could have more confidence in the selection. Excluding the literature review to determine the proper figures of merit, the material selection process not only selects effective material but it does not take much time once the somewhat steep learning curve is surmounted.

References

[1] M. Ahsby, T. Davies, and S. Gorsse, "The CES EduPack DB for Bulk Functional Materials," tech. rep., Granta Teaching Resources, 2015.

[2] D. C. Lagoudas, *Shape Memory Alloys*. Springer US, 2008.

[3] A. McWillims, "Smart Materials and Their Applications: Technologies and Global Markets," tech. rep., BCC Research Advanced Materials Reports, 2015.

[4] Y. Bar-Cohen, *Electroactive Polymer (EAP) Actuators as Artificial Muscles*. SPIE–The International Society for Optical Engineering, 2004.

[5] F. Li, L. Jin, Z. Xu, and S. Zhang, "Electrostrictive effect in ferroelectrics: An alternative approach to improve piezoelectricity," *Applied Physics Reviews*, vol. 1, no. 1, 2014.

[6] A. E. Clark and H. S. Belson, "Giant Room-Temperature Magnetostrictions in $TbFe_2$ and $DyFe_2$," *Physical Review B*, vol. 5, no. 9, pp. 3642–3644, 1972.

[7] J. Curie and P. Curie, "Développement, par pression, de l'électricité polaire dans les cristaux hémièdres à faces inclinées," *Comptes rendus de l'Académie des Sciences*, 1880.

[8] J. Tichý *et al.*, *Fundemantals of Piezoelectric Sensorics*. Springer-Verlag Berlin Heidelberg, 2010.

[9] "Piezoelectric Engineering Tutorial," tech. rep., Aerotech Inc.

[10] J. L. Pons, *Emerging Actuator Technologies: A Micromechatronic Approach*. Wiley, 2005.

[11] J. Glaum and M. Hoffman, "Electric Fatigue of Lead-Free Piezoelectric Materials," *Journal of American Ceramic Society*, vol. 97, no. 3, pp. 665–680, 2014.

[12] K. C. Kao, *Dielectric Phenomena in Solids*. Elsevier Academic Press, 2004.

[13] C.-H. Hong *et al.*, "Lead-free piezoceramics – where to move on?," *Journal of Materiomics*, vol. 2, pp. 1–24, 2016.

[14] S.-E. Park and T. R. Shrout, "Ultrahigh strain and piezoelectric behavior in relaxor based ferroelectric single crystals," *Journal of Applied Physics*, vol. 82, 1997.

[15] K. L. Walter Heywang and W. Wersing, *Piezoelectricity: Evolution and Future of a Technology*. Springer-Verlag Berlin Heidelberg, 2008.

[16] B. Jaffe, W. R. Cook, and H. Jaffe, *Piezoelectric Ceramics*. Academic Press Inc., 1971.

[17] L. Y. et al., "Novel polymer ferroelectric behavior via crystal isomorphism and the nanoconfinement effect," *Polymer*, vol. 54, 2013.

[18] R. C. Smith, *Smart Material Systems*. Society for Industrial and Applied Mathematics (SIAM), 2005.

[19] M. Goldfarb and N. Celanovic, "Modeling Piezoelectric Stack Actuators for Control of Micromanipulation," *IEEE Control Systems Magazine*, pp. 69–79, 1997.

[20] M. Quant *et al.*, "A comprehensive model for piezoceramic actuators: modelling, validation and application," *Smart Materials and Structures*, vol. 18, no. 12, 2009.

[21] A. Pramanick *et al.*, "Origins of Electro-Mechanical Coupling in Polycrystalline Ferroelectrics During Subcoercive Electrical Loading," *Journal of the American Ceramic Society*, vol. 94, no. 2, 2011.

[22] S. Zhang and F. Li, "High performance ferroelectric relaxor-$PbTiO_3$ single crystals: Status and Perspective," *Journal of Applied Physics*, vol. 111, 2012.

[23] C. S. Lynch, "The Effect of Uniaxial Stress on the Electro-Mechanical Response of 8/65/35 PLZT," *Acta Materialia*, vol. 44, no. 11, 1996.

[24] K. Sakayori *et al.*, "Curie Temperature of $BaTiO_3$," *Japanese Journal of Applied Physics*, vol. 34, 1995.

[25] C. A. Randall *et al.*, "Intrinsic and Extrinsic Size Effects in Fine-Grained Morphotropic-Phase-Boundary Lead Zirconate Titanate Ceramics," *Journal of American Ceramic Society*, vol. 81, no. 3, 1998.

[26] "Piezoelectric Ceramic Material and Measurements Guidelines for Sonar Transducers," *MIL-STD-1376B(SH)*, 1995.

[27] T. R. Shrout and S. J. Zhang, "Lead-free piezoelectric ceramics: Alternatives for PZT?," *Journal of Electroceramics*, vol. 19, 2007. Springer Nature.

[28] W. Jo *et al.*, "Giant electric-field-induced strains in lead-free ceramics for actuator applications – status and perspective," *Journal of Electroceramics*, vol. 29, 2012.

[29] D. A. DeAngelis and G. W. Schulze, "Performance of PZT8 versus PZT4 piezoceramic materials in ultrasonic transducers," *Physics Procedia*, vol. 87, pp. 85–92, 2016.

[30] "Noliac Piezoelectric Materials." http://www.noliac.com/products/materials/, 2013. [Online; accessed 2017/09/22.

[31] H. Jaffe and D. A. Berlincourt, "Piezoelectric Transducer Materials," *Proceedings of the IRE*, vol. 53, 1965.

[32] P. Srinivasan and S. M. Spearing, "Optimal materials selection for bimaterial piezoelectric microactuators," *JOURNAL OF MICROELECTROMECHANICAL SYSTEMS*, vol. 17, 2008.

[33] S. Tadigadapa and K. Mateti, "Piezoelectric MEMS sensors: state-of-the-art and perspectives," *Measurement science and technology*, vol. 20, 2009.

[34] J. Rödel *et al.*, "Transferring lead-free piezoelectric ceramics into application," *Journal of European Ceramic Society*, vol. 35, 2015.

[35] W. Soluch, E. Brzozowski, M. Lysakowska, and J. Sadura, "Determination of Mass Density, Dielectric, Elastic, and Piezoelectric Constants of Bulk GaN Crystal," *IEEE Transactions on Ultrasonics, Ferroelectrics, and Frequency Control*, vol. 58, 2011.

[36] R. C. Turner, P. A. Fuierer, R. E. Newnham, and T. R. Shrout, "Materials for High Temperature Acoustic and Vibration Sensors: A Review," *Applied Acoustics*, vol. 41, pp. 299–324, 1994.

[37] M. Otonicar, A. Reichmann, and K. Reichmann, "Electric field-induced changes of domain structure and properties in La-doped PZT–From ferroelectrics towards relaxors," *Journal of the European Ceramic Society*, vol. 36, 2016.

[38] I. Kerkamm *et al.*, "Correlation of small- and large-signal properties of lead zirconate titanate multilayer actuators," *Acta Materialia*, vol. 57, 2009.

[39] R. A. Cowley *et al.*, "Relaxing with relaxors: a review of relaxors," *Advances in Physics*, vol. 60, no. 2, 2011.

[40] L. E. Cross, "Relaxor Ferroelectrics," *Ferroelectrics*, vol. 76, 1987.

[41] E. V. Colla, N. K. Yushin, and D. Viehland, "Dielectric properties of $(PMN)_{(1-x)}(PT)_x$ single crystals for various electrical and thermal histories," *Journal of Applied Physics*, vol. 83, no. 6, 1998.

[42] K. Uchino, *Advanced Piezoelectric Materials: Science and Technology*. Woodhead Publishing, 2010.

[43] D. Damjanovic and R. E. Newnham, "Electrostrictive and Piezoelectric Materials for Actuator Applications," *Journal of Intelligent Material Systems and Structures*, 1992.

[44] The Tool Hub, "Understanding shrinkage rates." http://thetoolhub.com/part-design/shrink/. [Online; accessed 2017/10/27].

[45] E. K. Akdogan, M. Allahverdi, and A. Safari, "Piezoelectric Composites for Sensor and Actuator Applications," *IEEE Transactions on Ultrasonics, Ferroelectrics, and Frequency Control*, vol. 52, 2005.

[46] K. S. Ramadan, D. Sameoto, and S. Evoy, "A review of piezoelectric polymers as functional materials for electromechanical transducers," *Smart Materials and Structures*, vol. 23, 2014.

[47] M. S. Vijaya, *Piezoelectric Materials and Devices*. CRC Press, 2012.

[48] B. Chu *et al.*, "A Dielectric Polymer with High Electric Energy Density and Fast Discharge Speed," *Science*, vol. 313, 2006.

[49] A. J. Lovinger, "Ferroelectric Polymers," *Science*, vol. 220, no. 4602, 1983.

[50] Q. Li and Q. Wang, "Ferroelectric Polymers and Their Energy-Related Applications," *Macromolecular Chemistry and Physics*, vol. 217, 2016.

[51] C. Wan and C. R. Bowen, "Multiscale-structuring of polyvinylidene fluoride for energy harvesting: the impact of molecular-, micro- and macro-structure," *Journal of Materials Chemistry A*, vol. 5, 2017.

[52] T. Furukawa, "Ferroelectric properties of vinylidene fluoride copolymers," *Phase Transitions*, 1989.

[53] V. Sencadas, R. Gregorio, JR., and S. Lanceros-Méndez, "α to β Phase Transformation and Microestructural Changes of PVDF Films Induced by Uniaxial Stretch," *Journal of Macromolecular Science Part B: Science*, vol. 48, 2009.

[54] Q. M. Zhang, V. Bharti, and X. Zhao, "Giant Electrostriction and Relaxor Ferroelectric Behavior in Electron-Irradiated Poly(vinylidene fluoride-trifluoroethylene) Copolymer," *Science*, vol. 280, 1998.

[55] M. R. Gadinski *et al.*, "Understanding of Relaxor Ferroelectric Behavior of Poly (vinylidene fluoride-trifluoroethylene-chlorotrifluoroethylene) Terpolymers," *Macromolecules*, vol. 48, pp. 2731–2739, 2015.

[56] L. F. Brown *et al.*, "Ferroelectric Nylon Materials and Their Feasibility for Ultrasound Transducers," *IEEE Transactions on Ultrasonics, Ferroelectrics, and Frequency Control*, vol. 44, 1997.

[57] "Piezoelectric Films: Technical Information." http://www.piezotech.eu/export/sites/piezotech/.content/medias/downloads/Piezotech-leaflet-Feb-2015.pdf. [Online; accessed 2017/10/27].

[58] T. R. Dargaville and others., "Characterization, Performance and Optimization of PVDF as a Piezoelectric Film for Advanced Space Mirror Concepts," tech. rep., Sandia National Laboratories, 2005.

[59] W. Xia, Z. Xu, Z. Zhang, and H. Li, "Dielectric, piezoelectric and ferroelectric properties of a poly (vinylidene fluoride-co-trifluoroethylene) synthesized via a hydrogenation process," *Polymer*, vol. 54, pp. 440–446, 2013.

[60] H. Taunaumang, I. L. Guy, and H. L. W. Chan, "Electromechanical properties of 1-3 piezoelectric ceramic/piezoelectric polymer composites," *Journal of Applied Physics*, vol. 76, pp. 484–489, 1993.

[61] R. E. Newnham, D. Skinner, and L. Cross, "Connectivity and piezoelectric-pyroelectric composites," *Materials Research Bulletin*, vol. 13, no. 5, 1978.

[62] H. J. Lee, S. Zhang, Y. Bar-Cohen, and S. Sherrit, "High Temperature, High Power Piezoelectric Composite Transducers," *Sensors*, vol. 14, 2014.

[63] C. Liu *et al.*, "Micromachined High Frequency PMN-PT/Epoxy 1-3 Composite Ultrasonic Annular Arrays," in *2010 IEEE International Ultrasonics Symposium Proceedings*, 2010.

[64] Y. Zhang *et al.*, "Fabrication of angle beam two-element ultrasonic transducers with PMN–PT single crystal and PMN–PT/epoxy 1–3 composite for NDE applications," *Sensors and Actuators A*, vol. 168, 2011.

[65] D. Zhou *et al.*, "Fabrication and Performance of Endoscopic Ultrasound Radial Arrays Based on PMN-PT Single Crystal/Epoxy 1-3 Composite," *IEEE Transactions on Ultrasonics, Ferroelectrics, and Frequency Control*, vol. 58, 2011.

[66] A. A. Bent, *Active Fiber Composite for Structural Applications.* PhD thesis, Massachusetts Institute of Technology, 1997.

[67] W. K. Wilkie *et al.*, "Low-Cost Piezocomposite Actuator for Structural Control Applications," in *Proceedings of SPIE Vol. 3991*, Smart Structures and Materials 2000: Industrial and Commercial Applications of Smart Structures Technologies, 2000.

[68] H. A. Sodano, G. Park, and D. J. Inman, "An investigation into the performance of macro-fiber composites for sensing and structural vibration applications," *Mechanical Systems and Signal Processing*, vol. 18, 2004.

[69] H. J. Song *et al.*, "Energy Harvesting Devices Using Macro-fiber Composite Materials," *Journal of Intelligent Material Systems and Structures*, 2010.

[70] R. B. Williams, G. Park, D. J. Inman, and W. K. Wilkie, "An overview of composite actuators with piezoceramic fibers," Proceedings of 20th International Modal Analysis Conference, 2002.

[71] S. Huang *et al.*, "Preparation and polarization of 0–3 cement based piezoelectric composites," *Materials Research Bulletin*, vol. 41, 2006.

[72] Y. J. Choi *et al.*, "Dielectric and piezoelectric properties of ceramic-polymer composites with 0–3 connectivity type," *Journal of Electroceramics*, vol. 30, 2013.

[73] M. T. Sebastian and H. Jantunen, "Polymer–Ceramic Composites of 0–3 Connectivity for Circuits in Electronics: A Review," *International Journal of Applied Ceramic Technology*, vol. 7, no. 4, 2010.

[74] F. Z. Wang, H. Wang, H. J. Sun, and S. G. Hu, "Research on a 0–3 cement-based piezoelectric sensor with excellent mechanical–electrical response and good durability," *Smart Materials and Structures*, vol. 23, 2014.

[75] R. Rianyoi *et al.*, "Dielectric, ferroelectric and piezoelectric properties of 0-3 barium titanateâĂŞPortland cement composites," *Applied Physics A*, vol. 104, 2011.

[76] R. Gerhard-Multhaupt, "Less can be More Holes in Polymers lead to a New Paradigm of Piezoelectric Materials for Electret Transducers," *IEEE Transactions on Dielectrics and Electrical Insulation*, vol. 9, 2002.

[77] F. Carpi, *Electromechanically Active Polymers*. Springer International Publishing AG Switzerland, 2016.

[78] S. Bauer, "Piezo-, pyro- and Ferroelectrets: Soft Transducer Materials for Electromechanical Energy Conversion," *IEEE Transactions on Dielectrics and Electrical Insulation*, vol. 13, 2006.

[79] M. Matysek, P. Lotz, and H. F. Schlaak, "Lifetime Investigation of Dielectric Elastomer Stack Actuators," *IEEE Transactions on Dielectrics and Electrical Insulation*, vol. 18, 2011.

[80] A. Mohebbi, F. Mighri, A. Ajji, and D. Rodrigue, "Cellular Polymer Ferroelectret: A Review on Their Development and Their Piezoelectric Properties," *Advances in Polymer Technology*, vol. 0, 2016.

[81] "Electroactive Ferroelectret (≈ Ferroelectric) Sensor Film - Emfit." https://www.emfit.com/electroactive-ferroelectret-film. [Online; Accessed 2017/09/27].

[82] X. Zhang, J. Hillenbrand, and G. M. Sessler, "Ferroelectrets with improved thermal stability made from fused fluorocarbon layers," *Journal of Applied Physics*, vol. 101, 2007.

[83] S. Kärki and J. Lekkala, "A lumped-parameter transducer model for piezoelectric and ferroelectret polymers," *Measurement*, vol. 45, pp. 453–458, 2012.

[84] "Piezoelectric actuators," tech. rep., Physik Instrumente Ceramic GmbH, 2016. PI CAT128E R3.

[85] D. R. Brandt *et al.*, "Mechanical constitutive behavior and exceptional blocking force of lead-free BZT-xBCT piezoceramics," *Journal of Applied Physics*, vol. 115, 2014.

[86] J. Koruza *et al.*, "Enhancing the operational range of piezoelectric actuators by uniaxial compressive preloading," *Journal of Applied Physics D: Applied Physics*, vol. 48, 2015.

[87] R. Dittmer *et al.*, "Optimal working regime of lead–zirconate–titanate for actuation applications," *Sensors and Actuators A*, vol. 189, pp. 187–194, 2013.

[88] A. J. Fleming and K. K. Leang, *Design, Modeling and Control of Nanopositioning Systems*. Springer Nature, 2014.

[89] I. D. Mayergoyz and G. Bertotti, *The Science of Hysteresis*, ch. Hysteresis in Piezoelectric and Ferroelectric Materials. Academic Press, 2005.

[90] K. Uchino and S. Hirose, "Loss Mechanisms in Piezoelectrics: How to Measure Different Losses Separately," *IEEE Transactions in Ultrasonics, Ferroelectrics, and Frequency Control*, 2001.

[91] K. Uchino *et al.*, "Loss mechanism and high power piezoelectrics," *Journal of Materials Science*, vol. 41, pp. 217–228, 2006.

[92] H. Kungl and M. J. Hoffmann, "Method for the estimation of the total displacement of ferroelectric actuators under mixed thermal and electrical loading," *Sensors and Actuators A*, vol. 144, 2008.

[93] J. Rödel and et al., "Perspective on the Development of Lead-free Piezoceramics," *Journal of the American Ceramic Society*, vol. 92, no. 6, 2009.

[94] O. Mack, "Investigations of piezoelectric force measuring devices for use in legal weighing metrology," tech. rep., Physikalisch-Technische Bundesanstalt (PTB), 2005.

[95] J. P. Joule, "On the Effects of Magnetism upon the Dimensions of Iron and Steel Bars," *The London, Edinburgh and Dublin Philosophical Magazine and Journal of Science*, 1847.

[96] J. Atulasimha and A. B. Flatau, "A review of magnetostrictive iron–gallium alloys," *Smart Materials and Structures*, vol. 20, 2011.

[97] A. G. Jenner, R. J. E. Smith, A. J. Wilkinson, and R. Greenough, "Actuation and transduction by giant magnetostrictive alloys," *Mechatronics*, vol. 10, 2000.

[98] F. Claeyssen, N. Lhermet, and T. Maillard, "Magnetostrictive Actuators Compared to Piezoelectric Actuators," tech. rep., Cedrat Technologies, 2002.

[99] S. Karunanidhi and M. Singaperumal, "Design, analysis and simulation of magnetostrictive actuator and its application to high dynamic servo valve," *Senors and Actuators A*, vol. 157, pp. 185–197, 2010.

[100] A.-G. Olabi and A. Grunwald, "Design and Application of Magnetostrictive Materials," *Materials and Design*, vol. 29, 2008.

[101] Z.-Y. Jia, H.-F. Liu, F.-J. Wang, and C.-Y. Ge, "Research on a novel force sensor based on giant magnetostrictive material and its model," *Journal of Alloys and Compounds*, vol. 509, 2011.

[102] M. Ghodsi *et al.*, "Analytical, numerical and experimental investigation of a giant magnetostrictive (GM) force sensor," *Sensor Review*, vol. 35, no. 4, 2016. SPIE 9800, Behavior and Mechanics of Multifunctional Materials and Composites.

[103] "Magnetostriction: Basic physical elements," tech. rep., MTS Sensors Group, 2005.

[104] V. Berbyuk, "Vibration energy harvesting using Galfenol based transducer," in *Proceedings of SPIE 8688*, Active and Passive Smart Structures and Integrated Systems, 2013.

[105] S. Chikazumi, *Physics of Ferromagnetism*. Oxford University Press, 1997.

[106] A. Goldman, *Handbook of Modern Ferromagnetic Materials*. Kluwer Academic Publishers, 1999.

[107] K. Linnemann, S. Klinkel, and W. Wagner, "A constitutive model for magnetostrictive and piezoelectric materials," *International Journal of Solids and Structures*, vol. 46, p. 1151, 2009.

[108] "IEEE Standard on Magnetostrictive Materials: Piezomagnetic Nomenclature," *IEEE Std. 319-1971*, pp. 67–76, 1973.

[109] S. Chakrabarti, *Modeling of 3D Magnetostrictive Systems with Application to Galfenol and Terfenol-D Transducers*. PhD thesis, The Ohio State University, 2011.

[110] K. C. Pitman, "The influence of stress on ferromagnetic hysteresis," *IEEE Transaction on Magnetics*, vol. 26, 1990.

[111] D. C. Jiles, "Theory of Magnetomechanical Effect," *Journal of Physics D: Applied Physics*, vol. 28, no. 8, 1995.

[112] A. Grunwald and A.-G. Olabi, "Design of a Magnetostrictive (MS) Actuator," *Sensors and Actuators A*, vol. 144, pp. 161–175, 2008.

[113] "TdVib LLC Terfenol-D - ETREMA Products Inc.." http://tdvib.com/terfenol-d/, 2016. [Online; accessed 2017/02/15].

[114] "TdVib LLC Galfenol - ETREMA Products Inc.." http://tdvib.com/galfenol/, 2016. [Online; accessed 2017/02/15].

[115] T. Ueno and T. Higuchi, "Magnetic Circuit for Stress-Based Magnetic Force Control Using Iron-Gallium Alloy," *IEEE Transactions on Magnetics*, vol. 43, no. 6, 2007.

[116] E. Summers, "Galfenol – A New Class of Magnetostrictive Materials." http://www.tdvib.com/wp-content/uploads/2015/07/Galfenol-Public-Release_v7edit1.pdf, 2015. [Online; accesed 2017/09/28].

[117] Z. Deng and M. J. Dapino, "Magnetic flux biasing of magnetostrictive sensors," *Smart Materials and Structures*, vol. 26, 2017.

[118] J. Slaughter, E. Summers, and J. Snodgrass, "Comparison of transduction behavior of polycrystalline gallium-iron alloys and Terfenol-D," Smart Structures and Materials: Active Materials: Behavior and Mechanics, Proceedings of SPIE 5387, 2004.

[119] M. J. Dapino, R. C. Smith, and A. B. Flatau, "A model for the ΔE Effect in Magnetostrictive Transducers," tech. rep., North Carolina State University, 2000.

[120] H. Janocha, *Adaptronics and Smart Structures*. Springer-Verlag Berlin, 2007.

[121] M. Sheykholeslami *et al.*, "Investigation of ΔE Effect on Vibrational Behavior of Giant Magnetostrictive Transducers," *Shock and Vibration*, 2015.

[122] M. Ghodsi, M. Modabberifar, and T. Ueno, "Quality factor, static and dynamic responses of miniature galfenol actuator at wide range of temperature," *International Journal of the Physical Sciences*, vol. 6, 2011.

[123] F. T. Calkins, *Design, analysis, and modeling of giant magnetostrictuve transducers*. PhD thesis, Iowa State University, 1997.

[124] M. J. Dapino, F. T. Calkins, and A. B. Flatau, "On identification and analysis of fundamental issues in Terfenol-D transducer modeling," in *Proceedings of SPIE 3329*, Smart Materials and Structure 1998, 1998.

[125] F. T. Calkins, M. J. Dapino, and A. B. Flatau, "Effect of prestress on the dynamic performance of a Terfenol-D transducer," in *Proceedings of SPIE 3041*, Smart Structures and Materials, 1997.

[126] A. E. Clark, "High Power Rare Earth Magnetostrictive Materials," *Journal of Intelligent Material Systems and Structures*, vol. 4, 1993.

[127] Y.-K. Kwak, S.-H. Kim, and J.-H. Ahn, "Improvement of Positioning Accuracy of Magnetostrictive Actuator by Means of Built-in Air Cooling and Temperature Control," *International Journal of Precision Engineering and Manufacturing*, 2011.

[128] M. Ghodsi *et al.*, "Elimination of thermal instability in precise positioning of Galfenol actuators," in *Proceedings of SPIE 9800*, Behavior and Mechanics of Multifunctional Materials and Composites, 2016.

[129] C. M. Wayman and J. D. Harrison, "The origins of the shape memory effect," *The Journal of The Minerals, Metals & Materials Society*, 1989.

[130] J. M. Jani *et al.*, "A review of shape memory alloy research, applications and opportunities," *Materials and Design*, 2014.

[131] J. V. Humbeeck, "Shape Memory Alloys: A Material and a Technology," *Advanced Engineering Materials*, vol. 3, 2001.

[132] "Technical characteristics of flexinol actuator wires." http://www.dynalloy.com/pdfs/TCF1140.pdf. [Online; accessed 2017/07/21].

[133] D. W. Norwich and A. Fasching, "A Study of the Effect of Diameter on the Fatigue Properties of NiTi Wire," in *International Conference of Shape Memory and Superelastic Technologies*, 2009.

[134] "MigaOne DataSheet." http://www.migamotors.com/Media/MigaOneCutSheet.pdf. [Online; accessed 2017/07/21].

[135] B. Panton, *Laser Processing, Thermomechanical Processing, and Thermomechanical Fatigue of NiTi Shape Memory Alloys*. PhD thesis, University of Waterloo, 2016.

[136] K. Otsuka and X. Ren, "Physical metallurgy of Ti–Ni-based shape memory alloys," *Progress in Material Science*, pp. 511–678, 2005.

[137] Y. Liu and H. Yang, "Strain dependence of the ClausiusâĂŞClapeyron relation for thermoelastic martensitic transformations in NiTi," *Smart Materials and Structures*, vol. 16, 2007.

[138] "Measuring Transformation Temperatures in Nitinol Alloys." http://jmmedical.com/resources/211/Measuring-Transformation-Temperatures-in-Nitinol-Alloys.html. [Online; accessed 2017/08/03].

[139] J. Frenzel *et al.*, "Influence of Ni on martensitic phase transformations in NiTi shape memory alloys," *Acta Materialia*, vol. 58, 2010.

[140] Pelton, DiCello, and Miyazaki, "Optimization of Processing and Properties of Medical-Grade Nitinol Wire," tech. rep., NDC, 2000.

[141] C. Saikrishna *et al.*, "Enhancement in fatigue life of NiTi shape memory alloy thermal actuator wire," *Acta Materialia*, vol. 102, 2016.

[142] X. Wang, J. V. Humbeeck, B. Verlinden, and S. Kustov, "Thermal cycling induced room temperature aging effect in Ni-rich NiTi shape memory alloy," *Scripta Materialia*, vol. 113, 2016.

[143] K. C. Atli *et al.*, "The effect of training on two-way shape memory effect of binary NiTi and NiTi based ternary high temperature shape memory alloys," *Material Science and Engineering A*, vol. 560, 2013.

[144] K. Lygin, S. Langbein, P. Labenda, and T. Sadek, "A Methodology for the Development, Production, and Validation of R-Phase Actuators," *Journal of Materials Engineering and Performance*, vol. 21, 2012.

[145] X. B. Wang, B. Verlinden, and J. V. Humbeeck, "R-phase transformation in NiTi alloys," *Materials Science and Technology*, vol. 30, 2014.

[146] X. Wang, S. Kustov, B. Verlinden, and J. V. Humbeeck, "Fundamental Development on Utilizing the R-phase Transformation in NiTi Shape Memory Alloys," *Shape Memory Superelasticity*, vol. 1, 2015.

[147] C. Urbina, S. D. la Flor, and F. Ferrando, "R-phase influence on different two-way shape memory training methods in NiTi shape memory alloys," *Journal of Alloys and Compounds*, 2010.

[148] O. Benafan *et al.*, "Shape memory alloy actuator design: CASMART collaborative best practices and case studies," *International Journal Mechanical Material Design*, 2014.

[149] J. M. Jani, M. Leary, and A. Subic, "Designing shape memory alloy linear actuators: A review," *Journal of Intelligent Material Systems and Structures*, 2016.

[150] S. Barbarino and et. al., "A review on shape memory alloys with applications to morphing aircraft," *Smart Materials and Structures*, 2014.

[151] K. K. Alaneme and E. A. Okotete, "Reconciling viability and cost-effective shape memory alloy options – A review of copper and iron based shape memory metallic systems," *Engineering Science and Technology, an International Journal*, vol. 19, 2016.

[152] "SmartFlex Brochure 2." https://www.saesgetters.com/sites/default/files/SmartFlex%20Brochure_0.pdf, 2017. [Online; accessed 2017/11/07].

[153] W. Huang, "On the selection of shape memory alloys for actuators," *Materials and Design*, vol. 23, 2002.

[154] "SAES Smart Materials Brochure." https://www.saesgetters.com/sites/default/files/SAES%20Smart%20Materials%20Brochure_0.pdf, 2017. [Online; 2017/11/07].

[155] C. Zanotti, P. Giuliani, S. Arnaboldi, and A. Tuissi, "Analysis of Wire Position and Operating Conditions on Functioning of NiTi Wires for Shape Memory Actuators," *Journal of Materials Engineering and Performance*, vol. 20, 2011.

[156] G. S. Mammano and E. Dragoni, "Effects of loading and constraining conditions on the thermomechanical fatigue life of niti shape memory wires," *Journal of Materials Engineering and Performance*, 2014.

[157] S. S. Nakshatharan, K. Dhanalakshmi, and D. J. S. Ruth, "Effect of stress on bandwidth of antagonistic shape memory alloy actuators," *Journal of Intelligent Material Systems and Structures*, vol. 27, 2014.

[158] C. Jackson, H. J. Wagner, and R. J. Wasilewski, "The alloy with a memory, 55-Nitinol: Its physical metallurgy, properties, and applications," tech. rep., NASA, 1972. NASA-SP5110.

[159] M. A. Thrasher, A. R. Shahin, P. H. Meckl, and J. D. Jones, "Efficiency analysis of shape memory alloy actuators," *Smart Materials and Structures*, vol. 3, 1994.

[160] D. Reynaerts and H. V. Brussel, "Design aspects of shape memory actuators," *Mechatronics*, vol. 8, 1998.

[161] B. Lynch, X.-X. Jiang, A. Ellery, and F. Nitzsche, "Characterization, modeling, and control of Ni-Ti shape memory alloy based on electrical resistance feedback," *Journal of Intelligent Material Systems and Structures*, vol. 27, 2016.

[162] S. Majima, K. Kodama, and T. Hasegawa, "Modeling of Shape Memory Alloy Actuator and Tracking Control System with the Model," *IEEE Transactions on Control Systems Technology*, vol. 9, 2001.

[163] J. Jayender, R. V. Patel, S. Nikumb, and M. Ostojic, "Modeling and Control of Shape Memory Alloy Actuators," *IEEE Transactions on Control Systems Technology*, vol. 16, 2008.

[164] D. Cui, G. Song, and H. Li, "Modeling of the electrical resistance of shape memory alloy wires," *Smart Materials and Structures*, vol. 19, 2010.

[165] T.-M. Wang, Z.-Y. Shi, D. Liu, C. Ma, and Z.-H. Zhang, "An Accurately Controlled Antagonistic Shape Memory Alloy Actuator with Self-Sensing," *Sensors*, 2012.

[166] H. Cho *et al.*, "Exploitation of shape memory alloy actuator using resistance feedback control and its development," *Progress in Natural Science: Materials International*, vol. 20, 2010.

[167] G. Bertolino, A. Yawny, and J. Pelegrina, "The limitations of electrical resistance for accurate positioning of shape-memory actuators: The case of well-oriented CuZnAl single-crystals under uniaxial loading," *Materials and Design*, vol. 117, 2017.

[168] A. Gurley, T. R. Lambert, D. Beale, and R. Broughton, "Robust Self-Sensing in NiTi Actuators using a Dual Measurement Technique," in *Proceedings of the ASME 2016 Conference on Smart Materials, Adaptive Structures and Intelligent Systems*, 2016.

[169] Y. Tadesse, N. Thayer, and S. Priya, "Tailoring the Response Time of Shape Memory Alloy Wires through Active Cooling and Pre-stress," *Journal of Intelligent Material Systems and Structures*, vol. 0, 2009.

[170] M. Reinoehl, D. Bradley, R. Bouthot, and J. Proft, "The Influence of Melt Practice on Final Fatigue Properties of Superelastic NiTi Wires," in *Proceedings of the International Conference on Shape Memory and Superelastic Technologies*, 2000.

[171] J. R. S. Anadón, "Large force shape memory alloy linear actuator," Master's thesis, University of Florida, 2002.

[172] K. Chastaing and et. al., "Effect of Cu and Hf additions on NiTi martensitic transformation," *Material Science and Engineering A*, vol. 438–440, 2006.

[173] M. Leary, F. Schiavone, and A. Subic, "Lagging for control of shape memory alloy actuator response time," *Materials and Design*, vol. 31, 2010.

[174] J. Cui and et. al., "Combinatorial search of thermoelastic shape-memory alloys with extremely small hysteresis width," *Nature*, vol. 5, 2006.

[175] H. Kato, T. Ozu, S. Hashimoto, and S. Miura, "Cyclic stress – strain response of superelastic Cu – Al – Mn alloy single crystals," *Material Science and Engineering A*, vol. 264, 1999.

[176] M. Rahim *et al.*, "Impurity levels and fatigue lives of pseudoelastic NiTi shape memory alloys," *Acta Materialia*, vol. 61, 2013.

[177] K. J. Vinoy, G. K. Ananthasuresh, R. Pratap, and S. B. Krupanidhi, *Micro and Smart Devices and Systems*, ch. Nickel–Titanium Shape Memory Alloy Wires for Thermal Actuators. Springer India, 2014.

[178] M. Strathern, "'Improving ratings': audit in the British University system," *European Review*, vol. 5, no. 3, 1997.

[179] M. F. Ashby, "Multi-Objective Optimization in Material Design and Selection," *Acta Materialia*, pp. 359–368, 2000.

[180] S. Roundy, "On the Effectiveness of Vibration-based Energy Harvesting," *Journal of Intelligent Material Systems and Structures*, vol. 16, 2005.

[181] "IRE Standards on Piezoelectric Crystals: Determination of the Elastic, Piezoelectric, and Dielectric Constants - The Electromechanical Coupling Factor, 1958," tech. rep., 1958.

[182] S. Roundy, P. K. Wright, and J. Rabaey, "A study of low level vibrations as a power source for wireless sensor nodes," *Computer Communications*, vol. 26, 2003.

[183] A. D. Poole and J. D. Booker, "Design methodology and case studies in actuator selection," *Mechanism and Machine Theory*, vol. 46, 2011.

[184] C. W. de Silva, *Sensors and Actuators*. CRC Press, 2nd ed., 2016.

[185] J. E. Huber, N. A. Fleck, and M. F. Ashby, "The selection of mechanical actuators based on performance indices," in *Proceedings in Royal Society of London A: Mathematical, Physical and Engineering Sciences*, vol. 453, pp. 2185–2205, 1997.

[186] M. Zupan, M. F. Ashby, and N. A. Fleck, "Actuator Classification and Selection — The Development of a Database," *Advanced Engineering Materials*, 2002.

[187] C. G. O'Neill, D. S. Randall, and P. C. Smiley, "Piezomotors — Electromechanical Muscle," in *SAE Technical Paper*, SAE International, 02 1980.

[188] V. Giurgiutiu, R. Pomirleanu, and C. A. Rogers, "Energy-based comparison of solid-state induced-strain actuators," tech. rep., University of South Carolina: Laboratory for Adaptive Materials and Smart Structures, 2000.

[189] J. K. Dukowicz, "Theory of optimum linear induction motors," *Journal of Applied Physics*, vol. 47, 1976.

[190] L. F. Epstein, W. M. A. Andersen, and L. R. Harden, "High Intensity Ultrasonics: The Power Output of a Piezoelectric Quartz Crystal," *The Journal of Acoustical Society of America*, vol. 19, 1947.

[191] A. Jahan and K. L. Edwards, "A state-of-the-art survey on the influence of normalization techniques in ranking: Improving the materials selection process in engineering design," *Materials and Design*, pp. 335–342, 2015.

[192] "Piezo Mechanics Design Tutorial: Piezoelectricity, Forces and Stiffness." http://www.piezo.ws/piezoelectric_actuator_tutorial/Piezo_Design_part3.php. [Online; accessed 2017/11/09].

[193] N. Paine and L. Sentis, "Design and Comparative Analysis of a Retrofitted Liquid Cooling System for High-Power Actuators," *Actuators*, vol. 4, 2015.

[194] W. Tong, *Mechanical Design of Electric Motors*. CRC Press, 2014.

[195] "International vocabulary of metrology – Basic and general concepts and associated terms (VIM)," standard, Joint Committee for Guides in Metrology (JCGM), 2012.

[196] National Research Council, *Expanding the Vision of Sensor Materials*. The National Academies Press, 1995.

[197] J. Shieh *et al.*, "The selection of sensors," *Processes in Material Science*, vol. 46, 2001.

[198] R. J. M. Vullers *et al.*, "Micropower Energy Harvesting," *Solid State Electronics*, vol. 53, 2009.

[199] A. Chauhan and R. Vaish, "A comparative study on material selection for microelectromechanical systems," *Materials and Design*, vol. 41, pp. 177–181, 2012.

[200] P. Sharma and N. Gupta, "Investigation on material selection for gate dielectric in nanocrystalline silicon (nc-Si) top-gated thin film transistor (TFT) using Ashby's, VIKOR and TOPSIS," *Journal of Material Science: Materials in Electronics*, pp. 9607–9613, 2015.

[201] M. Yazdani and A. F. Payam, "A comparative study on material selection of microelectromechanical systems electrostatic actuators using Ashby, VIKOR and TOPSIS," *Materials and Design*, vol. 65, pp. 328–334, 2015.

[202] T. L. Saaty, "Decision making with the analytic hierarchy process," *International Journal of Services Sciences*, vol. 1, pp. 83–98, 2008.

[203] T. L. Saaty, *The Analytic Hierarchy Process*. McGraw Hill, 1980.

[204] "Expert choice customers span nearly every industry." http://expertchoice.com/clients-successes/, 2017. [Online; accessed 2017/10/16].

[205] K. Yoon, *Systems Selection by Multiple Attribute Decision Making*. PhD thesis, Kansas State University, 1980.

[206] C.-L. Hwang and K. Yoon, *Multiple Attribute Decision Making*. Springer-Verlag, 1981.

[207] M. Behzadian *et al.*, "A state-of the-art survey of TOPSIS applications," *Expert Systems with Applications*, pp. 13051–13069, 2012.

[208] A. Milani, A. Shanian, R. Madoliat, and J. Nemes, "The effect of normalization norms in multiple attribute decision making models: a case study in gear material selection," *Structural and Multidisciplinary Optimization*, vol. 29, no. 4, pp. 312–318, 2005.

[209] C. K. Halil Çaliskan, Bilal Kursuncu and S. Y. Güven, "Material selection for the tool holder working under hard milling conditions using different multi criteria decision making methods," *Materials and Design*, vol. 45, pp. 473–479, 2013.

[210] L. Anojkumar, M. Ilangkumaran, and V. Sasirekha, "Comparative analysis of MCDM methods for pipe material selection in sugar industry," *Expert Systems and Applications*, vol. 41, pp. 2964–2980, 2014.

[211] S. Opricovic and G.-H. Tzeng, "Compromise solution by MCDM methods: A comparative analysis of VIKOR and TOPSIS," *European Journal of Operational Research*, vol. 156, 2004.

[212] A. Jahan, F. Mustapha, M. Y. Ismail, S. Sapuan, and M. Bahraminasab, "A comprehensive VIKOR method for material selection," *Materials and Design*, 2011.

[213] J. Huang, G. Tzeng, and H. Liu, *Cutting-Edge Research Topics on Multiple Criteria Decision Making. Communications in Computer and Information Science*, ch. A Revised VIKOR Model for Multiple Criteria Decision Making - The Perspective of Regret Theory. Springer, Berlin, Heidelberg, 2009.

[214] A. Mardani *et al.*, "VIKOR Technique: A Systematic Review of the State of the Art Literature on Methodologies and Applications," *Sustainability*, vol. 8, 2016.

[215] Y. Reich, "My method is better!," *Research in Engineering Design*, vol. 21, 2010.

[216] B. Ceballos, M. T. Lamata, and D. A. Pelta, "Fuzzy Multicriteria Decision-Making Methods: A Comparative Analysis," *International Journal of Intelligent Systems*, 2017.

[217] J. Callerame, R. H. Tancrell, and D. T. Wilson, "Transmitters and receivers for medical ultrasonics," in *Proceedings of IEEE Ultrasonics Symposium*, pp. 407–411, 1979.

[218] L. F. Brown, "Design Considerations for Piezoelectric Polymer Ultrasound Transducers," *IEEE Transactions on Ultrasonics, Ferroelectrics, and Frequency Control*, vol. 47, no. 6, 2000.

[219] T. Rödig, A. Schonecker, and G. Gerlach, "A Survey on Piezoelectric Ceramics for Generator Applications," *Journal of the American Ceramic Society*, vol. 93, no. 4, 2010.

[220] P. D. Mitcheson *et al.*, "Energy Harvesting From Human and Machine Motion for Wireless Electronic Devices," *Proceedings of the IEEE*, vol. 96, no. 9, 2008.

[221] Z. Yang and J. Zu, "Comparison of PZN-PT, PMN-PT single crystals and PZT ceramic for vibration energy harvesting," *Energy Conversion and Management*, vol. 122, 2016.

[222] Q.-M. Wang, X.-H. Du, B. Xu, and L. E. Cross, "Electromechanical Coupling and Output Efficiency of Piezoelectric Bending Actuators," *IEEE Transactions on Ultrasonics, Ferroelectrics, and Frequency control*, vol. 46, no. 3, 1999.

[223] C. D. Richards, M. J. Anderson, D. F. Bahr, and R. F. Richards, "Efficiency of energy conversion for devices containing a piezoelectric component," *Journal of Micromechanics and Mictroengineering*, vol. 14, 2004.

[224] S. Priya, "Advances in energy harvesting using low profile piezoelectric transducers," *Journal of electroceramics*, vol. 19, 2007.

[225] L. Wang and F. G. Yuan, "Vibration energy harvesting by magnetostrictive material," *Smart Materials and Structures*, vol. 17, 2008.

[226] J. H. Cho, R. F. Richards, D. F. Bahr, , C. D. Richards, and M. J. Anderson, "Efficiency of energy conversion by piezoelectrics," *Applied Physics Letters*, vol. 16, 2006.

[227] "IEEE Standard on Piezoelectricity," *IEEE Std. 176-1978*, pp. 1–59, 1988.

[228] S. Priya, "Criterion for Material Selection in Design of Bulk Piezoelectric Energy Harvesters," *IEEE Transactions on Ultrasonics, Ferroelectrics, and Frequency control*, vol. 57, no. 12, 2010.

[229] T. L. Saaty, "The analytic hierarchy process - what it is and how it is used," *Mathematical Modelling*, vol. 9, 1987.

[230] J. A. Alonso and T. Lamata, "Consistency in the Analytic Hierarchy Process: A New Approach," *International Journal of Uncertainty*, vol. 14, no. 4, 2006.

[231] T.-C. Wang and H.-D. Lee, "Developing a fuzzy topsis approach based on subjective weights and objective weights," *Expert Systems with Applications*, vol. 36, 2009.

[232] A. Shemshadi, H. Shirazi, M. Toreihi, and M. Tarokh, "A fuzzy VIKOR method for supplier selection based on entropy measure for objective weighting," *Expert Systems with Applications*, vol. 38, 2011.

[233] P. M. . J. Baborowski, "Micromachined Ultrasonic Transducers and Acoustic Sensors Based on Piezoelectric Thin Films," *Journal of Electroceramics*, vol. 12, pp. 101–108, 2004.

[234] S. Zhang *et al.*, "Advantages and challenges of relaxor-$PbTiO_3$ ferroelectric crystals for electroacoustic transducers – A review," *Progress in Material Science*, vol. 68, pp. 1–66, 2015.

[235] K. K. Shung and M. Zipparo, "Ultrasonic Transducers and Arrays," *IEEE Engineering in Medicine and Biology*, vol. 15, no. 6, 1996.

[236] "Characteristics of piezoelectric transducers." https://www.nde-ed.org/EducationResources/CommunityCollege/Ultrasonics/EquipmentTrans/characteristicspt.htm. [Online; accessed 2017/10/16].

[237] R. E. McKeighen, "Design Guidelines for Medical Ultrasonic Arrays," in *Proc. SPIE 3341, Medical Imaging 1998: Ultrasonic Transducer Engineering*, 1998.

[238] C. S. Desilets, J. D. Fraser, and G. S. Kino, "The Design of Efficient Broad-Band Piezoelectric Transducers," *IEEE Transactions on Sonics and Ultrasonics*, vol. SU-25, 1978.

[239] J. M. Cannata *et al.*, "Design of Efficient, Broadband Single-Element (20–80 MHz) Ultrasonic Transducers for Medical Imaging Applications," *IEEE Transactions on Ultrasonics, Ferroelectrics, and Frequency control*, vol. 50, 2003.

[240] K. Uchino, "Introduction to piezoelectric actuators and transducers," 2003.

[241] K. K. Shung, J. M. Cannata, and Q. F. Zhou, "Piezoelectric materials for high frequency medical imaging applications: A review," *Journal of Electroceramics*, 2007.

[242] J. A. Gallego-Juarez, "Piezoelectric ceramics and ultrasonic transducers," *Journal of Physics E: Scientific Instrumentation*, vol. 22, 1989.

[243] Q. X. Chen and P. A. Payne, "Industrial applications of piezoelectric polymer transducers," *Measurement Science Technology*, vol. 6, 1995.

[244] H. J. Lee and S. Zhang, "Design of Low-Loss 1–3 Piezoelectric Composites for High-Power Transducer Applications," *IEEE Transactions on Ultrasonics, Ferroelectrics, and Frequency Control*, vol. 59, no. 9, 2012.

[245] K. A. Snook *et al.*, "Design, Fabrication, and Evaluation of High Frequency, Single-Element Transducers Incorporating Different Materials," *IEEE Transactions on Ultrasonics, Ferroelectrics, and Frequency Control*, vol. 49, no. 2, 2002.

[246] R. M. White, C. T. Chuang, and A. C. Lee, "Bulk Ultrasonic Transducer Employing Piezoelectric Film on Thin Metal Sheet," *IEEE Transactions on Sonics and Ultrasonics*, vol. SU-28, no. 1, 1981.

[247] M. Silk, *Ultrasonic Transducers for Nondestructive Testing*. CRC Press, 1984.

[248] H. Schlaberg and J. Duffy, "Piezoelectric polymer composite arrays for ultrasonic medical imaging applications," *Sensors and Actuators A*, vol. 44, 1994.

[249] G. S. Kino, *Acoustic Waves: Devices, Imaging, & Analog Signal Processing*. Prentice-Hall Inc., 1987.

[250] C. H. Sherman and J. L. Butler, *Transducers and Arrays for Underwater Sound*. Springer Science+Business Media, 2013.

[251] J. S. Jeong and K. K. Shung, "Improved fabrication of focused single element P(VDF–TrFE) transducer for high frequency ultrasound applications," *Ultrasonics*, vol. 53, 2013.

[252] S. Saffar and A. Abdullah, "Determination of acoustic impedances of multi matching layers for narrowband ultrasonic airborne transducers at frequencies <2.5 MHz – Application of a genetic algorithm," *Ultrasonics*, vol. 52, 2012.

[253] J. Chen and R. Panda, "Review: Commercialization of Piezoelectric Single Crystals for Medical Imaging Applications," in *2005 IEEE Ultrasonics Symposium*, 2005.

[254] "Lithium Niobate - Boston Piezo-Optics Inc.." http://www.bostonpiezooptics.com/lithium-niobate. [Online; accessed 2017/11/15].

[255] A. W. Warner, M. 0noe, and G. A. Coquin, "Determination of Elastic and Piezoelectric Constants for Crystals in Class (3m)," *The Journal of Acoustical Society of America*, vol. 42, 1967.

[256] R. T. Smith and F. S. Welsh, "Temperature Dependence of the Elastic, Piezoelectric, and Dielectric Constants of Lithium Tantalate and Lithium Niobate," *Journal of Applied Physics*, vol. 42, 1971.

[257] "Piezoelectric PMN-PT Single Crystal Products," tech. rep., CTS Corportation, 2016.

[258] S. Rajala, M. Paajanen, and J. Lekkala, "Measurement of Sensitivity Distribution Map of a Ferroelectret Polymer Film," *IEEE Sensors Journal*, vol. 16, no. 23, 2016.

[259] Q. Zhou, S. Lau, D. Wu, and K. K. Shung, "Piezoelectric films for high frequency ultrasonic transducers in biomedical applications," *Progress in Materials Science*, vol. 56, 2011.

[260] C. R. Bowen, H. A. Kim, P. M. Weaver, and S. Dunn, "Piezoelectric and ferroelectric materials and structures for energy harvesting applications," *Energy & Environmental Science*, 2014.

[261] "Crystal quartz properties - boston piezo-optics inc.." http://www.bostonpiezooptics.com/crystal-quartz.

[262] Q. Zhou, K. H. Lam, H. Zheng, W. Qiu, and K. K. Shung, "Piezoelectric single crystal ultrasonic transducers for biomedical applications," *Progress in Materials Science*, vol. 66, 2014.

[263] R. S. Dahiya and M. Valle, *Robotic Tactile Sensing*. Springer, Dordrecht, 2013.

[264] K. W. Kwok, H. L. W. Chan, and C. L. Choy, "Evaluation of the Material Parameters of Piezoelectric Materials by Various Methods," *IEEE Transactions on Ultrasonics, Ferroelectrics, and Frequency Control*, vol. 44, no. 4, 1997.

[265] V. Bovtun *et al.*, "Ferroelectret non-contact ultrasonic transducers," *Journal of Applied Physics A*, vol. 88, 2007.

[266] "Standard Specification for Wrought Iron-Cobalt High Magnetic Saturation Alloys (UNSR30005 and K92650)," *ASTM:A801–14*, pp. 1–59, 2014.

[267] M. Inc., "Metglas Magnetic Alloy 2605S3A(Iron-based)," tech. rep., 2009.

[268] C. Modzelewski, H. T. Savage, L. T. Kabacoff, and A. E. Clark, "Magnetomechanical coupling and permeability in transversely annealed metglas 2605 alloys," *IEEE Transactions on Magnetics*, 1981.

[269] R. S. Weis and T. K. Gaylord, "Lithium Niobate: Summary of Physical Properties and Crystal Structure," *Applied Physics A*, vol. 37, pp. 191–203, 1985.

[270] "Piezoceramic discs, rods and cylinders." https://www.piceramic.com/en/products/piezoceramic-components/disks-rods-and-cylinders/, 2017. [Online; accessed 2017/11/27].

[271] "Crystal standard shapes and tolerances." http://www.trstechnologies.com/Portals/0/Crystal2017. [Online; accessed 2017/11/27].

[272] G. Liu, S. Zhang, W. Jiang, and W. Cao, "Losses in ferroelectric materials," *Materials Science and Engineering R*, vol. 89, 2015.

[273] "Piezo Mechanics Design Tutorial: Piezoelectricity, Forces and Stiffness." http://www.piezo.ws/piezoelectric_actuator_tutorial/Piezo_Design_part3.php. [Online; accessed 2017/11/27].

[274] S. John, J. Sirohi, G. Wang, and N. M. Wereley, "Comparison of piezoelectric, magnetostrictive, and electrostrictive hybrid hydraulic actuators," *Journal of Intelligent Material Systems and Structures*, vol. 18.

[275] "Piezotech rt relaxor terpolymers for organic electronics," tech. rep., Piezotech Arkema Group, 2015.

[276] M. Paajanen, J. Lekkala, and K. Kirjavainen, "ElectroMechanical Film Å" EMFi / âĂŤ a new multipurpose electret material," *Sensors and Actuators*, vol. 84.

[277] J. DÄŰring *et al.*, "Cellular Polypropylene Ferroelectret Film: Piezoelectric Material for Non-Contact Ultrasonic Transducers," in *17th World Conference on Nondestructive Testing*, 2008.

[278] Y. A. Genenko, J. Glaum, M. J. Hoffmann, and K. Albe, "Mechanisms of aging and fatigue in ferroelectrics," *Materials Science and Engineering B*, vol. 192, 2015.

[279] P. Pertsch *et al.*, "Development of Highly Reliable Piezo Multilayer Actuators and Lifetime Tests under DC and AC Operating Conditions," tech. rep., Physik Instrumente Ceramic GmbH, 2010.

[280] S. Zhang *et al.*, "Polarization fatigue in $Pb(In_{0.5}Nb_0.5)O_3$–$Pb(Mg_{1/3}Nb_{2/3})O_3$–$PbTiO_3$ single crystals," *Acta Materialia*, vol. 58, 2010.

[281] G.-D. Zhu *et al.*, "Electrical Fatigue in Ferroelectric P(VDF-TrFE) Copolymer Films," *IEEE Transactions on Dielectrics and Electrical Insulation*, vol. 17, no. 4, 2010.

[282] X. Qiu, M. Sborikas, W. Wirges, and R. Gerhard, "Effective polarization fatigue in cellular polypropylene ferroelectrets," 2010.

[283] K. Prajapati, R. D. Greenough, and A. Wharton, "Magnetic and magnetoelastic response of stress cycled Terfenol-D," *American Institute of Physics*, vol. 81, no. 8, 1997.

[284] M.-J. Pan *et al.*, "Comparison of Actuator Properties for Piezoelectric and Electrostrictive Materials," in *Proceedings of SPIE Vol. 3992*, Smart Structures and Materials 2000: Active Materials: Behavior and Mechanics, 2010.

[285] V. Berbyuk, "Vibration energy harvesting using Galfenol based transducer," in *Proceedings of SPIE Vol. 8688*, Active and Passive Smart Structures and Integrated Systems 2013, 2013.

APPENDICES

Appendix A

Piezoelectric Derivations

Derivation of transmission efficiency (TP):

First, we will derive the relation $c^E = c^D(1 - k_t^2)$. Using the second equation of a set of constitutive equations, Equation 1d found in Jaffe et al. [31]:

$$T = -hD + c^D S \tag{A.1}$$

Substituting the first equation from Equation 1b, $D = \epsilon^S E + eS$,

$$\tag{A.2}$$

$$T = -h(\epsilon^S E + eS) + c^D S \tag{A.3}$$

$$T = -h(\epsilon^S E) + (c^D - he)S \tag{A.4}$$

Knowing that $h = e/\epsilon^S$, we can substitute:

$$\tag{A.5}$$

$$T = -eE + \left(c^D - \frac{e^2}{\epsilon^S}\right)S \tag{A.6}$$

If we look at the second equation from Equation 1b, $T = -eE + c^E S$, we can see that

$$\tag{A.7}$$

$$c^E = c^D - \frac{e^2}{\epsilon^S} \tag{A.8}$$

Using the $k_t^2 = e^2/(\epsilon^S c^D)$ relation found in Table III of Jaffe et al. [31], we get the relationship:

$$\tag{A.9}$$

$$c^E = c^D(1 - k_t^2) \tag{A.10}$$

$$\tag{A.11}$$

The following equations and relations will be used:

$$S = dE + s^E T \tag{A.12}$$

$$S = \frac{\Delta t}{t} \tag{A.13}$$

$$E = -\frac{V}{t} \tag{A.14}$$

$$d = e/c^E \tag{A.15}$$

$$c^E = c^D(1 - k_t^2) \tag{A.16}$$

$$k_t = \frac{e}{\sqrt{\epsilon^S c^D}} \tag{A.17}$$

As indicated in Callerame et al., the following assumptions are taken [217]:

1. we are to find x_t, thus we say that $x_t = \Delta t$,
2. T is unclamped (or T=0) and we are applying 1V.

Using Equation A.12 and applying the first assumption:

$$S = dT + \cancelto{0}{s^E T} \tag{A.18}$$

Subbing Equation A.13, we get:

$$\tag{A.19}$$

$$\frac{\Delta t}{t} = dT \tag{A.20}$$

Subbing Equation A.14, the relation becomes:

$$\tag{A.21}$$

$$\frac{\Delta t}{t} = d\left(\frac{-V}{t}\right) \tag{A.22}$$

$$\Delta t = -dV \tag{A.23}$$

Applying the second assumption, we get to the real form of TP:

$$\tag{A.24}$$

$$\Delta t = -d \tag{A.25}$$

To get to definition by Callerame et al. we must apply Equation A.15:

$$\tag{A.26}$$

$$\Delta t = -\frac{e}{c^E} \tag{A.27}$$

Substituting A.16:

$$\Delta t = -\frac{e}{c^D(1-k_t^2)} \tag{A.28}$$

$$\Delta t = -\frac{e}{c^D(1-k_t^2)}\frac{\sqrt{\epsilon^S c^D}}{\sqrt{\epsilon^S c^D}} \tag{A.29}$$

Substituting for k_t, we can get the published TP

$$\Delta t = -\frac{k_t}{c^D(1-k_t^2)}\sqrt{\epsilon^S c^D} = -\frac{k_t}{(1-k_t^2)}\sqrt{\frac{\epsilon^S}{c^D}} \tag{A.30}$$

Appendix B

Material Properties

Table B.1: Piezoelectric Properties

	T_c	T_{RT}	d_{33}	d^*_{33}	d_{31}	d_{15}	s^E_{33}	s^D_{33}	s^E_{11}	s^D_{11}	ϵ^T_{33}	ϵ^S_{33}	ϵ^T_{11}	ϵ^S_{11}	$\tan\delta_e$	Q_m	k_{33}	k_{31}	k_{15}	k_p	k_t	E_c	ρ	c_p
Material	[$^\circ C$]		[pC/N]				[$10^{-12}\,m^2/N$]				—				—	—	—	—	—	—	—	[kV/mm]	[kg/m^3]	[m/s]
Quartz (X-cut)	573	–	2.3	–	–	–	9.6	9.56	12.77	12.79	4.7	4.63	4.52	4.42	2*10^{-6}	180000–290000	–	–	–	0.088–0.14	0.11	–	2650	5740
AlN	>1000	–	5	–	-2	3.6	2.824	–	2.854	–	11.9	10	–	–	–	2490	0.23	–	–	–	0.065	–	3300	–
CdS	–	–	10.3	–	-5.18	-13.98	16.97	–	20.69	–	10.33	9.53	–	–	–	1000	0.26	–	–	–	–	–	4820	–
GaN	–	–	3.7	–	-1.9	3.1	2.915	–	3.326	–	10.5	11.2	–	8.6	–	2800	–	–	–	–	–	–	5986	–
ZnO	–	–	12.4	–	-5	-8.3	6.94	–	7.86	–	11	8.84	–	–	–	1700	0.48	–	–	–	0.09	–	5680	–
$BaTiO_3$	115	–	190	–	-78	260	9.5	7.1	9.1	8.7	1700	1260	1450	1115	0.01	300	0.5	-0.21	0.48	-0.36	0.36	0.4	6020	5470
$PbTiO_3$	470	–	56	–	–	68	–	–	–	–	190	–	–	–	–	1300	0.45	–	–	–	0.49	–	6900	5200
$LiNbO_3$ (36° Rotated Y-cut)	1150	–	6	–	-0.85	69.2	5.026	4.89	5.831	5.2	28.7	27.9	85.2	44.3	0.001	10^4	–	–	–	–	0.485	–	4628	7340
$LiNbO_3$ (41° X-cut)	1150	–	6	–	-0.85	69.2	5.026	4.89	5.831	5.2	28.7	27.9	85.2	44.3	0.001	10^4	–	–	0.682	–	–	–	4628	4795
PZT 4 (Type I)	328	–	289	330	-123	496	15.5	7.9	12.3	10.9	1300	635	1475	730	0.004	500	0.7	-0.33	0.71	-0.58	0.51	>1.0	7500	4600
PZT 5A (Type II)	365	–	374	600	-171	584	18.8	9.46	16.4	14.4	1700	830	1730	916	0.02	75	0.705	-0.34	0.685	-0.6	0.49	0.7	7750	4350
PZT 5H (Type VI)	193	–	593	800	-274	741	20.7	8.99	16.5	14.1	3400	1470	3130	1700	0.02	65	0.75	-0.39	0.675	-0.65	0.505	0.4	7500	4560
PZT 8 (Type III)	300	–	218	250	-93	–	13.9	8.5	11.1	10.1	1000	600	–	–	0.004	1000	0.62	-0.295	–	-0.5	0.44	1.5	7600	4600*
PMN-28%PT Type A	120–130	90–100	1190	–	-568	135	36.15	7.06	45.86	39.23	5500	895	1600	1467	0.004	120	0.9	0.43	0.28	–	0.60	2.5	8100	4610
PMN-32%PT Type B	130–140	80–90	1620	–	-760	192	49.18	6.82	58.85	49.53	7000	700	1620	1368	0.004	120	0.93	0.44	0.39	–	0.62	2.5	8100	4610
PIN24%-PMN-PT	140–170	100–115	1285	–	-646	122	49.04	9.78	45.76	35.84	4573	868	1728	1611	0.004	180	0.89	0.46	0.26	–	0.50	4.5–6	8122	4571
PIN33%-PMN-PT	160–200	115–135	1338	–	-651	147	56.15	11.52	47.18	36.62	4532	905	1666	1509	0.004	180	0.89	0.47	0.31	–	0.54	5.5–7	8141	4571
PVDF	90	–	13–28	–	6–20	–	–	–	–	–	12	–	–	–	0.018	20	0.27	0.12	–	–	–	–	1800	2200
P(VDF-TrFE)	100	–	24–38	–	6–12	–	–	–	–	–	12	–	–	–	0.018	20	0.37	0.07	–	–	–	–	1900	2400
PVDF	–	–	-32.5	–	21	-27	472	–	365	–	7.6	–	6.9	–	0.256	13	0.19	0.1	–	–	0.146	120	1780	2200
P(VDF-TrFE) 75/25	119.8	–	-33.5	–	10.7	-36.3	300	–	332	–	7.9	–	7.4	–	0.106	19.61	0.116	–	–	–	0.262	–	1880	2400
Emfit 70μm thick	50	–	170	–	2	–	10^6	–	–	–	1.2	–	–	–	–	–	–	–	–	–	–	–	330	–
Emfit 80μm thick	50	–	250–400	–	2	–	10^6	–	–	–	1.1	–	–	–	0.001	–	0.06	–	–	–	–	–	330	85

* – Assumed to be equal to PZT 4

Table B.2: Piezoelectric Properties References

	T_c	T_{RT}	d_{33}	d^*_{33}	d_{31}	d_{15}	s^E_{33}	s^D_{33}	s^E_{11}	s^D_{11}	ϵ^T_{33}	ϵ^S_{33}	ϵ^T_{11}	ϵ^S_{11}	$\tan\delta_e$	Q_m	k_{33}	k_{31}	k_{15}	k_p	k_t	E_c	ρ	c_p
Material	$[^\circ C]$		[pC/N]				$[10^{-12}\,m^2/N]$				—				—	—	—	—	—	—	—	[kV/mm]	$[kg/m^3]$	[m/s]
α-Quartz	[32]	–	[261]	–	–	–	[261]	[261]	[261]	[261]	[261]	[261]	[261]	[261]	[261]	[261]	–	–	–	[33]	[34]	–	[32]	[235]
AlN	[32]	–	[260]	–	[260]	[260]	[260]	–	[260]	–	[260]	[260]	–	–	–	[260]	[260]	–	–	–	[33]	–	[32]	–
CdS	–	–	[260]	–	[260]	[260]	[260]	–	[260]	–	[260]	[260]	–	–	–	[260]	[260]	–	–	–	–	–	[32]	–
GaN	–	–	[260]	–	[260]	[260]	[260]	–	[260]	–	[260]	[260]	–	[35]	–	[260]	–	–	–	–	–	–	[35]	–
ZnO	–	–	[260]	–	[260]	[260]	[260]	–	[260]	–	[260]	[260]	–	–	–	[260]	[260]	–	–	–	[33]	–	[32]	–
$BaTiO_3$	[31]	–	[31]	–	[31]	[31]	[31]	[31]	[31]	[31]	[31]	[31]	[31]	[31]	[31]	[31]	[31]	[31]	[31]	[31]	[31]	[31]	[31]	[31]
$PbTiO_3$	[36]	–	[36]	–	–	[36]	–	–	–	–	[36]	–	–	–	–	[36]	[36]	[31]	[31]	[31]	[245]	–	[245]	[245]
$LiNbO_3$ (36° Rotated Y-cut)	[254]	–	[269]	–	[269]	[269]	[269]	[254]	[269]	[254]	[269]	[269]	[269]	[269]	[254]	[254]	–	–	–	–	[254]	–	[269]	[254]
$LiNbO_3$ (41° X-cut)	[254]	–	[269]	–	[269]	[269]	[269]	[254]	[269]	[254]	[269]	[269]	[269]	[269]	[254]	[254]	–	–	[254]	–	–	–	[269]	[254]
PZT 4 (Type I)	[31]	–	[31]	[31]	[31]	[31]	[31]	[31]	[31]	[31]	[31]	[31]	[31]	[31]	[31]	[31]	[31]	[31]	[31]	[31]	[31]	[31]	[31]	[31]
PZT 5A (Type II)	[31]	–	[31]	[31]	[31]	[31]	[31]	[31]	[31]	[31]	[31]	[31]	[31]	[31]	[31]	[31]	[31]	[31]	[31]	[31]	[31]	[31]	[31]	[31]
PZT 5H (Type VI)	[31]	–	[31]	[31]	[31]	[31]	[31]	[31]	[31]	[31]	[31]	[31]	[31]	[31]	[31]	[31]	[31]	[31]	[31]	[31]	[31]	[31]	[31]	[31]
PZT 8 (Type III)	[31]	–	[31]	[31]	[31]	–	[31]	[31]	[31]	[31]	[31]	[31]	–	–	[31]	[31]	[31]	[31]	–	[31]	[31]	[31]	[31]	—
PMN-28%PT Type A	[257]	[257]	[257]	–	[257]	[257]	[257]	[257]	[257]	[257]	[257]	[257]	[257]	[257]	[257]	[257]	[257]	[257]	[257]	[257]	[257]	[257]	[257]	[262]
PMN-32%PT Type B	[257]	[257]	[257]	–	[257]	[257]	[257]	[257]	[257]	[257]	[257]	[257]	[257]	[257]	[257]	[257]	[257]	[257]	[257]	–	[257]	[257]	[257]	[262]
PIN24%-PMN-PT	[257]	[257]	[257]	–	[257]	[257]	[257]	[257]	[257]	[257]	[257]	[257]	[257]	[257]	[257]	[257]	[257]	[257]	[257]	–	[257]	[257]	[257]	[262]
PIN33%-PMN-PT	[257]	[257]	[257]	–	[257]	[257]	[257]	[257]	[257]	[257]	[257]	[257]	[257]	[257]	[257]	[257]	[257]	[257]	[257]	–	[257]	[257]	[257]	[262]
PVDF	[46]	–	[46]	–	[46]	–	–	–	–	–	[46]	–	–	–	[46]	[46]	[46]	[46]	–	–	–	–	[46]	[218]
P(VDF-TrFE)	[46]	–	[46]	–	[46]	–	–	–	–	–	[46]	–	–	–	[46]	[46]	[46]	[46]	–	–	–	–	[46]	[218]
PVDF	–	–	[263]	–	[263]	[263]	[263]	–	[263]	–	[263]	–	[263]	–	[56]	[56]	[260]	[57]	–	–	[264]	[58]	[264]	[218]
P(VDF-TrFE) 75/25	[59]	–	[263]	–	[263]	[263]	[263]	–	[263]	–	[263]	–	[263]	–	[56]	[56]	[60]	–	–	–	[60]	–	[60]	[218]
Emfit 70μm thick	[83]	–	[83]	–	[83]	–	[83]	–	–	–	[83]	–	–	–	–	–	–	–	–	–	–	–	[83]	–
Emfit 80μm thick	[81]	–	[81]	–	[81]	–	[81]	–	–	–	[81]	–	–	–	[265]	–	[265]	–	–	–	–	–	[81]	[265]

B.1 Magnetostrictives

Table B.3: Commercial Magnetostrictive Properties

	Terfenol-D [113]	Galfenol[114]	Metglas [267]	Permendur 2V [266]
	$Tb_{0.3}Dy_{0.7}Fe_{1.92}$	$Fe_{81.6}Ga_{18.4}$	2605SA1	R30005
Mechanical Properties				
Density (kg/m^3)	9200–9300	7800	7290	8120
Young's Modulus at constant I (GPa)	18–55	40–60	–	–
Young's Modulus at constant V (GPa)	50–90	60–80	100–110	207
Speed of Sound (m/s)	1395–2444	2265–2775	–	–
Tensile (Compressive) Strength (MPa)	28 [123]	350	1000–2000	480–1340
Thermal Properties				
Thermal Conductivity (W/(m K) @25°C)	13.5	15–20	–	29.8
Electrical Properties				
Resistivity (10^{-8} Ω-m)	60	85	138	40
Curie Temperature (°C)	380	670	358	940
Magnetostrictive Properties				
Strain (10^{-6})	800–1200	200–250	20	60
Piezomagnetic Constant, d_{33} (nm/A)	6–10	20–30	–	–
Coupling Factor, k_{33}	0.7–0.8	0.6–0.7	>0.9*	–
Relative Permeability, μ_r/μ_0	2–10	75–100	35,000	15,000
Saturation Flux Density (Tesla)	1	1.5–1.6	1.41	2.30

* – Maximum coupling factor at 0 bias field. Reduces to 0.1 at 12 Oe [268]

Table B.4: Material-Based Figures of Merit

Type	Piezoelectric					Magnetostrictive		NiTi SMA			
	Soft PZT	Hard PZT	Relaxor	PVDF	Cellular	Terfenol-D	Galfenol	N=1	N< 10^2	N< 10^5	N< 10^7
Max Suggested Temperature ($^\circ C$)	73–183[a]	113–165[a]	60–349[a]	90–118	50–70	335–338	170–188		110[c]		
Standard Diameter Range (mm)	2–80	2–80	5–30	—	—	10–68	<23		0.02–0.51		
Safe Actuation Stress* (MPa)	12.5–25(30)		38(30–110)**	5–15	3	10–50**	10**	900	600	100–150	100–150
Static Strain (%)	0.10–0.16		0.1–0.2	2–5	9.6	0.08–0.12	0.02–0.025	6–8	6–8	2–4	0.5
Modulus of Elasticity (GPa)	111–117	115	97–124	0.1–2.5	0.001–0.002	90	125		28–83		
Density (kg/m^3)	7500–7600	7500–7750	8100–8360	1780–1900	330–1300	9200–9300	7800		6400–6500		
Coupling Coefficient	0.62–0.7	0.705–0.75	0.90–0.95	0.116–0.27	0.06	0.38–0.78	0.6–0.85		0.03***		
Mechanical Quality Factor	49–170	370–2500	120–180	13–20	1100	3–112	13.5–24.6		–		
Actuator FOMs											
Volumetric Energy Density (kJ/m^3)	6.5-20(15–24)		19–38(15–110)	50–380	140	3.9–30	1–1.3	(27–36)*103	(18–24)*103	(1–3)*103	250–375
(Strain Energy Eq.)						$1/2\ \sigma\epsilon$					
Specific Energy Density (J/kg)	0.86–2.7(2.0–3.2)	0.84–2.7(1.9–3.2)	2.3(1.8–14)	26–210	110–440	0.42–3.3	0.13–0.16	4200–5600	2800–3800	150–310	38–59
Volumetric Power Density† (W/m^3)	(7.5–720)*10^9		(7.5–3300)*10^9	(5.0–3800)*10^9	3.8*10^{1}2	(310–2400)*10^6	(80–100)*10^6	(1.9–240)*10^6	(1.3–160)*10^6	(.071–13)*10^6	(.018–2.5)*10^6
(Maximum Frequency)	(5–300)*10^5			(1–100)*10^5	5*10^5	80*10^3			0.07–6.67		
Specific Power Density (W/kg)	(0.99–96)*10^6	(0.97–96)*10^6	(0.90–410)*10^6	(2.6–2100)*10^6	(55–220)*10^6	(33–260)*10^3	(10–13)*10^3	(.3–38)*10^3	(.2–25)*10^3	11–2100	2.7–390
Energy Efficiency	0.90–0.99			0.90–0.95	–	0.80–0.99			0.013		
Cycle Life	>5*10^7–10^{12} ‡		>10^6‡	10^4–9*10^6‡	1.8*10^5‡	>>10^6§	–	1	100	10^5	10^6
Sensor FOMs											
Sensitivity	13.2–26.6	22.6–53.9	24.4–33.4	193–479	(142–295)*10^3	0.635–7.936	0.204		–		
Hysteresis	<0.06	<0.018	<0.005	–	–	0.1	<<0.1		38–41		

a – Using half curie temperature for PZT and $T_R T$ for relaxors
* – Brackets indicates safe actuation stress when used with a prestress mechanism
** – Using blocked stress calculated from actuators
*** - Using energy efficiency since no coupling coefficient exists
†– Only using pre-stressed safe actuation stress
‡– Indicating polarization fatigue properties; no fatigue properties available
§– Indicating stress cycle number; no fatigue properties available

Table B.5: References for Material-Based Figures of Merit

Type	Piezoelectric					Magnetostrictive		NiTi SMA			
	Soft PZT	Hard PZT	Relaxor	PVDF	Cellular	Terfenol-D	Galfenol	N=1	N< 10^2	N< 10^5	N< 10^7
Max Suggested Temperature ($°C$)	[272]	[272]	[22]	[46, 59]	[83, 81]	[113, 285]	[114, 285]			[132]	
Standard Diameter Range (mm)	[270]	[270]	[271]	—	—	[113]	[114]			[152, 132]	
Safe Actuation Stress* (MPa)	[273]([84])		[274]([188])	[275]	[81]	[188, 274]**	[274]**			[153]	
Static Strain (%)	[273]		[274]	[275]	[80]	[113]	[114]			[153]	
Modulus of Elasticity (GPa)	[31]	[31]	[257]	[57, 275]	[81]	[113]	[114]			[130]	
Density (kg/m^3)	[31]	[31]	[257]	[264, 46]	[276]	[113]	[114]			[132, 130]	
Coupling Coefficient	[31]	[31]	[22]	0.116[46]	[265]	[285, 113]	[285]			[160]	
Mechanical Quality Factor	[272]	[272]	[257]	[46, 218]	[277]	[120, 121]	[122, 118]			–	
Actuator FOMs											
Volumetric Energy Density (kJ/m^3) (Strain Energy Eq.)	–	–	–	–	–	–	–	–	–	–	–
Specific Energy Density (J/kg)	–	–	–	–	–	–	–	–	–	–	–
Volumetric Power Density† (W/m^3) (Maximum Frequency)	–	[185]	–	[185]	[185]	[185]	–	–	–	[185]	–
Specific Power Density (W/kg)	–	–	–	–	–	–	–	–	–	–	–
Energy Efficiency		[185]		[185]	–	[185]				[160]	
Cycle Life	[278, 279]		[280]	[281]	[282]	[283]	–			[160]	
Sensor FOMs											
Sensitivity	[272]	[272]	–	–	–	–	–			–	
Hysteresis	[284]	[284]	[284]	–	–	[285]	[285]			–	